Università degli Studi di Padova

Dipartimento di Ingegneria dell'Informazione

Corso di Laurea Magistrale
in Bioingegneria

Bayesian Approach for dimensionality reduction of compartmental model parameters of the PET [^{18}F]FDG tracer

Approccio Bayesiano per la riduzione di dimensionalità dei parametri del modello compartimentale del tracciante PET [^{18}F]FDG

Relatore:
Chiar.ma Prof.ssa Alessandra Bertoldo

Correlatore:
Dott. Mattia De Francisci

Laureando:
Pietro Laddomada

Anno accademico 2022/2023

Alla mia famiglia.

Abstract

Positron Emission Tomography (PET) with [^{18}F]FDG (Fluorodeoxyglucose) is a nuclear imaging technique widely utilized in oncology. It plays a crucial role in examining physiological and pathophysiological processes in vivo, enabling the quantitative measurement of biochemical changes in the body. This facilitates the detection of anomalies in the metabolism of tissues of interest. To establish a connection between PET signals and internal biochemical processes, compartmental modeling is required. Parameter estimation can be performed either at region-of-interest (ROI) level or at the voxel level, fully exploiting the PET scanner spatial resolution. In specific situations, for example when studying a lesion, the information provided by ROI level analysis may not be enough, and a voxel level analysis would be required.

The challenge lies in the type of signal obtained at the voxel level, characterized by a low Signal-to-Noise Ratio (SNR), in contrast to regional analysis. Currently, commonly employed methods for microparameter estimation at ROI level are not equally effective at the voxel level, due to the low SNR. Simplified approaches, such as the Patlak Graphical method, are available, but they generate parameters with less detailed physiological information. Therefore, there is a need for an approach able to produce reliable voxel-level results. A solution may be found in Bayesian approaches, which leverage a priori information to perform better in the presence of noisy data.

Nevertheless, microparameter estimation in the model is based on the assumption of having a noise-free Input function. This typically requires arterial sampling, which can be uncomfortable and burdensome for the patient. An alternative is the Image-Derived Input Function

(IDIF), which extracts the Input function directly from the PET image, using the Internal Carotid Arteries (ICA) or the Common Carotid Arteries (CCA), with corrections applied for Partial Volume Effect (PVE).

This thesis focuses on exploring a Bayesian approach to enable adequate voxel-level microparameter estimation. Specifically, the Maximum a Posteriori (MAP) estimation method is employed. In our implementation, the prior information is derived from ROI-level estimates with the ultimate goal of obtaining precise voxel-level estimates. Additionally, the MAP estimation was tested with a constraint on a model parameter, k_3, based on the voxel-wise K_i estimate obtained using Patlak's graphical analysis, to further reduce complexity. Furthermore, the impact of using different input functions extracted from different vascular ROIs was examined in this study.

The analysis was performed on a dataset consisting of 10 subjects affected by glioma who underwent [^{18}F]FDG acquisition on a PETMR system at the University Hospital of Padova. To assess the reliability of the results obtained with the MAP, the parametric maps were compared to the ones obtained using another bayesian approach, i.e. the Variational Bayes (VB). Voxel-level esimates coming from the two different methods exhibit a high correlation. As for the input function, we observe that similar estimates are obtained when using ICA's IDIF with PVE correction or when using CCA's IDIF without any correction. This approach opens doors for future research in handling data fitting with respect to measurement error and examining the influence of constraints on the posterior calculation of the k_3 parameter.

Abstract [Ita]

Positron Emission Tomography (PET) con [^{18}F]FDG (Fluorodeossiglucosio) è una tecnica di imaging nucleare ampiamente utilizzata in oncologia. Ha un ruolo cruciale nell'esaminare i processi fisiologici e patofisiologici in vivo, consentendo la misurazione quantitativa dei cambiamenti biochimici nel corpo. Ciò facilita la rilevazione di anomalie nel metabolismo dei tessuti d'interesse. Per stabilire una connessione tra i segnali PET e i processi biochimici interni, è richiesto l'utilizzo di un modello compartimentale. La stima dei parametri può essere eseguita a livello di regione di interesse (ROI) o a livello di voxel, sfruttando appieno la risoluzione spaziale dello scanner PET. In situazioni specifiche, ad esempio nello studio di una lesione, le informazioni fornite dall'analisi a livello di ROI potrebbero non essere sufficienti, e sarebbe richiesta un'analisi a livello di voxel.

La sfida risiede nel tipo di segnale ottenuto a livello di voxel, caratterizzato da un basso rapporto segnale-rumore (SNR), in contrasto al segnale ottenuto dall'analisi a livello di ROI. Attualmente, i metodi comunemente utilizzati per la stima dei microparametri a livello di ROI non sono altrettanto efficaci a livello di voxel, a causa del basso SNR. Approcci semplificati, come il metodo grafico di Patlak, sono applicabili, ma generano parametri con informazioni fisiologiche meno dettagliate. Pertanto, c'è la necessità di un approccio in grado di produrre risultati affidabili a livello di voxel. Una soluzione potrebbe essere negli stimatori Bayesiani, che sfruttano informazioni a priori per performare meglio in presenza di dati rumorosi.

Tuttavia, la stima dei microparametri nel modello è basata sull'assunzione di disporre di una funzione di input priva di rumore. Questo richiede

tipicamente campionamenti arteriali, che possono essere scomodi e gravosi per il paziente. Un'alternativa è la Image-derived Input Function (IDIF), che estrae la funzione di input direttamente dall'immagine PET, utilizzando le arterie carotidi interne (ICA) o le arterie carotidi comuni (CCA), con correzioni applicate per correggere i Partial Volume Effect (PVE).

Questa tesi si concentra sull'esplorazione di un approccio bayesiano per consentire una stima adeguata dei microparametri a livello di voxel. In particolare, è stato utilizzato il metodo di stima Maximum A Posteriori (MAP). Nella nostra implementazione, le informazioni a priori derivano dalle stime a livello di ROI, con l'obiettivo finale di ottenere stime precise a livello di voxel. Inoltre, la stima MAP è stata testata con un vincolo su un parametro del modello, il k_3, basato sulla stima voxel-wise di K_i ottenuta utilizzando l'analisi grafica di Patlak, per ridurre ulteriormente la complessità. Inoltre, è stata esaminata l'influenza dell'utilizzo di diverse funzioni di input estratte da diverse ROI vascolari in questo studio.

L'analisi è stata eseguita su un dataset composto da 10 soggetti affetti da glioma sottoposti ad una acquisizione con tracciante [^{18}F]FDG su un sistema PET/MR presso l'Ospedale Universitario di Padova. Per valutare l'affidabilità dei risultati ottenuti con la stima MAP, le mappe parametriche sono state confrontate con quelle ottenute utilizzando un altro approccio bayesiano, ovvero il Variational Bayes (VB). Le stime a livello di voxel ottenute dai due diversi metodi presentano una correlazione elevata. Per quanto riguarda la funzione di input, osserviamo che si ottengono stime simili utilizzando l'IDIF delle ICA con correzione del PVE o utilizzando l'IDIF delle CCA senza alcuna correzione. Questo approccio apre la strada a futuri studi sulla gestione dei dati rumorosi in relazione all'errore di misura e sull'ispezione dell'influenza dei vincoli sul calcolo a posteriori del parametro k_3.

Contents

List of Figures

List of Tables

Chapter 1

Introduction

1.1 Positron Emission Tomography

Positron Emission Tomography (*PET*) is a nuclear medicine technique for monitoring physiological and pathophysiological processes in vivo by using radiopharmaceuticals labeled with positron-emitting radionuclides [1]. It helps to extract quantitative measures of biochemical changes in the body, thus making it possible to identify abnormalities in the metabolism of the tissue of interest. PET research can suit into many different areas, including investigations into pathophysiology, pharmacology and drug development, and diagnostics, driving the work of physicians and researchers. It has the potential ability to image a wide range of processes that are critical for understanding the cause of disease, and can play a significant role in developing and monitoring targeted therapies in the field of precision medicine. The applications in neurology opens up a wide range of possibilities to advance research in numerous areas, such as neurodegenerative disease, oncology, and drug development [4, 3]. PET scan session requires the intravenous administration of bio-molecules labeled with positron emitting isotope (or tracers), which are previously synthesized using a cyclotron. These radiotracers must be able to cross the blood-brain barrier (BBB), reaching their intended target molecules. The radiotracer injected into the bloodstream will be exposed to a complex environment that may cause a breakdown into one or more metabolites [2]. Subsequently, the interaction of the radio tracer with the surrounding tissues causes it to lose kinetic energy, leading to the emission of a positron β^+ that interacts with an electron of the matter, resulting in the phenomenon of annihilation and, consequently, in the emission of a couple of γ rays, both of energy 511keV, emitted in opposite directions (180-degree to each other). The PET

tomograph detection system, which surrounds the patient under examination, is built to detect coincident events and measure their intensity and direction. Specifically, the scintillator is the main component and through computer-implemented algorithms, it is possible to perform the image reconstruction, identifying the origin from which they were emitted. Filtered back projection (FBP) is one of the most common reconstruction algorithms used. It is a modified version of the traditional back projection approach, which suffers from the issue of generating blurred images. FBP overcomes this limitation by applying a filter (for example, a ramp filter), which, however, has the main drawback of introducing noise in data. Another well-known approach is the Ordered-Subset Expectation Maximization (OSEM), which involves an iterative process, and is based on Maximum Likelihood Expectation Maximization (MLEM). This algorithm addresses the problem of noise in the FBP but comes with higher computational cost. The generated images allow to monitor and evaluate bodily processes such as glucose metabolism, oxygen metabolism, and cerebral blood flow. These are the three essential components in brain metabolism, and they can be expressed as follows: cerebral metabolic rate of glucose ($CMRglc$), cerebral metabolic rate of oxygen ($CMRO_2$), and cerebral blood flow (CBF). Depending on the process to trace, different radiotracers have been developed. It is also possible to distinguish between static and dynamic PET examinations based on the experimental frameworks, figure 1.1. In contrast to the second modality, which is more expensive and sophisticated and is favoured in research, the first modality just requires a single-frame acquisition and is primarily employed in clinical routine applications [6].

During the examination with dynamic procedure, the patient usually undergoes an arterial blood sampling, since the measurement of radioligand concentration in arterial plasma is required in order to derive quantitative information from PET data. Although the method is still a crucial tool for clinical and academic applications, the invasive nature of arterial sampling prevents it from being used in many therapeutic settings [6, 7].This leads to the necessity of exploring less-invasive alternatives to arterial cannulation, which can help exploit the full potential of PET quantification in clinical settings, by reducing both the patient's discomfort and the technical challenges required by the processing of arterial samples.

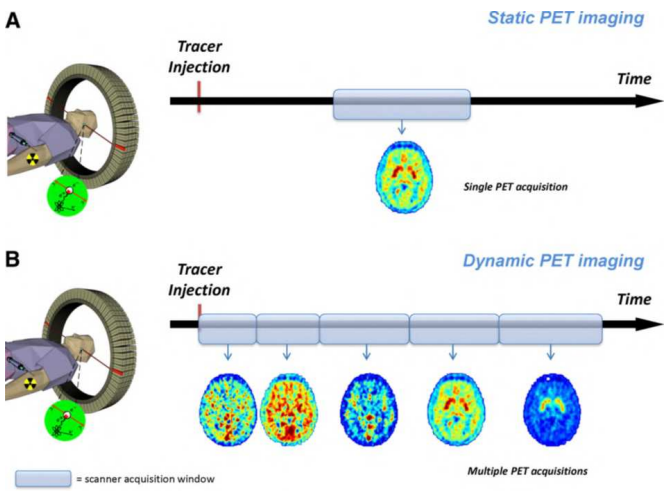

Figure 1.1: Static and dynamic PET image framework.

1.2 PET quantification

The image generated by a PET scan requires to be processed in order to be translated into relevant physiological information. A fully quantitative analysis is based on the definition of mathematical models, which rely on a priori physiological information. An important assumption to derive physiological information from this kind of model applied to PET data, is that the tracer does not alter or perturb the system under study. Three different classes of techniques can be used to perform quantificaiton of PET dynamic images: input-output models, graphical methods and compartmental models.

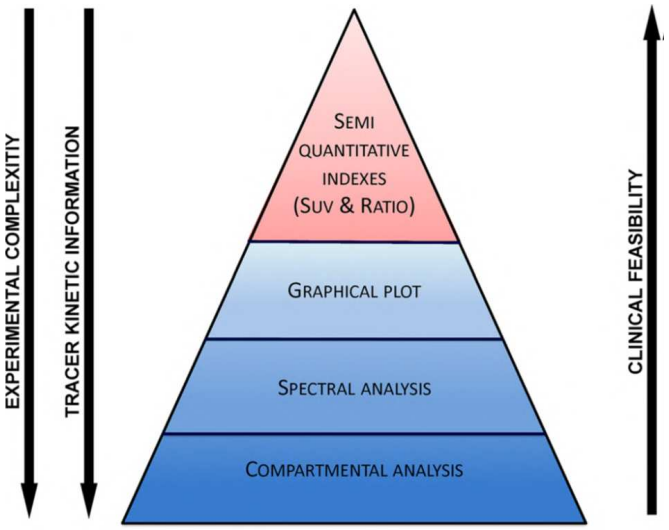

Figure 1.2: Hierarchical representation of the different methods used for quantitative or semi-quantitative PET image analysis [6]

In figure 1.2, the most frequently used quantification techniques are categorized, ordered in such a way that for each method, the trade-off between the conditions necessary for the application and the parameters returned as output is explained.

Static PET

The standardized uptake value (SUV) is a semi-quantitative index commonly employed in static PET for therapeutic applications. SUV quantifies tracer uptake in a region of interest (ROI) or voxel and normalizes it to the injected dose and a normalization factor (NF) determined by the subject's characteristics such as body weight, body surface area, and lean body mass. SUV is suited for clinical usage with a variety of PET tracers due to its simplicity and versatility, and it does not require arterial cannulation, making it widely used in clinical routine [6].

$$SUV = \frac{radiotracer\ concentration}{\frac{injected\ dose}{NF}} \tag{1.1}$$

The radiotracer concentration (e.g., kBq/ml) represents the concentration measured with PET during a brief interval (typically 5 to 15 minutes) after an established period (e.g., 45 or 60 minutes) following tracer administration. The total administered dose is the injected dosage (e.g., MBq), and the NF depends on which is the normalization unit (e.g. body weight in kg). Despite the simplicity of the index and its widespread use in oncology for diagnosis and tumor staging, its reproducibility is subject to various technical and physiological factors [24].

Dynamic framework quantification

Regarding the dynamic PET framework, input-output models, graphical methods and compartmental models are the most frequently used, and a quantification step is needed to derive meaningful physiological parameters. The first two methods require analysis under a steady-state condition, whereas compartmental analysis is employed to derive quantitative information from dynamic PET scans. This method is based on a mathematical model of the physiological processes that regulate tracer kinetics. It requires assessing a linear or nonlinear structure with a set number of compartments and their interconnections. The chosen structure, which often explains the complex operation of the system, must have a strong foundation in biochemistry and physiology. Therefore, the method enables a

complete description of the system kinetic and lead to a deep knowledge of the process that eventually can be crucial to clinical assessment of a pathology or disease.

1.3 [18F]FDG PET kinetic

One of the most commonly used radioligands to trace regional glucose metabolism is [18F]Fluorodeoxyglucose ([18F]FDG) .

The first tracer for glucose metabolism was [11C]glucose, but the model used to interpret its tissue activity must take into account the difficulties of its kinetics, explicitly considering its metabolic byproducts through glycolysis and glycogen synthesis pathways.

To overcome the challenges posed by the complexity of [11C]glucose kinetics, an alternative approach, based on [18F]FDG, was developed by Sokoloff and colleagues and employed in brain studies [9]

[18F]FDG competes for facilitated transport sites with glucose and for phosphorylation with hexokinase, resulting in [18F]FDG-6-phosphate ([18F]FDG-6-P) formation. The key advantage of this analogue lies in the fact that [18F]FDG-6-P becomes trapped in the tissue and is released very slowly (in other words, [18F]FDG-6-P cannot undergo further metabolism), while glucose-6-P undergoes further metabolism along the glycolysis and glycogen synthesis pathways.

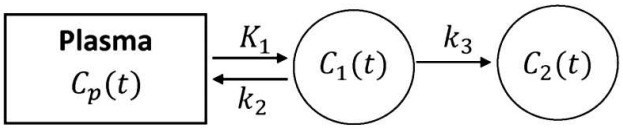

Figure 1.3: The two-compartment three rate constant model for quantifying [18F]FDG glucose analogue [9]

The figure 1.3 illustrates Sokoloff et al.'s 3K model for [18F]FDG kinetics. Every compartment, illustrated as a circle, is conceptualized as a volume of well-mixed and kinetically homogeneous material. It is defined by a set of first-order differential equations that vary with time, eq. 1.2. In this model, $C_p(t)$ represents the plasma arterial concentration of [18F]FDG, $C_1(t)$ represents the tissue concentration of [18F]FDG, $C_2(t)$ represents the concentration of [18F]FDG-6-P in tissue. The microparameters K_1 and k_2 describe the kinetics of [18F]FDG transport across the membrane in the forward and reverse directions, while k_3

represents the rate constant for [^{18}F]FDG phosphorylation. By utilizing arterial plasma samples and dynamic PET images, it becomes possible to estimate these microparameters within the model. The microparameters k_2 and k_3 are expressed in [min $^{-1}$], while the K_1 is highlited in capital letter because the unit of measurement is expressed in [ml/cm3/min] or [ml plasma/ml tissue/min].

It is observed that the connection between $C_1(t)$ and $C_2(t)$ is unidirectional: the phosphorylation process is definitive, and the tracer cannot return to the previous form in $C_1(t)$. Therefore, (compartment $C_2(t)$) the tracer is defined irreversible. It is worth noting that there is also a version of the compartmental model that takes into account the dephosphorylation of [^{18}F]FDG-6-P after 120 minutes from the tracer injection, adding a fourth rate constant, k_4, which links the process from $C_2(t)$ to $C_1(t)$ [10].

$$\begin{aligned} \dot{C_1}(t) &= K1C_p(t) - (k2 + k3)C_1(t) \quad C_1(0) = 0 \\ \dot{C_2}(t) &= k3C_2(t) \qquad\qquad\qquad\qquad C_1(0) = 0 \end{aligned} \tag{1.2}$$

The measurement equation is defined in eq.1.3: $C_{tissue}(t)$ describes the total amount of radioactivity measured from the PET scanner after injection of the [^{18}F]FDG tracer. It also takes into account the measurement of radioactivity in the volume of blood present within the tissue, V_b.

$$C_{tissue}(t) = (1 - Vb)(C_1(t) + C_2(t)) + V_bC_b(t) \tag{1.3}$$

1.4 Input Function

Arterial sampling is considered to be the gold standard for obtaining the arterial input function of the model. However, the procedure is invasive, technically demanding, and has a minor risk of adverse effects. This could lead to patient discomfort and potentially expose them to the risk of injuries, including arterial thrombosis in severe cases [29]. Additionally, the technical staff responsible for sample collection may face radiation exposure and the processing of these samples requires specific laboratory procedures, which could dramatically raise the costs associated with dynamic acquisitions and limit their use in clinical settings.

Accurate measurement of the concentration of the parent radioligand in plasma is a challenging task in quantitative PET imaging. Injected radiolabeled compounds can undergo chemical changes, producing radiometabolites that must be

considered to ensure accurate quantification of radioligand binding. The behavior of radiometabolites depends on the tissue with which they interact. The process begins with the collection of blood samples from the patient, from which the radioactive activity is measured using a gamma counter, resulting in $C_b(t)$. Subsequently, through a centrifugation procedure, the separation between blood and plasma is carried out, and using the same gamma counter instrument, the total radioactivity present in the plasma, called $C_tot(t)$, is measured. For tracers that generate metabolites (such as [^{18}F]FDG, [5]), it is necessary to calculate the fraction of the unchanged compound, called plasma parent fraction (PPf), which represents the proportion of radioactivity attributed exclusively to the original compound, and this is estimated through high-performance liquid chromatography (HPLC). Due to the rapid decay of radioactivity, mathematical functions are often used to fit PPf data points, creating a smooth curve from discrete noisy samples. Choosing an appropriate PPf model is crucial for kinetic modeling and can significantly impact the results. Only then $C_p(t)$ can be obtained: this is the quantity directly used in the model as a forcing function, eq 1.3, that undergoes under the important assumption that its time activity curve is noise-free.One of the hypotheses for applying compartmental modeling is that the input function must be noise free: for this reason, a model based denoising needs to be applied to the measured arterial input [32, 2].

Image Derived Input Function

The image-derived input function (IDIF) is seen as a promising noninvasive alternative to arterial sampling, eliminating the need for invasive and expensive procedures like arterial cannulation, blood handling, analysis, and reducing radiation exposure to research personnel. One of the issues that arises is partial volume effects, which result from the presence of tissue heterogeneity within a single voxel or ROI, complicating quantitative analysis via mathematical modeling.

While IDIF has been effectively validated using major blood vessels like the heart, aortic segments, and femoral arteries, which are easily manageable with regard to partial volume effects [12], in brain PET studies, where these large vessels are not always within the imaging field, using intracranial blood vessels, primarily the carotid arteries, which are relatively small compared to the spatial resolution of modern PET cameras, introduces two significant partial volume effect artifacts. These include the 'spill-out' effect, leading to underestimation

of the input function, and the 'spill-in' effect, resulting in artificial elevation of carotid activity and potential alterations in the curve shape.

To obtain an accurate input function estimate, correcting both these effects is essential. An important drawback of IDIF is its inability to differentiate between the original compound and its radioactive metabolites, as well as to distinguish plasma radioactivity from that of whole blood [12]. Since [^{18}F]FDG does not produce any radiometabolites, this additional step is not required, and partial volume correction is ideally sufficient to estimate plasmatic concentration. Occasionally, individual metabolite correction can be effectively incorporated into the IDIF process, but it still requires a limited number of blood samples. Therefore, the primary advantage of using IDIF over an arterial input function would be a decreased reliance on arterial blood sampling. To avoid blood sampling completely, a common metabolite curve can be used. However, this approach's applicability depends on the tracer and must be verified for each specific case[11]. Other alternatives are provided by venous samples,which also play a role in the partial volume effects correction process[[16]. Because its kinetics differs from the arterial one, venous samples can replace arterial samples only within a limited time window of varying duration, which needs to be evaluated individually for each tracer. In the case of [^{18}F]FDG, is typically achieved approximately 10 to 15 minutes after injection, allowing for the use of venous samples in calculating the IDIF [16]. Other methods, distinct from IDIF, such as population-based input function (PBIF) and simultaneous estimation of the input function (SIME), are under examination. With further validation and the resolution of certain methodological challenges, these two approaches have the potential to provide a less invasive means of estimating the input function for certain tracers.

1.5 Quantification of microparameters at Voxel level

Microparameters relative to the compartmental model described in section 1.3 can be estimated either at voxel level or region-level (ROI). Higher signal-to-noise ratios (SNR) are a benefit of ROI-level analysis, which enables more accurate and precise numerical estimation of model parameters, as the mean information of voxels within the ROI is employed, thus enabling a significant reduction in noise. On the other hand, the loss of the original spatial resolution and the implicit assumption that heterogeneity within the same ROI is not important for

the results, are both disadvantages of ROI level analysis.

Voxel-wise quantification based on complete kinetic modeling overcomes these limitations; the analysis performed at voxel level is enabled through the generation of parametric maps, which can entirely account for the spatial heterogeneity of the physiological processes under study. Certain occurrences, like a lesion within a limited section of an anatomical structure, might remain undetectable when analyzing ROIs, but with the use of voxel-wise parametric maps they can be easily visible even through basic visual examination.

However, the low SNR of TACs collected from individual voxels presents challenges for quantification based on full kinetic modeling. Starting from the parameter estimation, the gold standard for ROI-based quantification is the weighted nonlinear least squares estimators (WNLLS), but because of its overly sensitivity to noise, the use of non-linear estimators at voxel level (which are affected by a higher noise), is difficult and highky demanding, leading to a high computational cost, convergence issues and sensitivity to initial estimates. Consequently, parameter estimates are affected by low precision and accuracy.

Thus, the development of reliable and general-purpose parametric imaging methods remains a challenge for dynamic quantitative PET imaging. Therefore, it is evident that there is a need for more robust and computationally less complex algorithms, particularly at the voxel level. Several alternatives to WNLLS are available, such as Generalized Least Square (GLS) method, basic function method, and global two-stage method [6]. In the case of graphical methods, it is possible to overcome the computational complexity hurdle, providing reliable estimates even at the voxel level due to the simplified model complexity, but they often do not return any information on the micro-parameters, such as individual compartmental rate constants of the model. There is also a class of estimators based on Bayes's theorem, which include prior information on tissue kinetics and have been adopted in the PET community, showing the potential to provide robust estimates even at the voxel level. However, many Bayesian methods proposed so far lack the necessary flexibility to be applied to all common compartmental models, and when they can, their clinical applicability is hindered by the extensive computational time required for analyzing whole-brain dynamic PET scans. The main challenge with any Bayesian approach lies in computing the posterior distribution using Bayes' rule, defined as :

$$f_{p|z}(p|z) = \frac{f_{z|p}(z|p) f_p(p)}{f_z(z)} \tag{1.4}$$

where the posterior parameter distribution is denoted as $f_{p|z}(p|z)$, the prior expectations of parameter values are formalized as the prior distribution $f_p(p)$, where p represents the parameter vector of our model and z is the observed data. Bayes estimators strike a balance between a priori and a posteriori information, corresponding to expectations and data, respectively.

Bayesian estimator presents certain algorithmic complexities:

- In general cases, the a posteriori probability density is determined through the Markov Chain Monte Carlo (MCMC) method. This approach can be technically demanding, involving challenges related to convergence, and it demands significant computational resources, which is beyond the scope of this course.
- Analytical accessibility of the a posteriori probability density, enabling point estimates via optimization, is feasible only under specific assumption.

A possible solution to simplify this computation is the Variational Bayesian (VB) method, which is a fully Bayesian approach that utilizes an analytical approximation to streamline the calculation of the posterior distribution . However, despite the robustness of the results, the reduced computational cost, and the potential benefits in clinical applications [18], the construction of prior information largely depends on the operator's expertise, and the results are significantly influenced by that.

A simpler alternative to VB may be represented by Maximum A Posteriori (MAP) estimator. In case of PET studies, parameter estimation based on MAP can rely on a simplified prior structure, which is derived from ROI-level analysis.

Previous studies showed the potential benefits of applying a Bayesian approach on PET quantification. [19, 20, 21, 22, 23].

1.6 Patlak Graphical Method

Patlak plot is a graphical method for an irriversible tracer with a kinetic described by a a two tissue compartmental model (2TCM) and three rate constans, K1, k2 and k3, originally developed for quantification of [18F]FDG PET studies [30]. Graphical methods refer to techniques that involve transforming the data in such a way that, over time, the data display a linear pattern where the slope can be linked to the parameter under investigation. The linear trend reflects the fact that an equilbrium state between plasma and compartment has been reached.

The Patlak method allows for the estimation of the macroparameter K_i, which is defined as the fractional uptake of [18F]FDG and measured in (ml/cm^3/min). This parameter is linked to the other microparameters that describe the compartmental model through the following equation:

$$K_i = \frac{K_1 k_3}{k_2 + k_3} \tag{1.5}$$

When K_i is known it is possible to derive the cerebral metabolic rate of glucose (CMRglc)

$$CMRglc = K_i \frac{C_{p-g}}{LC} \tag{1.6}$$

with C_{p-g} that indicate the subject's glycemia measured at at the beginning of the PET session; LC is the lumped constant, which is tissue dependent and describes the relation between the glucose analogue and the glucose itself. The estimation of K_i is possible because, when tissue and plasma are at the equilibrium, data can be modeled as in the equation below:

$$\frac{C_{tissue}(t)}{C_p(t)} = K_i \frac{\int_0^t C_p(\tau) d\tau}{C_p(t)} + q \qquad t > t^* \tag{1.7}$$

This requires the assumption that there is at least one irreversible compartment. The time when the equilibrium for all the reversible compartments in the system happens is conventionally known as t*.

Graphically, the parameter of interest, K_i, is the slope of the line in figure 1.4

Due to the linearity of equation 1.7, a linear estimator, which is much faster and more robust to noise than NLLS, can be applied and provide reliable voxel-level estimates.[3]

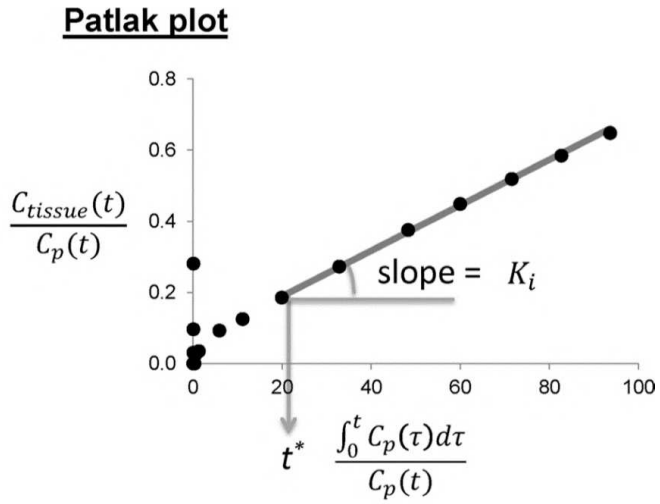

Figure 1.4: Patlak graphical plot. The data show a linear trend after the equilibrium time t* and the slope corresponds to the estimated parameter K_i.

1.7 Aim of the study

In this thesis project, the quantification of [18F]FDG microparameters was examined. A new approach based on a MAP estimator was tested, where the prior information is obtained using ROI-level estimates coming from an anatomical atlas. Moreover, model complexity was reduced by exploiting additional a priori information coming from Patlak's graphical analysis. Furthermore, the impact of using IDIF extracted from different vascular ROIs was examined.The performances of the MAP estimator were also compared to the ones obtained using Variational Bayes.

Chapter 2

Materials and methods

2.1 Dataset / Materials

2.1.1 [^{18}F]FDG PET data

60 min Dynamic [18F]FDG PET acquisitions coming from 10 subjects (age 58 ± 19, 6 male and 4 female, height 167 ± 9 cm, weight 67 ± 12 Kg, injected dose 194 ± 40 MBq), affected by glioma were obtained using a hybrid PET/MR 3T Siemens Biograph scanner at the University Hospital of Padova. PET dynamic images were reconstructed using the ordered subset expectation maximization (OSEM) algorithm starting from list mode data. The following reconstruction grid was employed: 10x6s, 8x15s, 9x60s, 12x240s, figure 2.1. Images are 256x256x127 matrices (voxel size: 2.8 mm x 2.8 mm x 2.0 mm). Venous blood samples were not provided for this study. No spatial smoothing was performed on the final images.

2.1.2 MRI data

Simultaneously with PET acquisition, subjects underwent a structural MR scan consisting in a 3D T1w Magnetization Prepared-Rapid Gradient Echo (TR/TE 2400/3.2ms, voxel size 1x1x1mm3). Data was processed using an in-house pipeline, which included bias field correction (N4BiasFieldCorrection [38]), skull-stripping (MASS [39]) and nonlinear diffeomorphic registration [40] to the symmetric MNI152 FSL atlas [41] and finally a segmentation into gray matter (GM), white matter (WM), and cerebrospinal fluid (CSF), using SPM and generating the probability map for each tissue. Then, the segmentations were linearly mapped from T1w to PET space.A coregistration step of the Hammers Atlas in the T1 image space

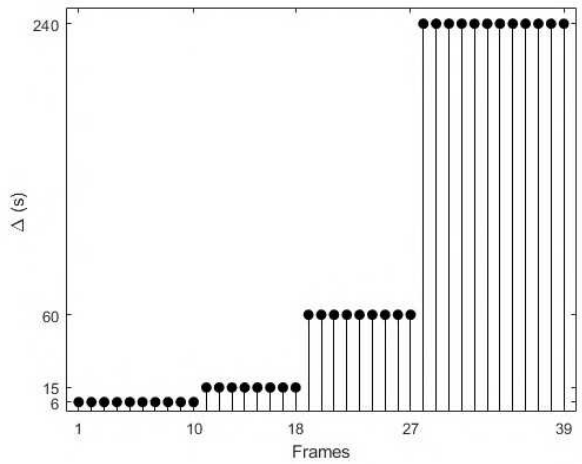

Figure 2.1: PET reconstruction time grid.

was performed. Finally, the inverse matrix is then used to apply to the Hammers Atlas to align it with the PET image.

2.1.3 Input function

The input functions were extracted using EMATA [27], a toolbox which automatically performs IDIF extraction directly from [18F]FDG PET images, and additionally includes a PVE correction procedure that does not require any blood sampling [26]. IDIF were extracted both from the ICA (and in particular from the siphons portion) and from the CCA.[12, 36].

Model-based denoising was applied to denoise both the plasmatic curves [25]. Spillover correction was applied using Chen's method[17]. Since venous samples were not available, they were predicted from subjects' covariates, exploiting the non-linear mixed effect model by Volpi and colleagues [26].

2.2 Data analysis

2.2.1 Grey Matter mask

The tissue masks contain, for each tissue, the probability that a given voxel belongs to that tissue type. High probabilities were assigned to cases where intensities clearly represent either white matter or gray matter. Intermediate probability values are used to indicate partial volume effect, which occurs when a voxel spans more than one type of tissue. For our analysis, only the GM is

considered.

Since the analysis was focused on gray matter, only voxels with a GM probability value greater than 0.8 were included, in order to minimize partial volume effect between GM and WM.

2.2.2 Measurement Error

Throughout the discussion, the measurement error for the observed PET TACs was assumed to have certain statistical properties. More specifically, noise is assumed to be additive, uncorrelated and to follow a Gaussian distribution with zero mean. The noise covariance, Σ_v, is represented by a matrix, which entries are calculated according to the following formula [31]:

$$\sigma_k^2 = \rho^2 \frac{C_i^{obs}(t_k)}{\Delta t_k} \tag{2.1}$$

where $C_i^{obs}(t_k)$ represents the observed mean value of the tracer activity over the $k^(th)$ relative time scan interval Δt_k, and ρ^2 is an unknown proportionality constant. In PET applications, the use of a non-uniform sampling grid means that the scintillation crystals remain active for varying duration within each measured sample. This enables them to record pairs of photons emitted by the tracer, with the duration of each time frame chosen to ensure a sufficient number of decay events are detected for image reconstruction. Consequently, the noise level varies at different time points [18].

Observing equation 2.1, larger time frames Δt_k result in smaller errors, implying more reliable measurements. However, this idea is not feasible when dealing with rapidly changing dynamics, especially in the initial part of the TAC dynamics, figure 2.1, where a denser sampling grid with smaller Δt_k is required to accurately approximate the instantaneous measurement $C_i^{obs}(t_k)$ at that specific time [32]. A wider time interval is acceptable in the second part of the TAC, as the curve exhibits less rapid changes and to compensate for the minor decay in the late time activity curve. Nonetheless, even in this case, the time interval cannot be too large, as it affects the estimated activity in that time span, leading to deterioration of the signal [33].

Consequently, an optimal weighting consistent with [34] was used to define the objective function during parameter estimation:

$$w_k = \frac{\Delta t_k}{C_i^{obs}(t_k)} \tag{2.2}$$

and the constant ρ^2 is calculated a posteriori:

$$\rho^2 = \frac{WRSS}{n-m} \tag{2.3}$$

where *WRSS* represents the Weighted Residual Sum Square of the model fit regarding data, n is the number of samples, and m is the complexity of the model used, i.e., the number of parameters to be estimated.

2.2.3 Patlak Graphical method

Optimal choiche of t*

In order to proceed with the estimation of the [^{18}F]FDG fractional uptake parameter, K_i, it is necessary to define a time point t* starting from which the relationship between $C_{tissue}(t)/C_p(t)$ and $\int_0^t C_p(\tau)d\tau/C_p(t)$ is approximately linear, equation 1.7.

A subset of ROI level TACs from the Hammers atlas were selected as reference to optimally identify the t* : "L Thalamus," "R Thalamus," "L Superior frontal gyrus," "R Superior frontal gyrus," "L Cuneus," "R Cuneus," "L postcentral gyrus," "R Postcentral gyrus". A grid-search approach was employed, repeating the WLLS estimation for each candidate t. Starting from time *4.5* minute, i.e. corresponding to sample 20 out of the total 39 provided by the scan, we proceed backward until we meet the condition of a minimum number of samples, which is set to 6. This is necessary to ensure an adequate number of time points for a reliable estimation of K_i.

For each candidate, the K_i and the q constant, described in eq 1.7, represented by a linear regression model, were estimated using the weighted least square, where the weights were used coherently with 2.2.2. Once the parameters were identified, t* was chosen from among those that generated the best fit of the data by the model. The t* corresponding to the best fit was selected, i.e. the model with the highest coefficient of determination R^2, defined as:

$$\rho_{\hat{Y}Y} = \frac{Cov(\hat{Y}, Y)}{\sigma_{\hat{Y}}\sigma_Y} \tag{2.4}$$

$$R^2 = {\rho_{\hat{Y}Y}}^2 \tag{2.5}$$

This procedure was repeated for each region and for each input function. The average t* across all regions and inputs was adopted as the optimal value and used for the ROI level and voxel level analysis.

Patlak ROI level

The next step was to estimate Ki at the ROI level for each of the regions in the Hammers atlas and for each Input function. The estimation followed the same approach as described above, using WLLS and the same data weighting approach. Subsequently, the standard deviation of the estimates and their Coefficient of Variation (CV) were calculated.

Patlak voxel level

The same procedure described above was carried out at the voxel level for each input function.

2.2.4 ROI Level: microparameters estimation

In this section, the procedure for estimating the microparameters K_1, k_2, k_3, and Vb at the ROI level of the 1.2 model is described.

Model Description

The model representation is provided through a state-space model:

$$\begin{cases} \dot{x}(t) = Ax(t) + Bu(t) \\ y(t) = Cx(t) + Du(t) \end{cases} \tag{2.6}$$

where x is the state vector, u is the input vector, and y is the output vector. A, B, C and D are the state-space matrices that express the system dynamics.

The state vector x is described by the system of differential equations in eq. 1.2; u represents the input function, which for this projects corresponds to the different IDIFs which were tested.

Since the measurement equation (1.3) also requires the knowledge of the $C_b(t)$, we tested two different approaches.

-) We used the equation below to derive the $C_b(t)$ from the $C_p(t)$:

$$C_b(t) = C_p(t)(1 - 0.3 * H) \tag{2.7}$$

where H represents the hematocrit, that is usually subject dependent. However, since this measurment was not provided with our data, we set H to 0.8 [35].

The system in 2.9 then becomes:

$$\begin{cases} \begin{bmatrix} \dot{C}_1(t) \\ \dot{C}_2(t) \end{bmatrix} = \begin{bmatrix} -(k_2 + k_3) & 0 \\ k_3 & 0 \end{bmatrix} \begin{bmatrix} C_1(t) \\ C_2(t) \end{bmatrix} + \begin{bmatrix} K_1 \\ 0 \end{bmatrix} \begin{bmatrix} C_p(t) \end{bmatrix} \\ \\ \begin{bmatrix} C_{tissue}(t) \end{bmatrix} = \begin{bmatrix} (1 - Vb) & (1 - Vb) \end{bmatrix} \begin{bmatrix} C_1(t) \\ C_2(t) \end{bmatrix} + \begin{bmatrix} Vb \end{bmatrix} \begin{bmatrix} C_p(t)(1 - 0.3 * H) \end{bmatrix} \end{cases} \tag{2.8}$$

- Additionally, we set: $C_b(t) = C_p(t)$, and the following system of equation is used to model the data:

$$\begin{cases} \begin{bmatrix} \dot{C}_1(t) \\ \dot{C}_2(t) \end{bmatrix} = \begin{bmatrix} -(k_2 + k_3) & 0 \\ k_3 & 0 \end{bmatrix} \begin{bmatrix} C_1(t) \\ C_2(t) \end{bmatrix} + \begin{bmatrix} K_1 \\ 0 \end{bmatrix} \begin{bmatrix} C_p(t) \end{bmatrix} \\ \\ \begin{bmatrix} C_{tissue}(t) \end{bmatrix} = \begin{bmatrix} (1 - Vb) & (1 - Vb) \end{bmatrix} \begin{bmatrix} C_1(t) \\ C_2(t) \end{bmatrix} + \begin{bmatrix} Vb \end{bmatrix} \begin{bmatrix} C_p(t) \end{bmatrix} \end{cases} \tag{2.9}$$

Parameters estimation

The microparameters of the model were identified using WNLLS, setting initial values and lower and upper bounds for the estimation as specified in table 2.1. The error covariance matrix was built as described in section 2.2.2, with the signal value $C_i^{obs}(t)$ corresponding in this case to the TAC of each *i-th* ROI. Finally, the precision of the estimated parameters was calculated.

Table 2.1: Initial values and bound for parameters estimation algorithm.

Microparameters	***Initial estimates***	***Lower bound***	***Upper Bound***
K1 [ml/cm^3/min]	0.1	0	1
k2 [min^{-1}]	0.3	0	3
k3 [min^{-1}]	0.1	0	1
Vb [adim]	0.05	0	0.5

2.2.5 ROI Level: microparameters estimation with constraint on k_3

The ROI level estimation was also repeated using a reduced set of parameters, by exploiting the results of Patlak Graphical Analysis. More specifically, k_3 was calculated a posteriori using Patlak's K_i. This allows us to reduce the complexity of the model, enabling the estimation of a lower number of parameters.Furthermore, as evident in [36], the tail of the IDIF may differ when varying the extraction site or the PVE correction, and this can be reflected in the late dynamics of the PET signal described by the k_3 .The type of IDIF, in any case, also influences the K_i parameter because the value estimated depends on the area under the curve of the $C_p(t)$, as described in section 1.6.

The constraint was imposed, for each ROI, due to eq 1.5:

$$k_3 = \frac{K_i k_2}{K_1 - K_i} \tag{2.10}$$

The constraint is applied to reduce the model complexity and, as a consequence, to obtain estimates with higher precision.

Model Description

The implementation of the model remains similar to section 2.2.4; the only modification is relative to the state-space matrix A. The first equation of the systems 2.8, 2.8 will, therefore, be:

$$\begin{bmatrix} \dot{C}_1(t) \\ \\ \dot{C}_2(t) \end{bmatrix} = \begin{bmatrix} -(k_2 + \frac{K_i k_2}{K_1 - K_i}) & 0 \\ \\ \frac{K_i k_2}{K_1 - K_i} & 0 \end{bmatrix} \begin{bmatrix} C_1(t) \\ \\ C_2(t) \end{bmatrix} + \begin{bmatrix} K_1 \\ \\ 0 \end{bmatrix} \begin{bmatrix} C_p(t) \end{bmatrix} \tag{2.11}$$

Parameters estimation

The microparameters of the model were identified,as above, using WNLLS and setting initial values and lower and upper bounds for the estimation as specified in table 2.1. k_3 is calculated a posteriori, using 2.10.

2.2.6 Voxel level: microparameters estimation with MAP

In this section, we delve into the estimation of microparameters at the voxel level, which remains the ultimate goal of this thesis.

Model Description

The definition of the model is similar to what was discussed in the previous chapter regarding the ROI-level analysis, section 2.2.4. all the analysis described in the next paragraphs were repeated twice, for each of the two approximations of $C_b(t)$, models 2.8 and 2.9.

Parameter estimation

To perform parameters estimation at Voxel level, the proposed solution involves the use of the *Maximum A Posteriori*, a Bayesian estimator that can incorporate prior information to guide parameter estimation.

The formulation of the estimator starts from a generic measurement z_k , which in our case correspond to the signal at time t_k from the PET scan, corrupted by noise measurement, and can be represented as follows:

$$z_k = y_k(t_k) + v_k = g(t_k, \boldsymbol{p}) + v_k, \qquad K = 1, ..., N \tag{2.12}$$

the error-free measurable signal, y_k, is described by a generic model y = g(t,p), where $g(\cdot)$ depends on the specific model equation, and $\boldsymbol{p}$ is the parameter vector. The term v_k takes into account the measurement error, assumed to be additive, Gaussian with zero mean, and with covariance described by the equation 2.1.

Starting from the Bayes' rule, described in Section 1.5, eq. 1.4, the MAP estimator relies on the maximization of the a posteriori PDF:

$$\hat{\rho}_{MAP} = \arg\max_{p} f_{p|z}(p|z) \tag{2.13}$$

by replacing $f_{p|z}(p|z)$ in Equation 2.13 with the expression from Equation 1.4. Disregarding the denominator of the objective function $f_z(z)$ in the maximization problem (since it is independent of $\boldsymbol{p}$), the MAP estimator can be computed as:

$$\hat{\rho}_{MAP} = \arg\max_p f_{z|p}(z|p) f_p(p) \tag{2.14}$$

Under the assumptions we have imposed of Gaussian noise and a f_p has a Gaussian distribution, it is therefore possible to analytically handle the posterior probability density and, as a result, solve the estimation problem as an optimization problem. Then, eq. 2.14 can be simplified:

$$\hat{\rho}_{MAP} = \arg\min_p J_{MAP}(p) \tag{2.15}$$

where the cost function $J_{MAP}(p)$ is defined as:

$$J_{MAP}(p) = [y - G(p)]^T \Sigma_v^{-1} [y - G(p)] + (p - \mu_p)^T \Omega^{-1} (p - \mu_p) \tag{2.16}$$

With this formulation, the focus shifts from deriving the posterior distribution, which is cumbersome, to minimizing a cost function, while incorporating the available prior information. The first term, which measures the goodness of fit or the adherence to the a posteriori information, while the last term reflects the adherence of the estimate to the available a priori knowledge about the parameter vector. The microparameter estimates derived from the ROI model fitting serve as a priori information for guiding the voxel level estimates. For each voxel belonging to the *i-th* region of the Hammers atlas, the corresponding ROI-level estimate was used as prior, indicated as μ_p, and their covariance Ω provided by their precision (see eq. 2.17. The measurement error Σ_v was consistent with what was described in section 2.2.2, with the signal value $C_{obs}(t)$ corresponding to the average TAC of the GM.

$$\mu_p = \begin{bmatrix} \tilde{K_1^i} \\ \tilde{k_2^i} \\ \tilde{k_3^i} \\ Vb^i \end{bmatrix} \qquad \Omega = \begin{bmatrix} var(\tilde{K_1^i}) \\ var(\tilde{k_2^i}) \\ var(\tilde{k_3^i}) \\ var(\tilde{Vb^i}) \end{bmatrix} \tag{2.17}$$

Noisy data with a high Σ_v value of the noise vector v lead the estimator to consider the information provided by the prior more reliable, compared to the data. Conversely, an non-sufficiently informative prior lead to an high Ω, causing the estimator to favor a better model fit with the data.

2.2.7 Voxel level: microparameters estimation with MAP and constraint on k_3

The constraint on the parameter k3 was also applied for voxel-level estimation, as described in Section 2.2.5.

Model Description

The definition of the model is similar to what was discussed in the previous chapter at the ROI level with the constrain, section 2.2.5, model 2.11 .

Parameters estimation

The microparameters of the restricted model,K_1, k_2 and Vb, were identified as above, using MAP estimator, setting initial values and lower and upper bounds for the estimation as specified in table 2.1. k_3 is calculated a posteriori, using equation2.10.

2.3 Comparison with Variational Bayes results

The final step involves a comparison between the results provided by MAP estimator (with and without constraint) and the maps obtained using VB approach. The results were compared both by visual inspection of the parameter distribution and by computation of the Spearman correlation coefficient for each pair of maps.

Chapter 3

Results

The graphs and results of all subjects are stored in the DEI's storage:
$\backslash nfsd\backslash biopetmri4\_tesi\backslash LaddomadaPietro\_2023\backslash DATA\_processed\backslash$

3.1 Patlak Graphical method

3.1.1 Analysis of the t*

The search for the optimal t* has produced a range of results specific for each subject, summarized in the Table 3.1. From a graphical example in figure 3.1, 3.2 and 3.3, subjects *n° 2, 5, 9*, it can be observed how the proposed selection method in the section 2.2.3 produces satisfactory results. It's possible to confirm even through visual analysis that the choice of t* is suitable for the linearization of the model described in 1.6. In fact, the curves exhibit a linear trend for t>t*.

Table 3.1: Optimal Patlak t for each subject

Subject	***t* Patlak [min]***
001	14
002	18
003	10.5
004	11.5
005	11.5
006	11.5
007	14
008	11.5
009	10.5
010	14
mean value	*12.7 ± 2.3*

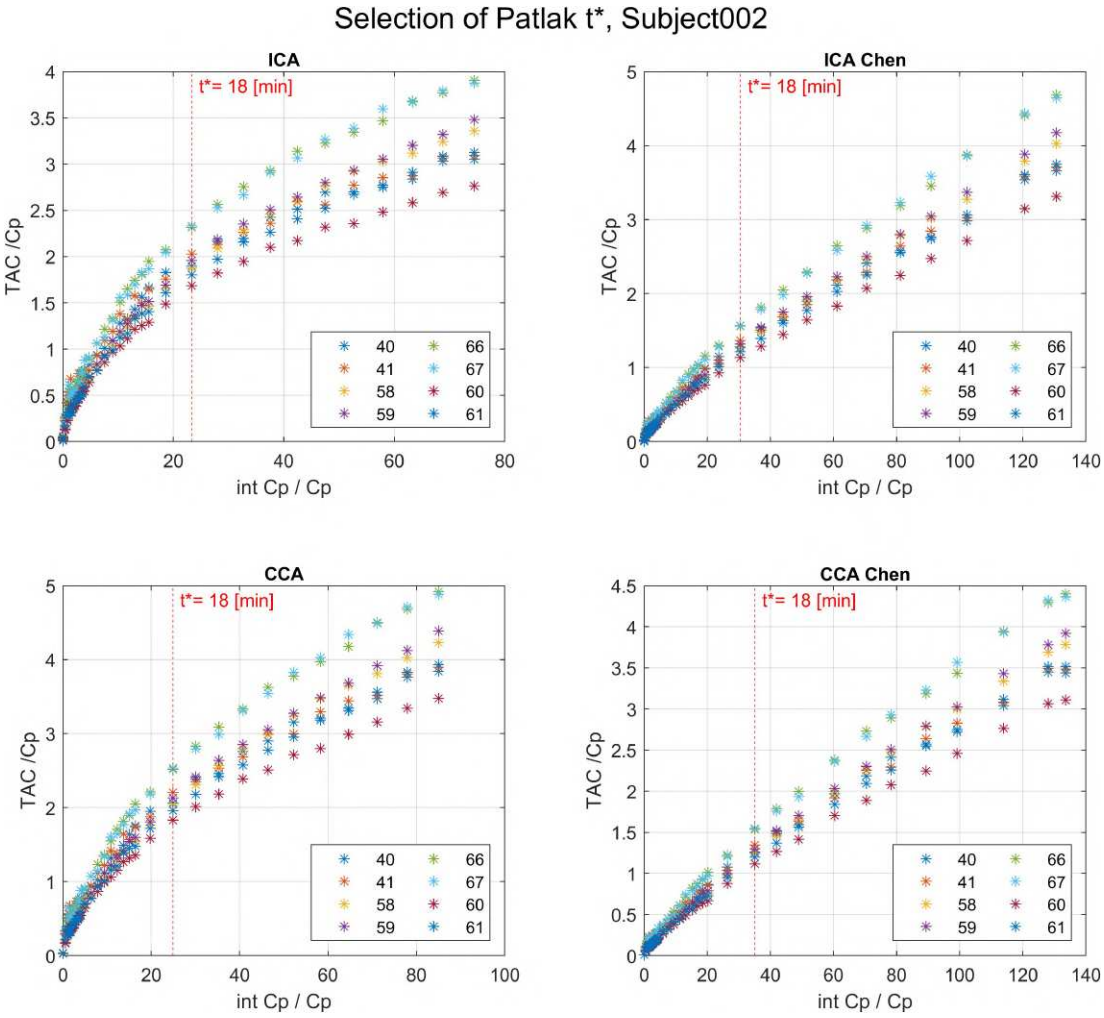

Figure 3.1: Patlak graphical plot for tested regions: each number refers to the region according with Hammers Atlas. Optimal t*, subject 002.

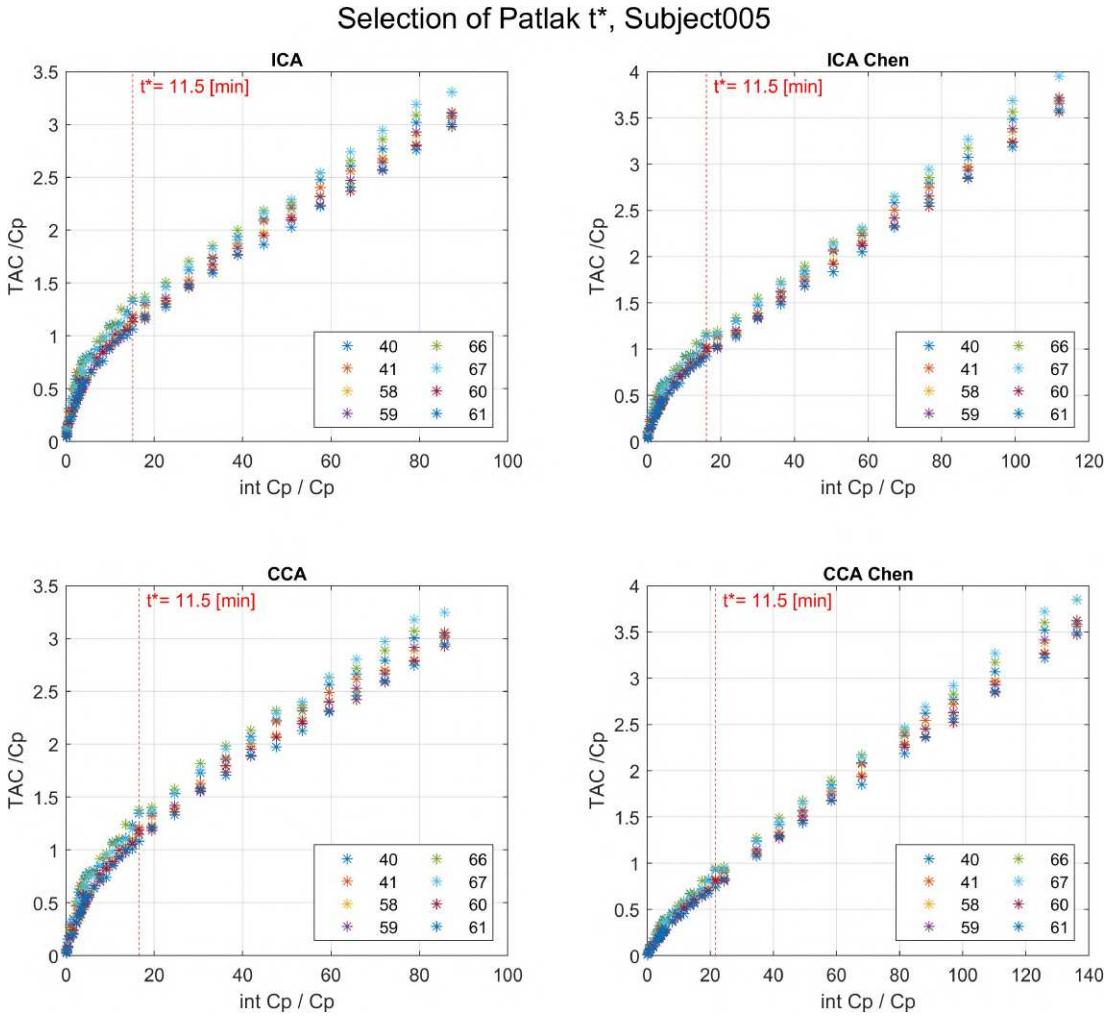

Figure 3.2: Patlak graphical plot for tested regions: each number refers to the region according with Hammers Atlas. Optimal t*, subject 005.

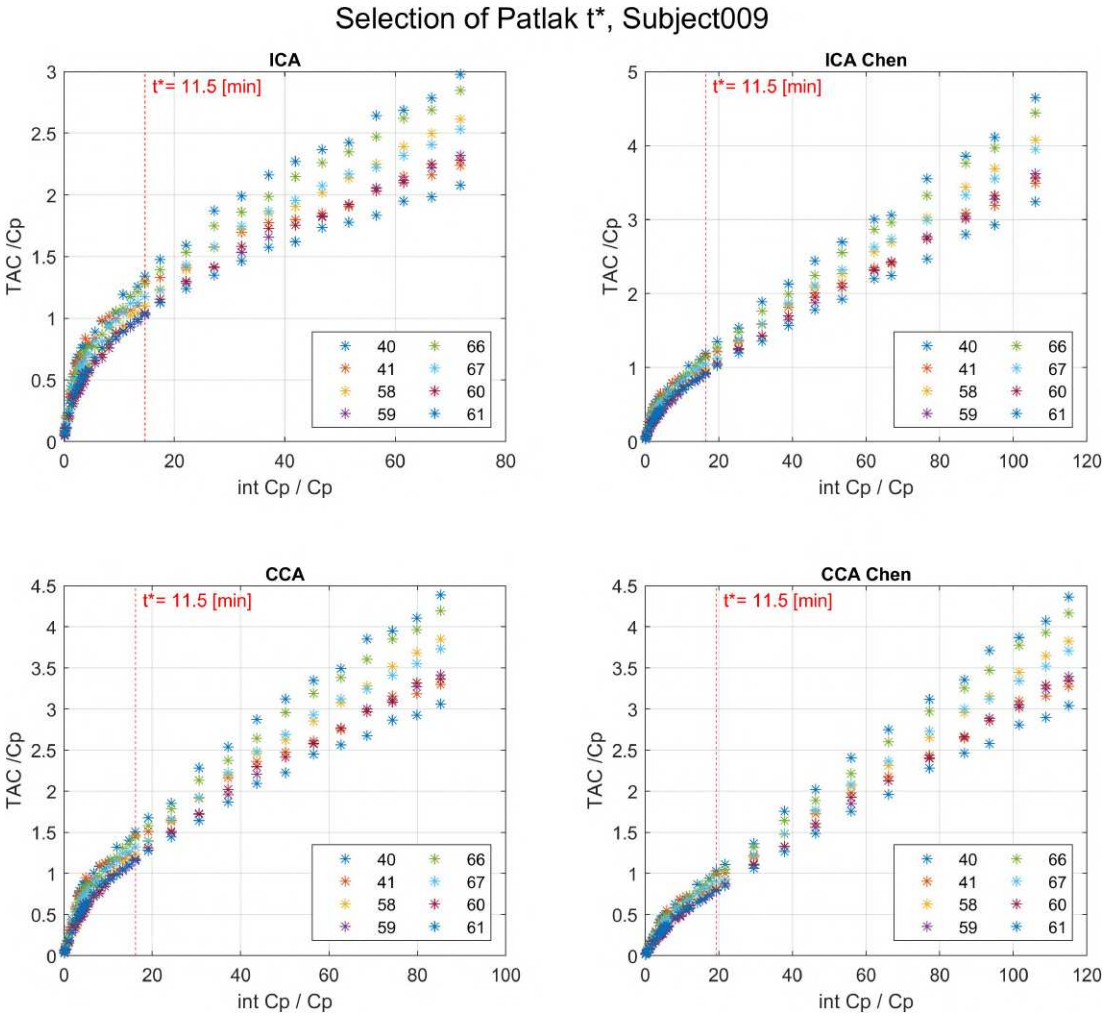

Figure 3.3: Patlak graphical plot for tested regions: each number refers to the region according with Hammers Atlas. Optimal t*, subject 009.

3.1.2 Visual comparison, ROI level and Voxel level

Results of the application of the Patlak graphical method at the ROI and Voxel levels are presented for subjects *n° 2, 5, 9*. Each parametric map of the estimated fractional uptake K_i is accompanied by a map showing the coefficient of variation (CV) in percentage. For this inspection, input IDIF from ICA corrected with Chen's method, and from CCA with no PVE correction were shown.

K_i Patlak map, subject 002

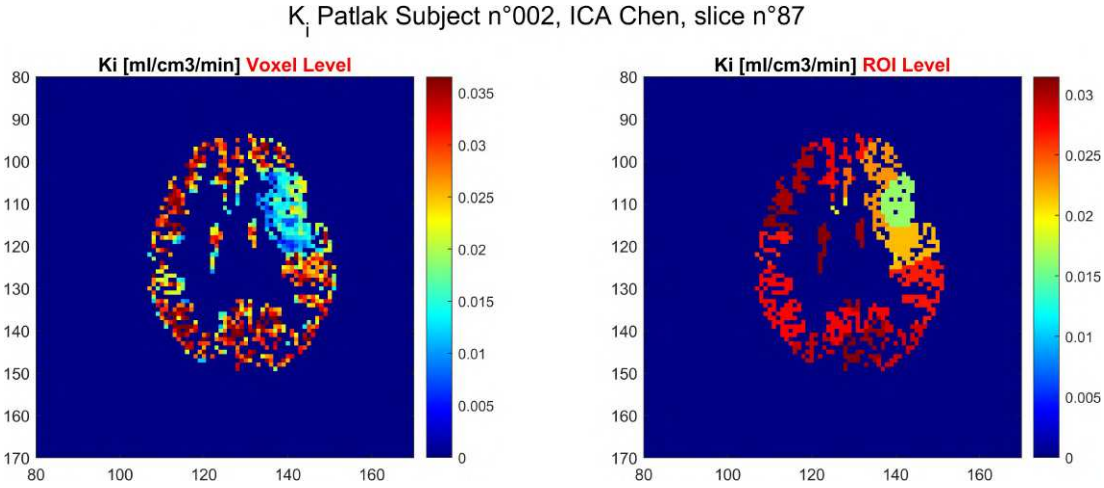

Figure 3.4: K_i parametric map from Patlak graphical method, Voxel level and ROI level, ICA corrected with Chen, Subject 002.

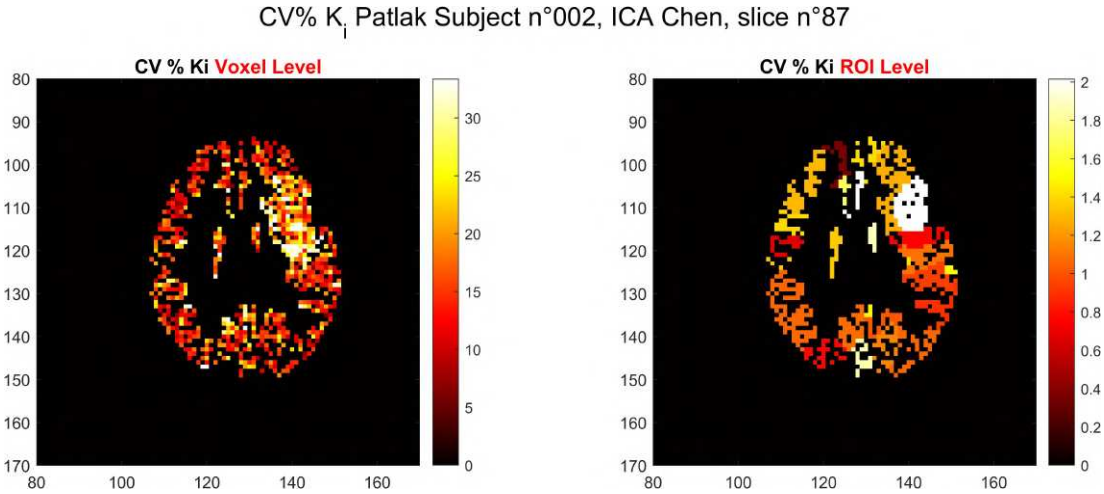

Figure 3.5: CV % of K_i from Patlak graphical method, Voxel level and ROI level, ICA corrected with Chen, Subject 002.

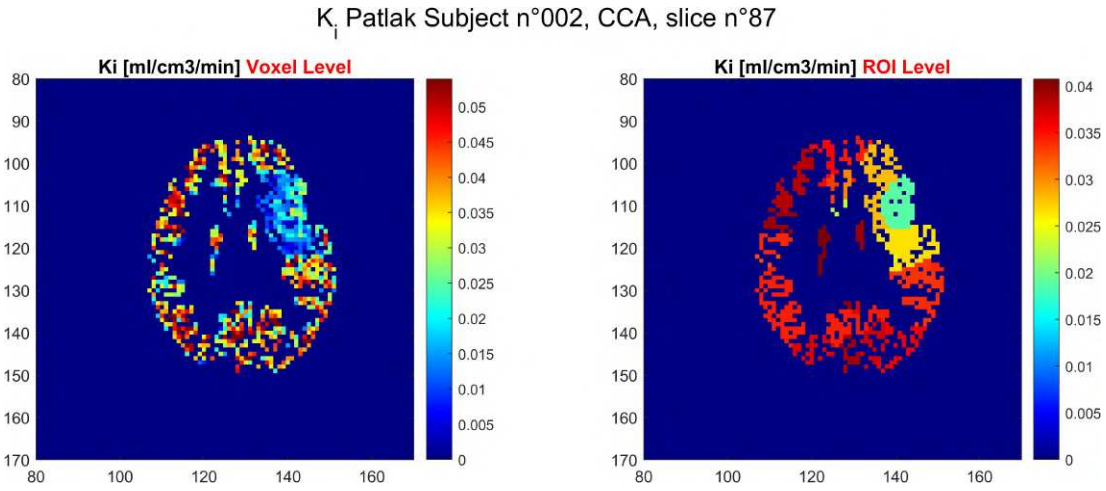

Figure 3.6: K_i parametric map from Patlak graphical method, Voxel level and ROI level, ICA corrected with Chen, Subject 002.

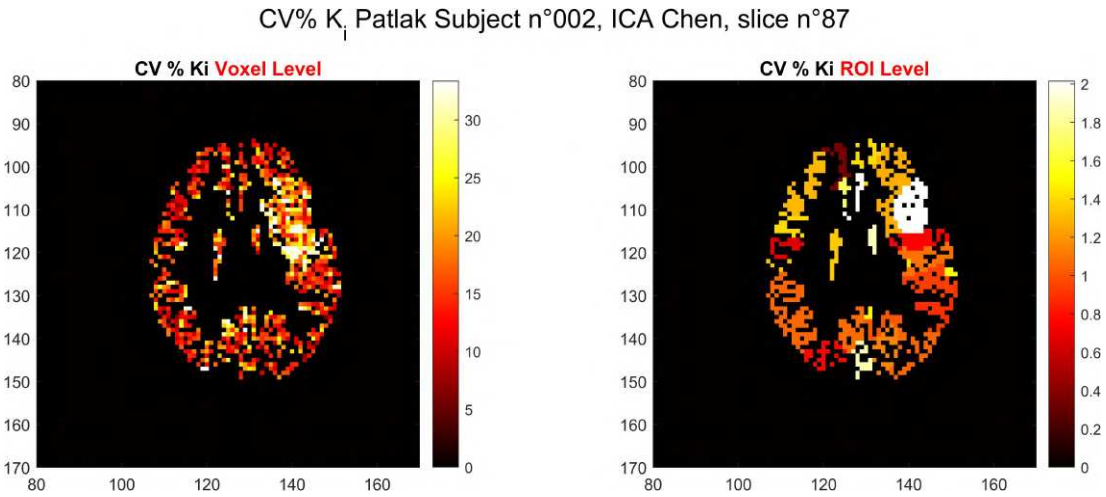

Figure 3.7: CV % of K_i from Patlak graphical method, Voxel level and ROI level, CCA with no correction, Subject 002.

K_i Patlak map, subject 005

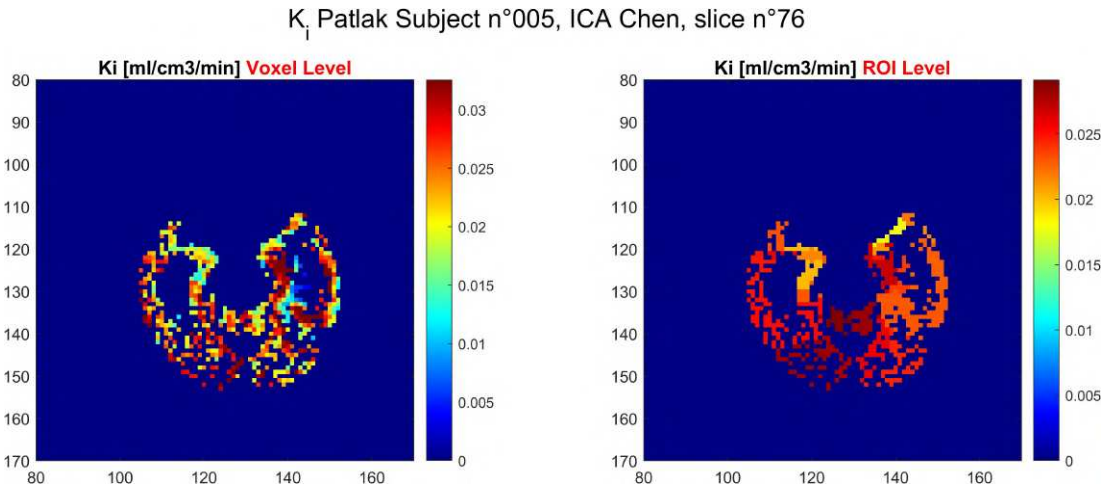

Figure 3.8: K_i parametric map from Patlak graphical method, Voxel level and ROI level, ICA corrected with Chen, Subject 005.

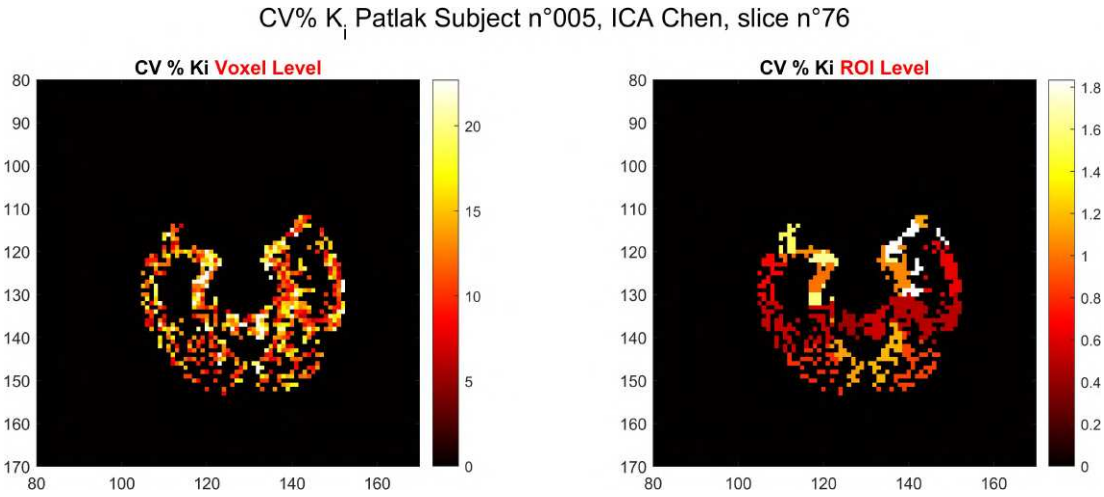

Figure 3.9: CV % of K_i from Patlak graphical method, Voxel level and ROI level, ICA corrected with Chen, Subject 005.

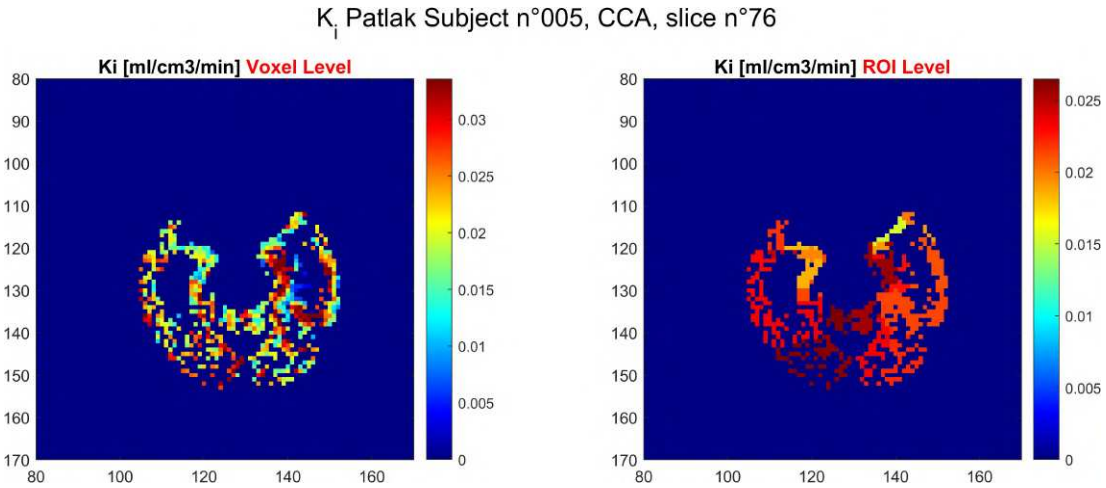

Figure 3.10: K_i parametric map from Patlak graphical method, Voxel level and ROI level, CCA with no correction, Subject 005.

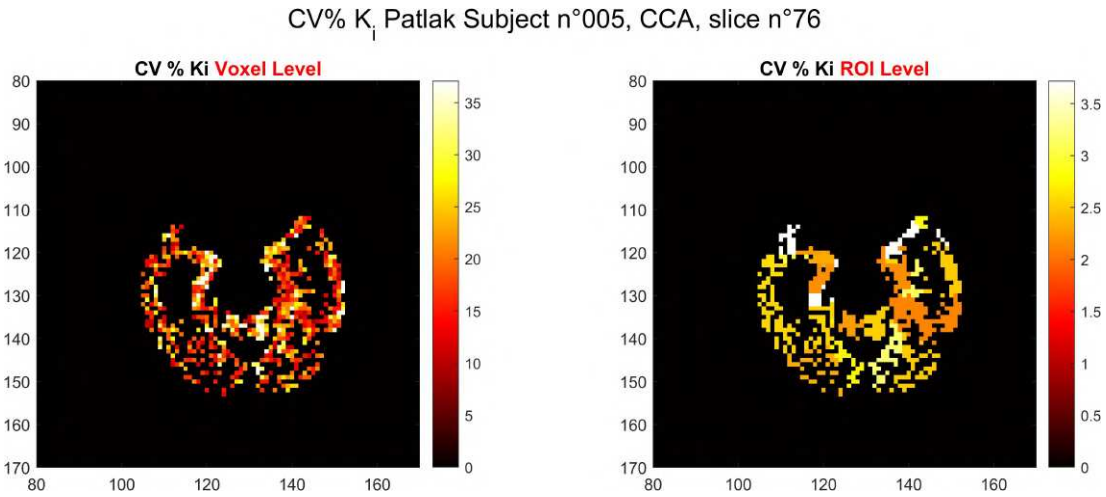

Figure 3.11: CV % of K_i from Patlak graphical method, Voxel level and ROI level, CCA with no correction, Subject 005.

K_i Patlak map, subject 009

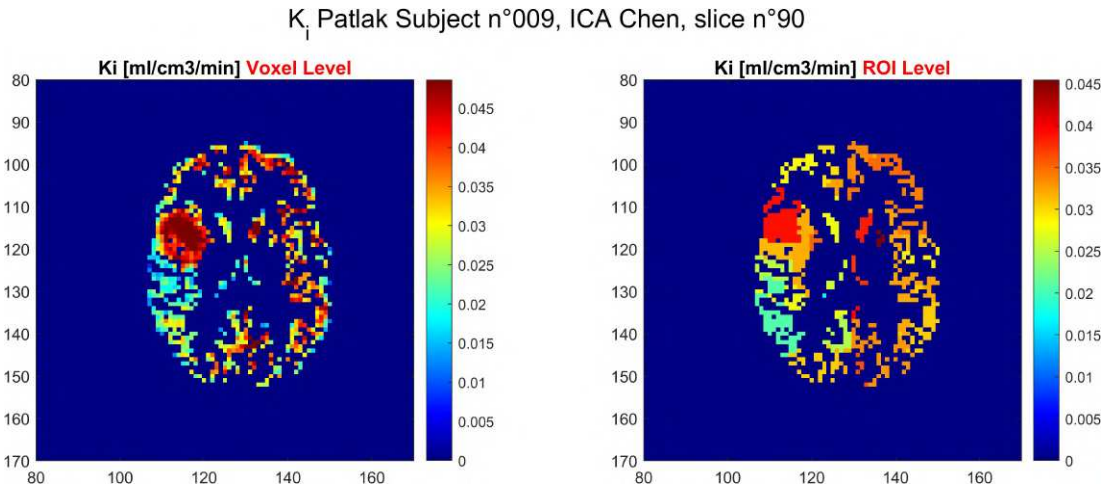

Figure 3.12: K_i parametric map from Patlak graphical method, Voxel level and ROI level, ICA corrected with Chen, Subject 009.

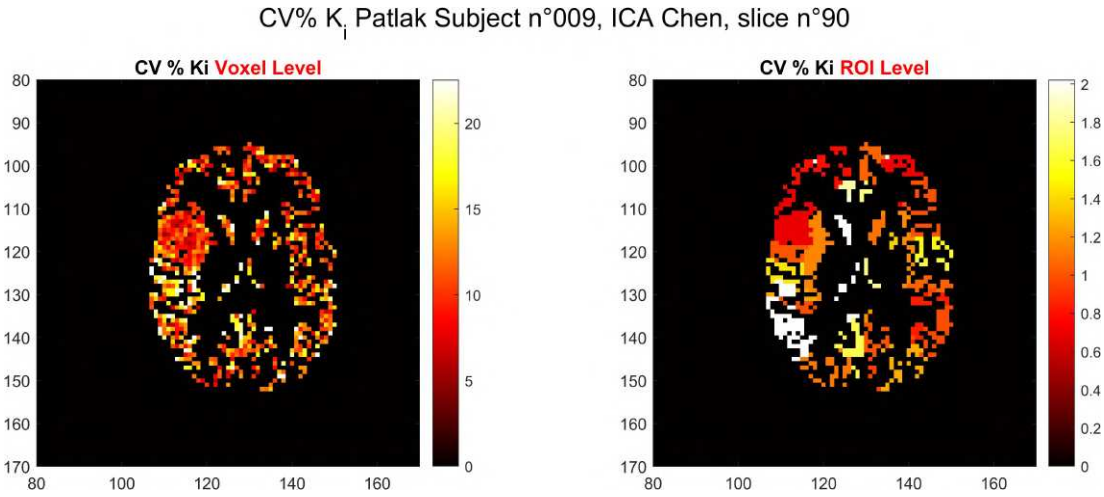

Figure 3.13: CV % of K_i from Patlak graphical method, Voxel level and ROI level, ICA corrected with Chen, Subject 009.

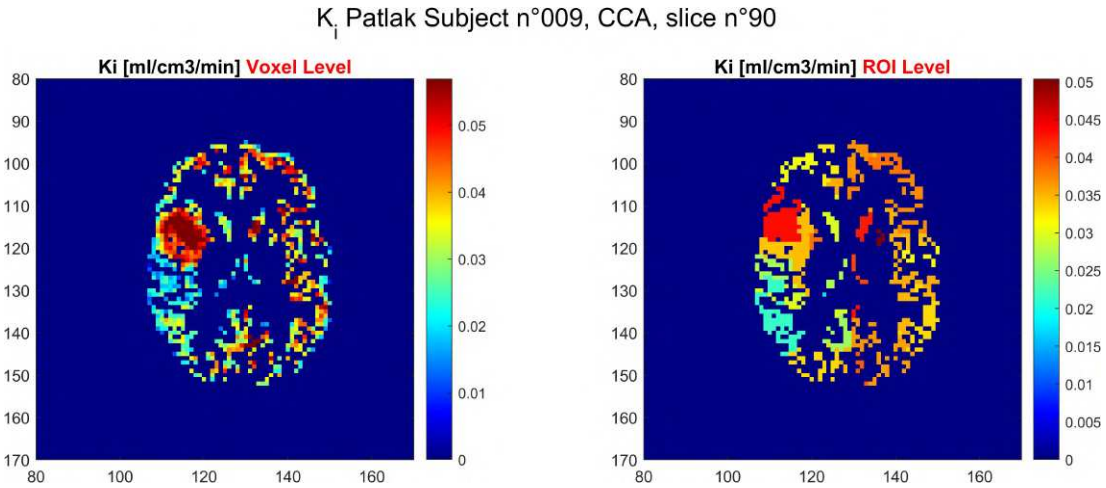

Figure 3.14: K_i parametric map from Patlak graphical method, Voxel level and ROI level, CCA with no correction, Subject 009.

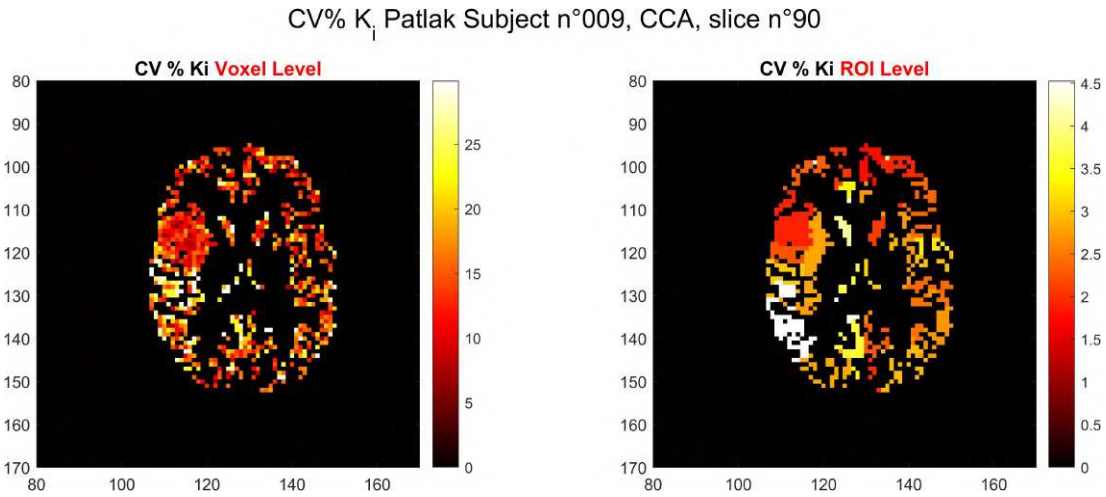

Figure 3.15: CV % of K_i from Patlak graphical method, Voxel level and ROI level, CCA with no correction, Subject 009.

3.1.3 Summary table of K_i with Pathlak at ROI level

The estimated K_i at ROI level for each subject, varying with the input function, are summarized in the following tables. The results show no significant variation in parameter estimates among the different IDIFs.

Table 3.2: Estimated value of fractional uptake K_i at ROI level, for ICA and ICA corrected with Chen's method, represented in mean value ± standard deviation, and CV %

Subject	**ICA**			***CV %***	**ICA Chen**			***CV %***
001	0.0269	±	0.0057	4.6%	0.0263	±	0.005	2.95%
002	0.0239	±	0.0058	6.84%	0.0250	±	0.0049	2.51%
003	0,0216	±	0,0041	3.1%	0,0206	±	0,0035	1.96%
004	0,0295	±	0,0068	5.97%	0,0283	±	0,0053	1,68%
005	0,024	±	0,0045	3.42%	0,0255	±	0,0046	2.42%
006	0,0246	±	0.0059	6.32%	0,0276	±	0.0055	2.78%
007	0,0202	±	0.0044	4.93%	0,0293	±	0.0054	2.47%
008	0,027	±	0.0066	1,68%	0,0324	±	0.0069	1,68%
009	0,0217	±	0.0048	4.55%	0,0307	±	0.0055	2.19%
010	0,0166	±	0.0032	6.44%	0,0162	±	0.0025	3.61%

Table 3.3: Estimated value of fractional uptake K_i at ROI level, for CCA and CCA corrected with Chen's method, represented in mean value ± standard deviation, and CV %

Subject	**CCA**			***CV %***	**CCA Chen**			***CV %***
001	0.0297	±	0.0058	3.21%	0.0264	±	0.005	2.85%
002	0.0312	±	0.0070	4.9%	0.0234	±	0.0046	2.87%
003	0,0253	±	0,0048	2.9%	0,0209	±	0,0048	2.55%
004	0,0352	±	0,0076	5.13%	0,021	±	0,0038	1.95%
005	0,0238	±	0,0046	4.35%	0,022	±	0,0039	2.55%
006	0,0315	±	0.0068	5.06%	0,0237	±	0.0046	2.83%
007	0,0264	±	0.0054	3.64%	0,0291	±	0.0054	1,68%
008	0,0418	±	0.009	1,68%	0,0328	±	0.007	2.91%
009	0,0333	±	0.0064	2.24%	0,0285	±	0.0049	2.14%
010	0,0153	±	0.0028	6.00%	0,014	±	0.0022	3.94%

3.1.4 Summary table of K_i with Pathlak at Voxel level

The estimated K_i at Voxel level for each subject, varying with the input function, are summarized in the following tables. The results show no significant variation in parameter estimates among the different IDIFs.

Table 3.4: Estimated value of fractional uptake K_i at Voxel level, for ICA and ICA corrected with Chen's method, represented in mean value ± standard deviation, and CV %

Subject	**ICA**	***CV %***	**ICA Chen**	***CV %***
001	0,0276 ± 0,0107	38.1	0,0270 ± 0,0084	36.9
002	0,0245 ± 0,0114	56.0	0,0255 ± 0,0079	17.4
003	0,0214 ± 0,0078	26.7	0,0206 ± 0,0063	17.6
004	0,0302 ± 0,0103	25.5	0,0292 ± 0,0069	10.2
005	0,0252 ± 0,0077	18.9	0,0269 ± 0,0073	13.6
006	0,0255 ± 0,0095	30.7	0,0287 ± 0,0076	13.9
007	0,0206 ± 0,0074	30.8	0,0299 ± 0,0081	14.5
008	0,0279 ± 0,0109	29.5	0,0334 ± 0,0105	14.8
009	0,0212 ± 0,0085	29.6	0,0301 ± 0,0091	13.8
010	0,0171 ± 0,0082	163.9	0,0166 ± 0,0059	23.3

Table 3.5: Estimated value of fractional uptake K_i at Voxel level, for CCA and CCA corrected with Chen's method, represented in mean value ± standard deviation, and CV %

Subject	**CCA**	***CV %***	**CCA Chen**	***CV %***
001	0,0305 ± 0,0271	24.6	0,0085 ± 0,0100	21.3
002	0,0317 ± 0,0238	39.0	0,0075 ± 0,0128	18.5
003	0,0251 ± 0,0208	26.6	0,0064 ± 0,0091	18.6
004	0,0361 ± 0,0218	23.4	0,0048 ± 0,0111	10.9
005	0,0250 ± 0,0233	20.9	0,0061 ± 0,0079	13.0
006	0,0327 ± 0,0246	21.0	0,0062 ± 0,0101	13.0
007	0,0268 ± 0,0297	22.2	0,0081 ± 0,0087	15.4
008	0,0431 ± 0,0338	15.5	0,0107 ± 0,0137	15.0
009	0,0326 ± 0,0280	18.3	0,0079 ± 0,0107	13.0
010	0,0158 ± 0,0144	49.1	0,0051 ± 0,0073	24.2

3.2 ROI Level estimation

The ROI-level estimation conducted using WNLLS has yielded physiologically plausible results with high precision, in line with expectations from the literature. The IDIFs that have shown more plausible results for all parameters are the ICA corrected with Chen's method and the CCA without correction. The estimates obtained with the constraint imposed on k_3 exhibit inconsistency in the estimation of certain parameters, depending on the type of IDIF used. Therefore, the results for subjects *n° 2, 5, 9* are summarized through the following figures.

3.2.1 Boxplot K_i

In this paragraph, boxplot of K_i estimated at ROI level are reported in figures.

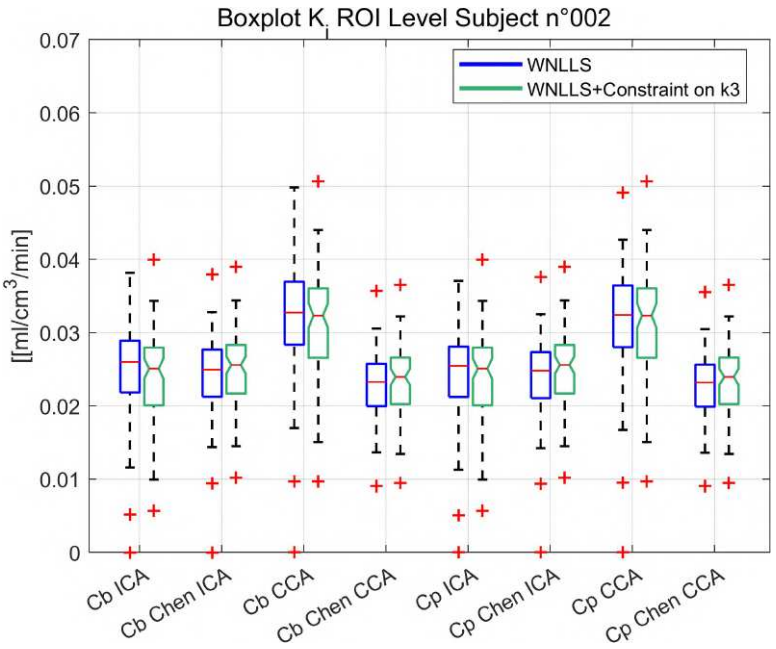

Figure 3.16: Boxplot with K_i values estimated with WNLLS, ROI level, Subject 002

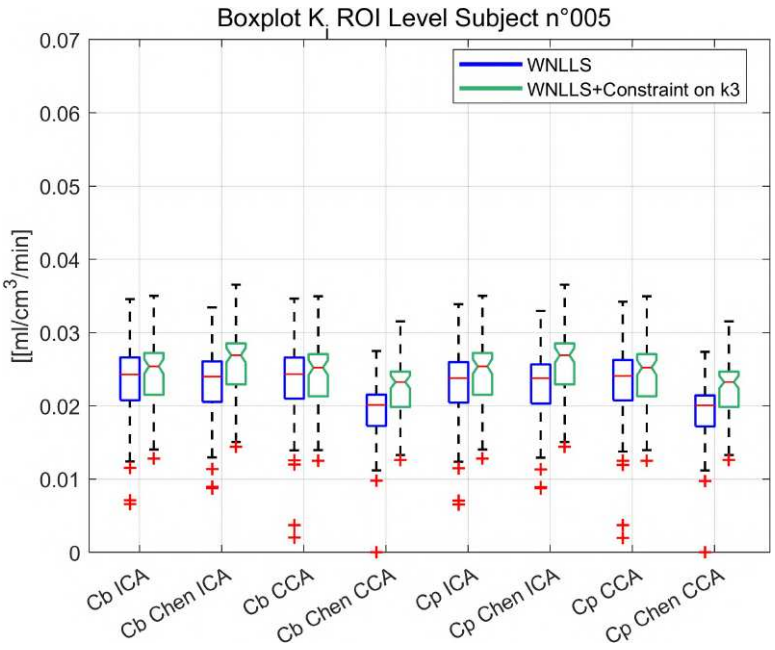

Figure 3.17: Boxplot with K_i values estimated with WNLLS, ROI level, Subject 005

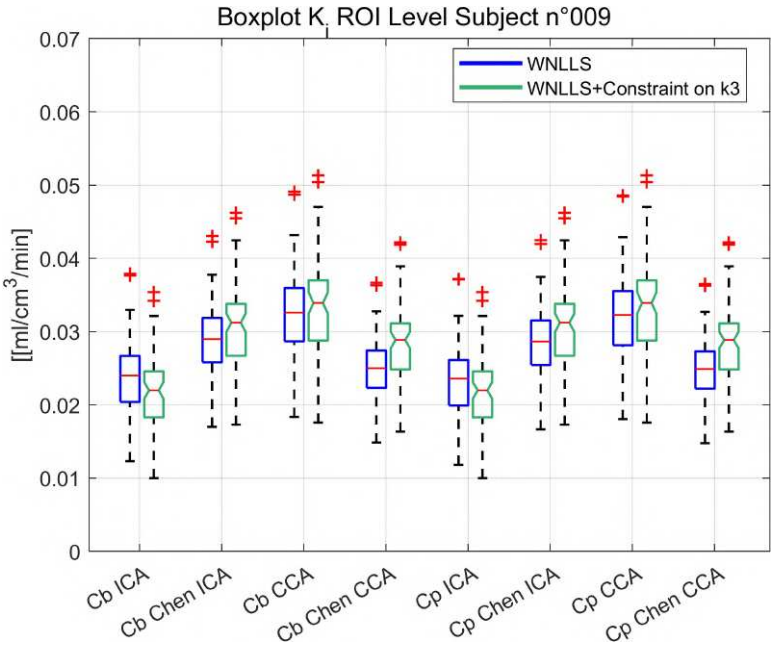

Figure 3.18: Boxplot with K_i values estimated with WNLLS, ROI level, Subject 009

3.2.2 Boxplot K_1

In this paragraph, boxplot of K_1 estimated at ROI level are reported in figures.

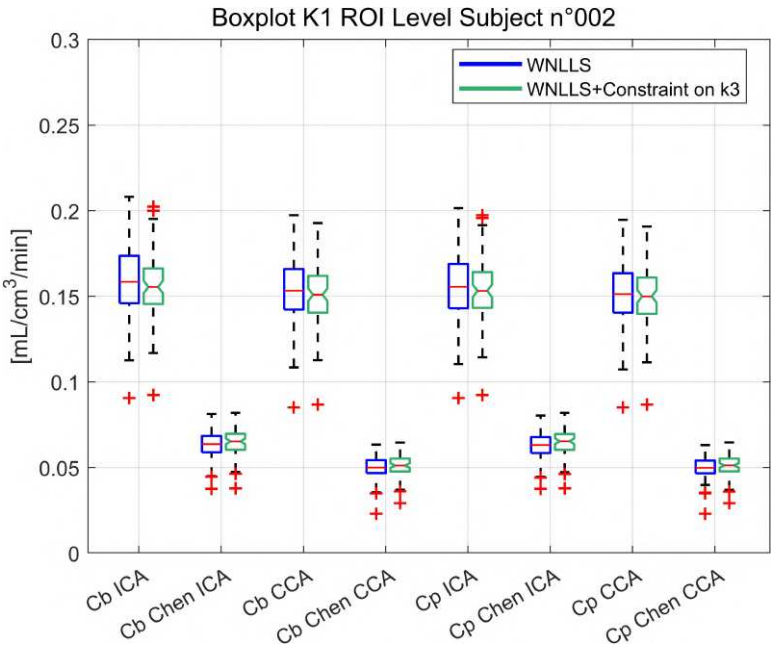

Figure 3.19: Boxplot with K_1 values estimated with WNLLS, ROI level, Subject 002

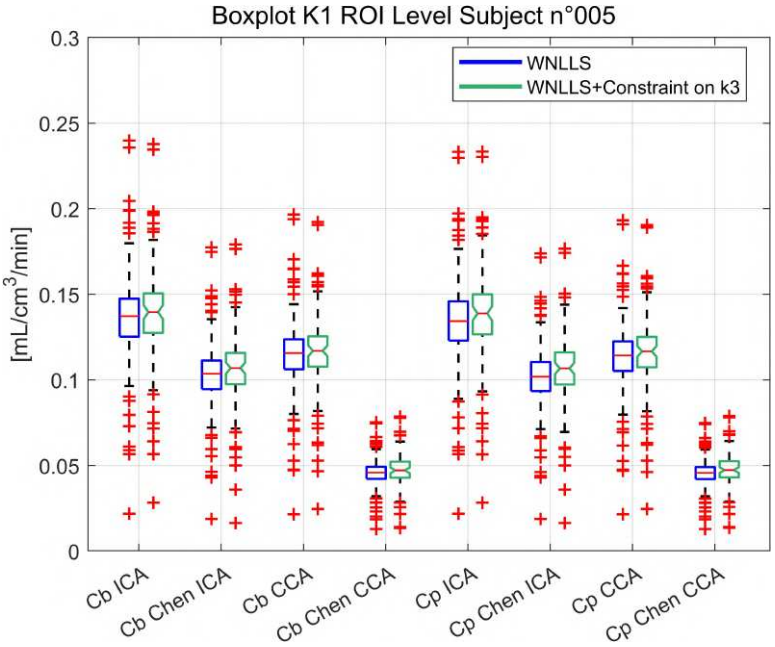

Figure 3.20: Boxplot with K_1 values estimated with WNLLS, ROI level, Subject 005

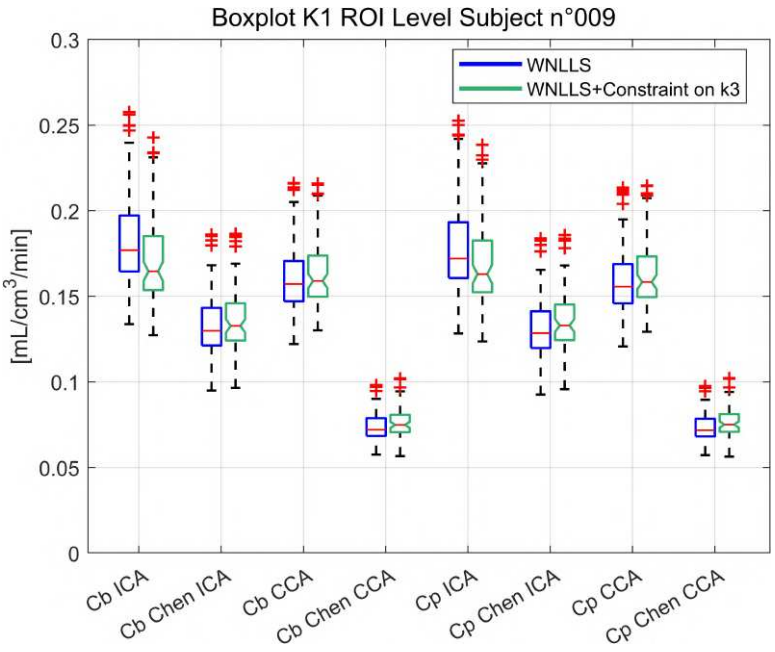

Figure 3.21: Boxplot with K_1 values estimated with WNLLS, ROI level, Subject 009

3.2.3 Boxplot k_2

In this paragraph, boxplot of k_2 estimated at ROI level are reported in figures.

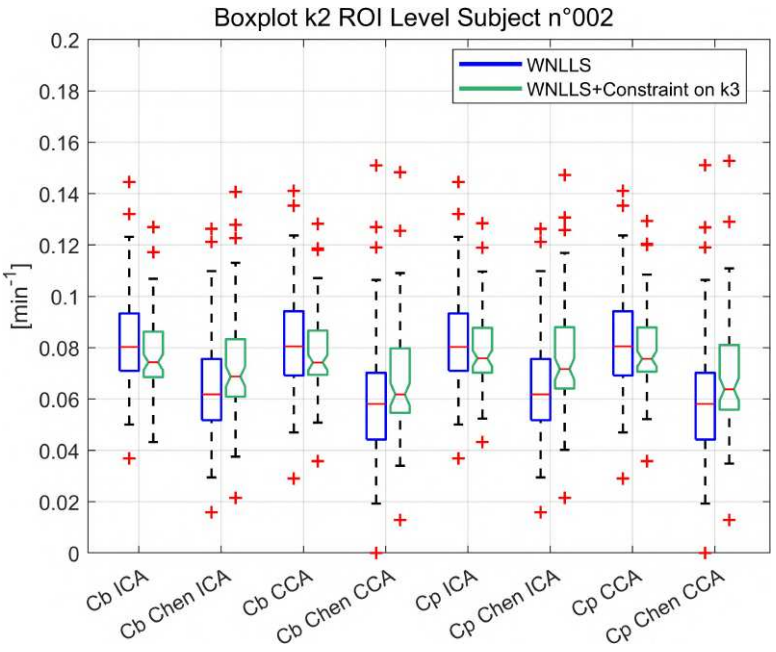

Figure 3.22: Boxplot with k_2 values estimated with WNLLS, ROI level, Subject 002

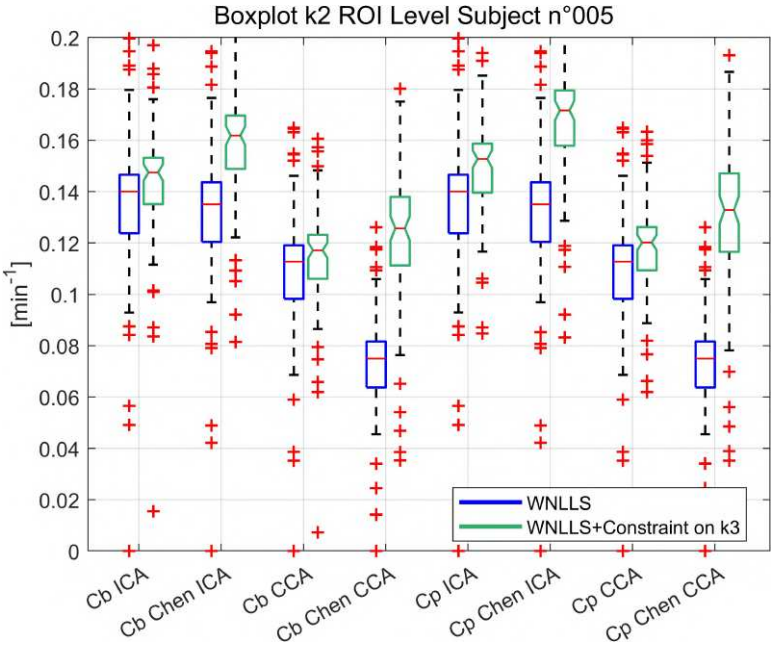

Figure 3.23: Boxplot with k_2 values estimated with WNLLS, ROI level, Subject 005

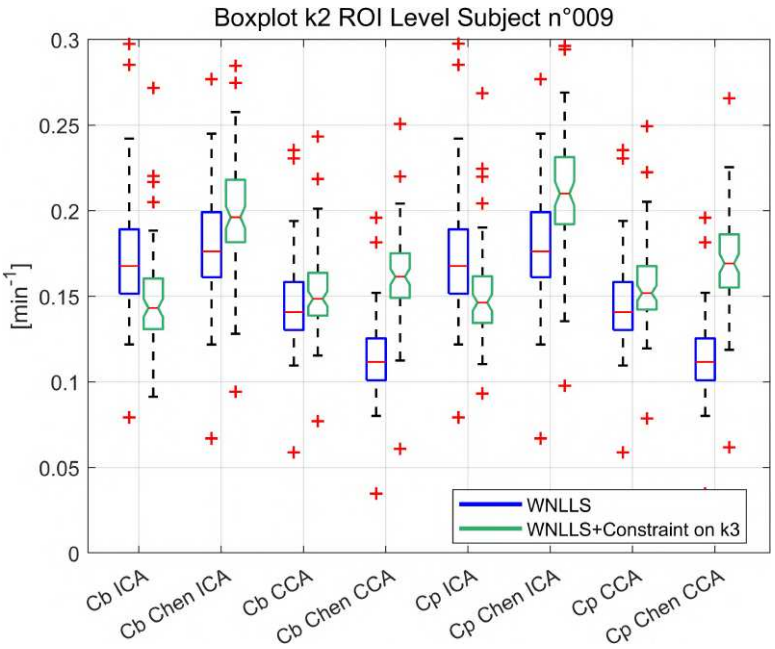

Figure 3.24: Boxplot with k_2 values estimated with WNLLS, ROI level, Subject 009

3.2.4 Boxplot k_3

In this paragraph, boxplot of k_3 estimated at ROI level are reported in figures.

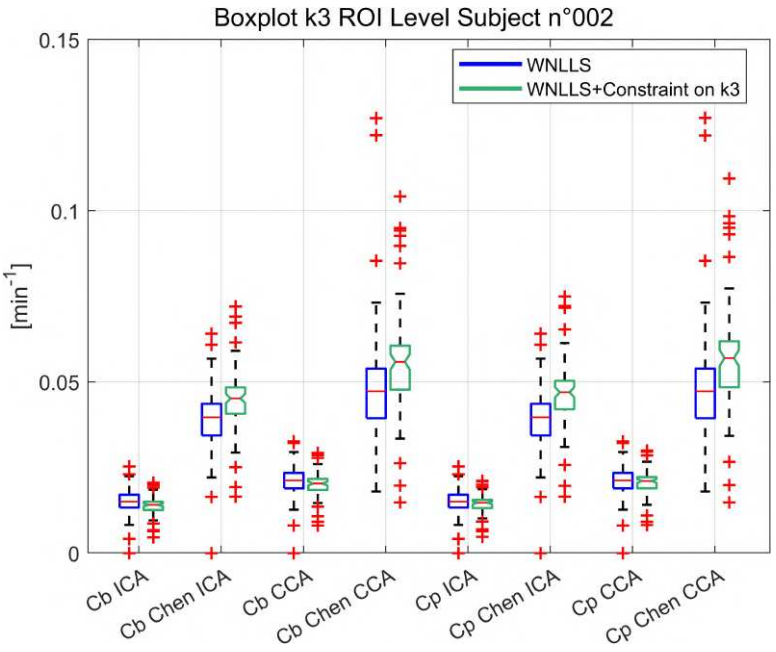

Figure 3.25: Boxplot with k_3 values estimated with WNLLS, ROI level, Subject 002

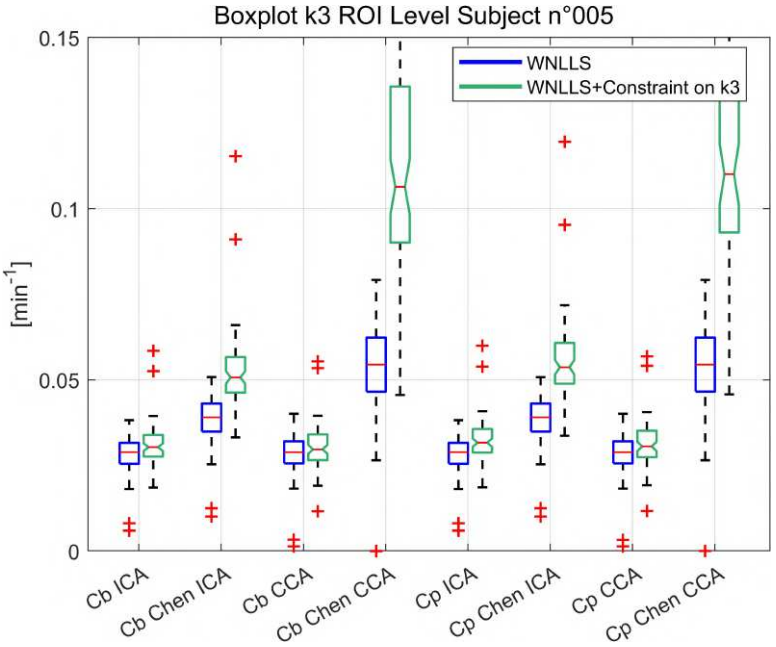

Figure 3.26: Boxplot with k_3 values estimated with WNLLS, ROI level, Subject 005

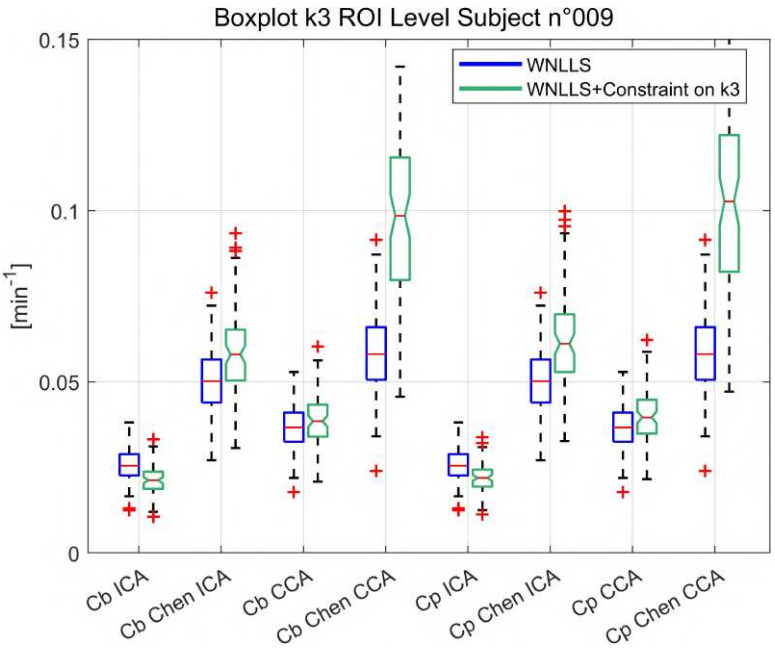

Figure 3.27: Boxplot with k_3 values estimated with WNLLS, ROI level, Subject 009

3.2.5 Boxplot Vb

In this paragraph, boxplot of Vb estimated at ROI level are reported in figures.

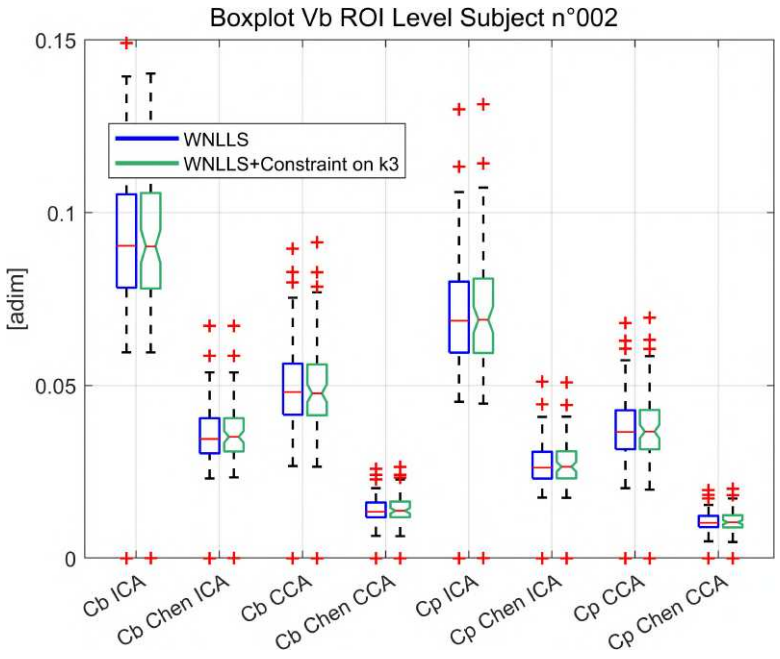

Figure 3.28: Boxplot with Vb values estimated with WNLLS, ROI level, Subject 002

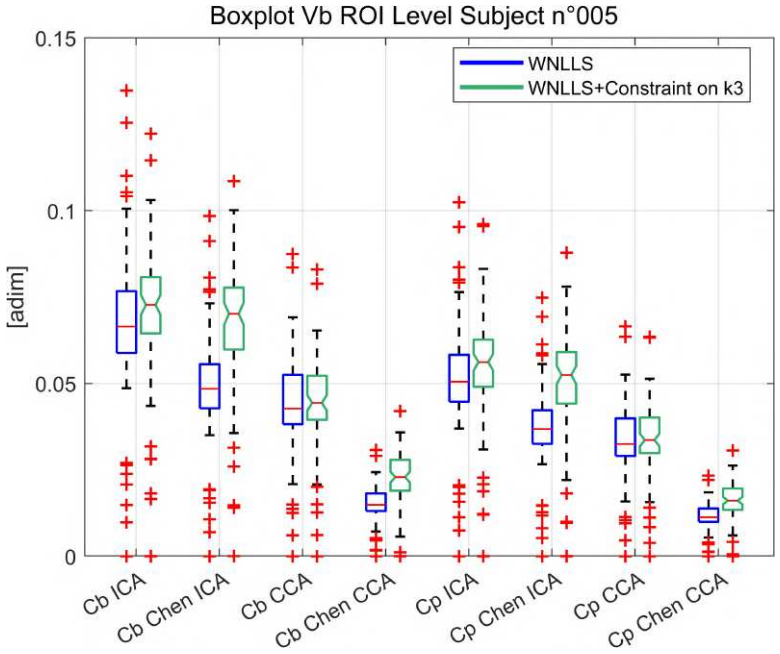

Figure 3.29: Boxplot with Vb values estimated with WNLLS, ROI level, Subject 005

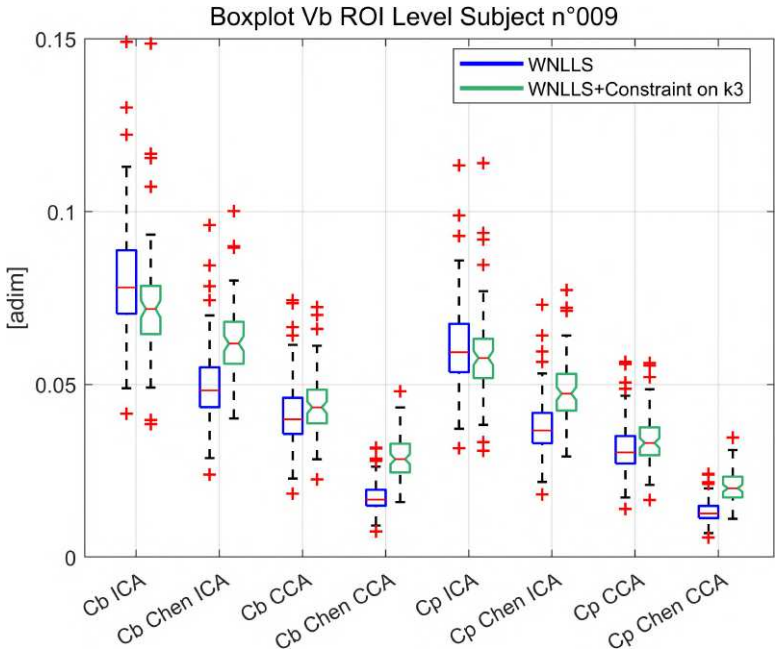

Figure 3.30: Boxplot with Vb values estimated with WNLLS, ROI level, Subject 009

3.3 Voxel Level estimation: exploratory analysis

The MAP estimation at the voxel level has produced results with a high number of outliers for all parameters. It is observed that the imposition of the constraint on k_3 has led to a significantly higher outliers estimate for the parameter in question, compared to the absence of the constraint. Nonetheless, the ICA corrected with Chen's method and the CCA without correction have generated more plausible results, in line with the ROI-level outcomes. The following figures represents the results for subjects *n°9*.

3.3.1 Boxplot K_i

In this paragraph, boxplot of K_i estimated at voxel level are reported in figures.

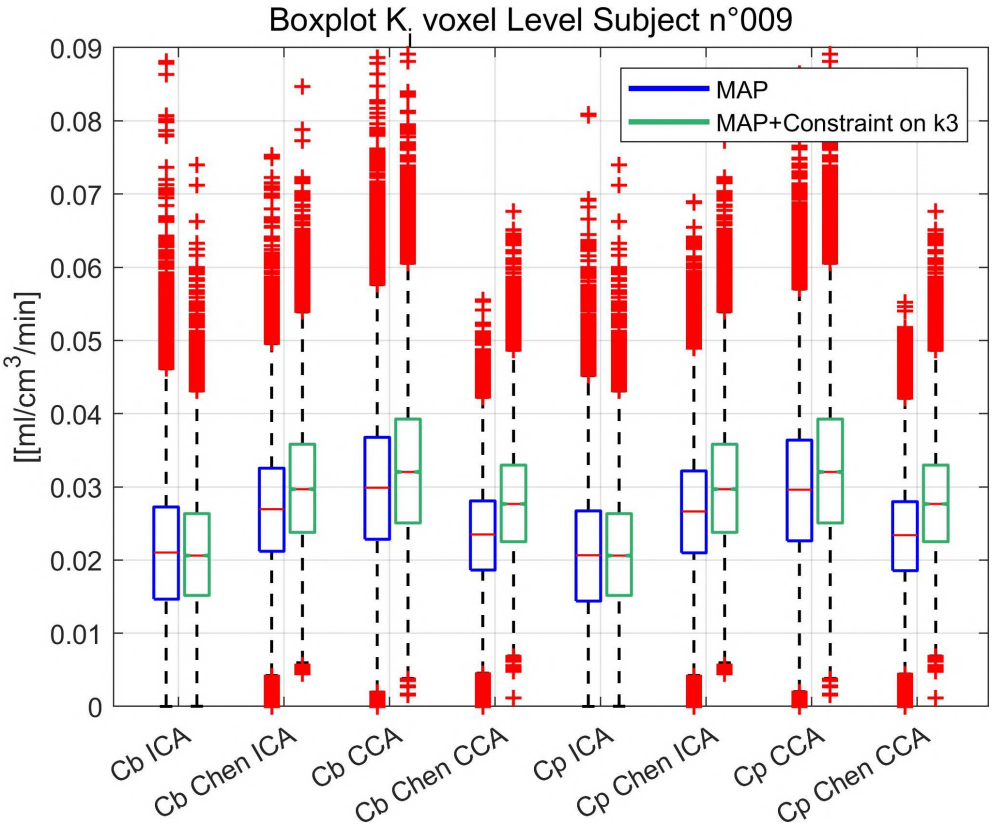

Figure 3.31: Boxplot with K_i values estimated with MAP, Voxel level, Subject 009

3.3.2 Boxplot K_1

In this paragraph, boxplot of K_1 estimated at voxel level are reported in figures.

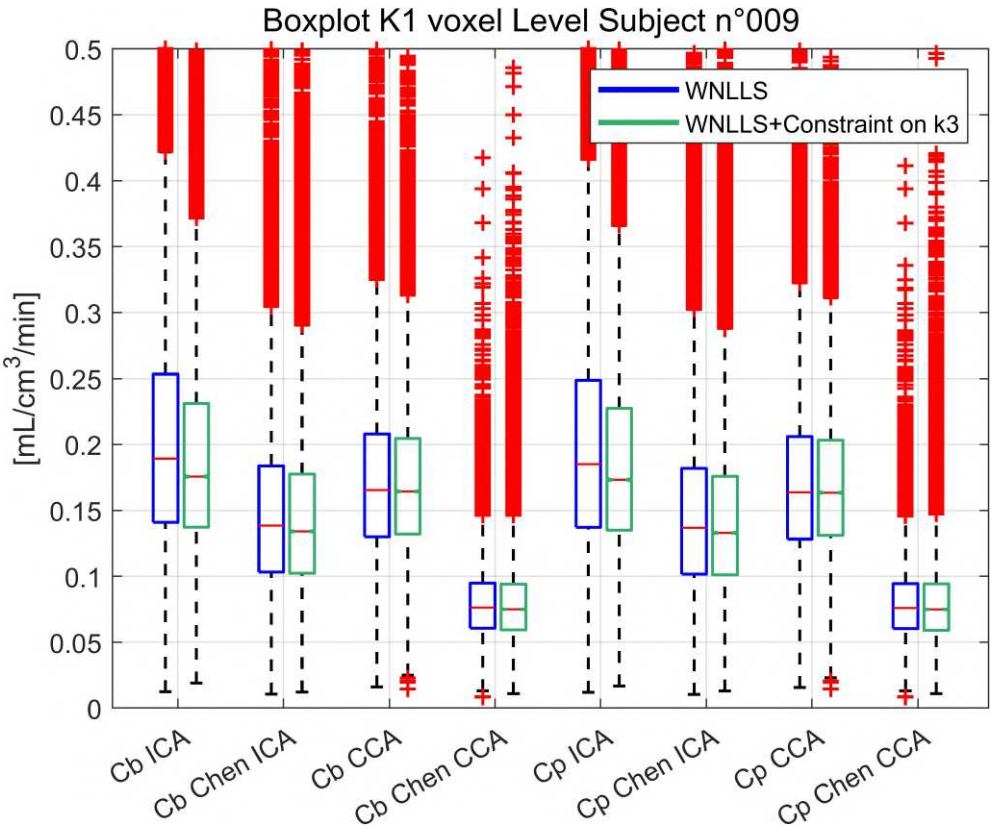

Figure 3.32: Boxplot with K_1 values estimated with MAP, Voxel level, Subject 009

3.3.3 Boxplot k_2

In this paragraph, boxplot of k_2 estimated at voxel level are reported in figures.

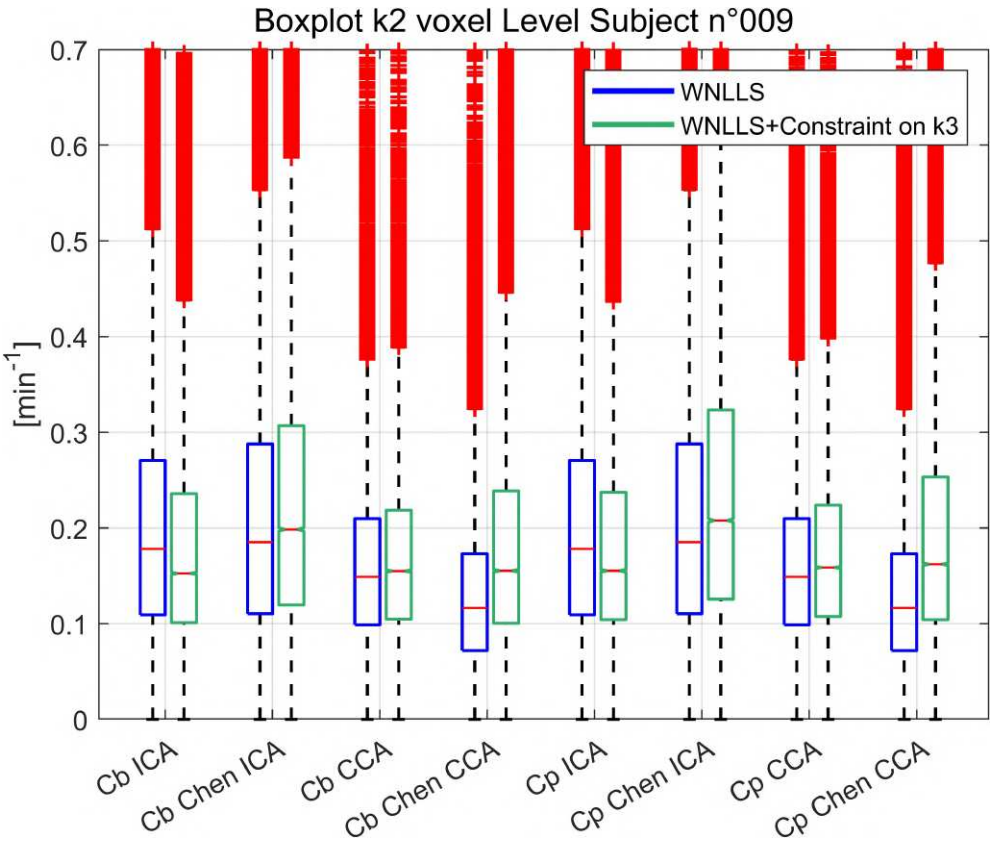

Figure 3.33: Boxplot with k_2 values estimated with MAP, Voxel level, Subject 009

3.3.4 Boxplot k_3

In this paragraph, boxplot of k_3 estimated at voxel level are reported in figures.

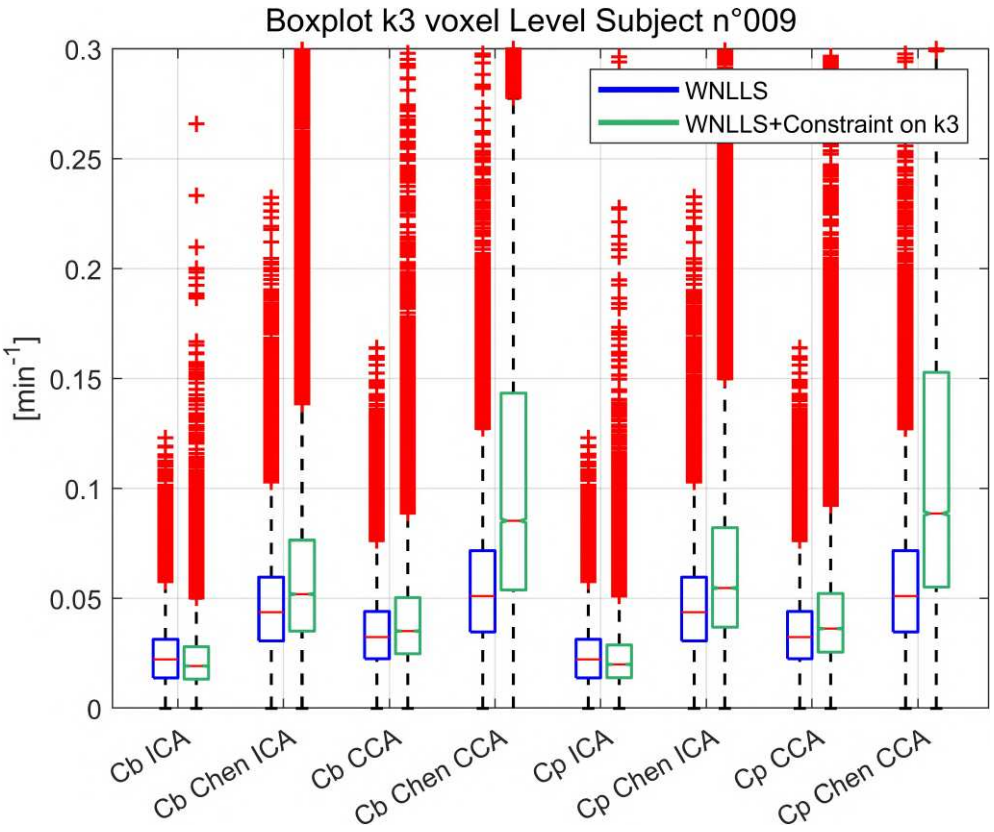

Figure 3.34: Boxplot with k_3 values estimated with MAP, Voxel level, Subject 009

3.3.5 Boxplot Vb

In this paragraph, boxplot of Vb estimated at voxel level are reported in figures.

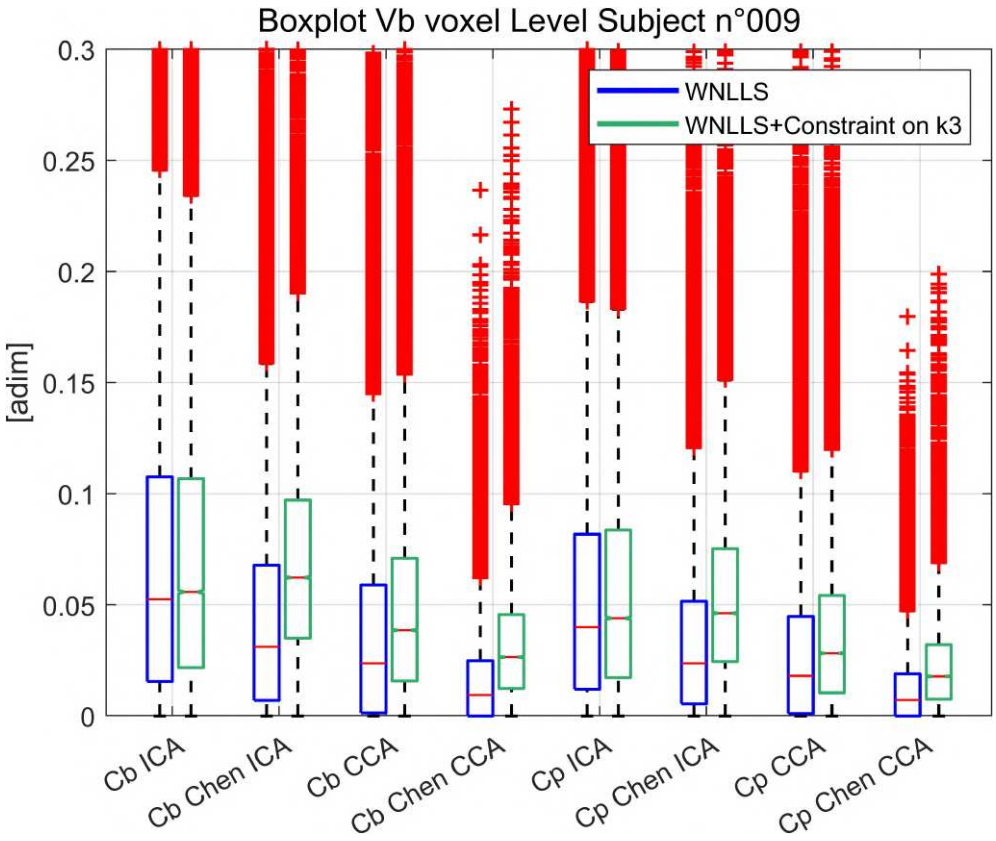

Figure 3.35: Boxplot with Vb values estimated with MAP, Voxel level, Subject 009

3.4 Summary table of estimated parameters at Voxel Level

The estimated parameters are summarized, for each subject, in the following tables. Because of the considerations from the previous results, the parameters obtained for the model with and without the constraint are shown, using only the following IDIFs: ICA corrected with Chen's method and CCA uncorrected for PVE.

We found that the estimated parameter values are consistent with the ranges present in literature, e.g. [42], [43] and [44].

3.4.1 Summary table of K_1 at voxel level

Table 3.6: Estimated value of K_1 at Voxel level, for ICA without correction and with Chen's correction, for both model with and without constraint on k_3. Values are represented in median value ± median absolute deviation. The last raw represent a mean value across all the subject, expressed in mean ± standard deviation

Subject	**ICA Chen**	
	Without constraint	*With constraint*
001	0,097 ± 0,029	0,099 ± 0,023
002	0,068 ± 0,020	0,071 ± 0,017
003	0,098 ± 0,030	0,104 ± 0,028
004	0,087 ± 0,031	0,088 ± 0,030
005	0,120 ± 0,045	0,132 ± 0,045
006	0,085 ± 0,029	0,094 ± 0,029
007	0,157 ± 0,072	0,175 ± 0,068
008	0,110 ± 0,034	0,115 ± 0,030
009	0,138 ± 0,052	0,148 ± 0,050
010	0,064 ± 0,022	0,070 ± 0,022
Overall	0.102 ± 0.028	0.110 ± 0.027

Table 3.7: Estimated value of K_1 at Voxel level, for CCA without correction and with Chen's correction, for both model with and without constraint on k_3. Values are represented in median value ± median absolute deviation. The last raw represent a mean value across all the subject, expressed in mean ± standard deiation

Subject	**CCA Chen**	
	Without constraint	*With constraint*
001	0,130 ± 0,034	0,130 ± 0,029
002	0,163 ± 0,047	0,161 ± 0,037
003	0,207 ± 0,055	0,212 ± 0,053
004	0,162 ± 0,042	0,154 ± 0,033
005	0,133 ± 0,045	0,132 ± 0,041
006	0,164 ± 0,062	0,157 ± 0,052
007	0,178 ± 0,056	0,180 ± 0,052
008	0,161 ± 0,039	0,164 ± 0,036
009	0,165 ± 0,049	0,164 ± 0,046
010	0,101 ± 0,035	0,100 ± 0,030
Overall	0.156 ± 0.028	0.156 ± 0.029

3.4.2 Summary table of k_2 at voxel level

Table 3.8: Estimated value of k_2 at Voxel level, for ICA without correction and with Chen's correction, for both model with and without constraint on k_3. Values are represented in median value ± median absolute deviation. The last raw represent a mean value across all the subject, expressed in mean ± standard deviation

Subject	**ICA Chen**	
	Without constraint	*With constraint*
001	0,089 ± 0,061	0,084 ± 0,047
002	0,068 ± 0,060	0,073 ± 0,052
003	0,127 ± 0,064	0,132 ± 0,060
004	0,190 ± 0,142	0,197 ± 0,162
005	0,149 ± 0,077	0,169 ± 0,088
006	0,101 ± 0,078	0,125 ± 0,097
007	0,210 ± 0,160	0,224 ± 0,165
008	0,096 ± 0,068	0,099 ± 0,059
009	0,185 ± 0,118	0,198 ± 0,126
010	0,105 ± 0,067	0,131 ± 0,087
Overall	0.132 ± 0.047	0.143 ± 0.050

Table 3.9: Estimated value of k_2 at Voxel level, for CCA without correction and with Chen's correction, for both model with and without constraint on k_3. Values are represented in median value ± median absolute deviation. The last raw represent a mean value across all the subject, expressed in mean ± standard deviation

Subject	**CCA Chen**	
	Without constraint	*With constraint*
001	0,087 ± 0,048	0,089 ± 0,039
002	0,084 ± 0,055	0,080 ± 0,039
003	0,148 ± 0,049	0,160 ± 0,050
004	0,102 ± 0,059	0,085 ± 0,042
005	0,125 ± 0,058	0,127 ± 0,053
006	0,133 ± 0,094	0,122 ± 0,078
007	0,151 ± 0,072	0,162 ± 0,071
008	0,099 ± 0,043	0,107 ± 0,041
009	0,149 ± 0,072	0,155 ± 0,071
010	0,118 ± 0,068	0,122 ± 0,060
Overall	0.120 ± 0.024	0.121 ± 0.029

3.4.3 Summary table of k_3 at voxel level

Table 3.10: Estimated value of k_3 at Voxel level, for ICA without correction and with Chen's correction, for both model with and without constraint on k_3. Values are represented in median value ± median absolute deviation. The last raw represent a mean value across all the subject, expressed in mean ± standard deviation

Subject	**ICA Chen**	
	Without constraint	*With constraint*
001	0,032 ± 0,019	0,031 ± 0,109
002	0,034 ± 0,025	0,040 ± 2,022
003	0,030 ± 0,013	0,032 ± 0,054
004	0,084 ± 0,037	0,097 ± 5,509
005	0,035 ± 0,014	0,045 ± 1,169
006	0,041 ± 0,023	0,058 ± 3,277
007	0,043 ± 0,016	0,052 ± 1,414
008	0,038 ± 0,021	0,040 ± 0,141
009	0,044 ± 0,019	0,052 ± 1,485
010	0,028 ± 0,016	0,041 ± 5,877
Overall	0.041 ± 0.015	0.049 ± 0.018

Table 3.11: Estimated value of k_3 at Voxel level, for CCA without correction and with Chen's correction, for both model with and without constraint on k_3. Values are represented in median value ± median absolute deviation. The last raw represent a mean value across all the subject, expressed in mean ± standard deviation

Subject	**CCA Chen**	
	Without constraint	*With constraint*
001	0,024 ± 0,014	0,026 ± 0,026
002	0,018 ± 0,013	0,019 ± 0,018
003	0,017 ± 0,007	0,020 ± 0,009
004	0,029 ± 0,015	0,025 ± 0,012
005	0,026 ± 0,012	0,027 ± 0,023
006	0,031 ± 0,016	0,030 ± 0,023
007	0,024 ± 0,010	0,027 ± 0,033
008	0,032 ± 0,014	0,035 ± 0,019
009	0,032 ± 0,014	0,035 ± 0,156
010	0,018 ± 0,012	0,021 ± 0,194
Overall	0.025 ± 0.006	0.027 ± 0.006

3.4.4 Summary table of Vb at voxel level

Table 3.12: Estimated value of Vb at Voxel level, for ICA without correction and with Chen's correction, for both model with and without constraint on k_3. Values are represented in median value ± median absolute deviation. The last raw represent a mean value across all the subject, expressed in mean ± standard deviation

Subject	**ICA Chen**	
	Without constraint	*With constraint*
001	0,022 ± 0,031	0,028 ± 0,031
002	0,022 ± 0,027	0,032 ± 0,029
003	0,021 ± 0,029	0,030 ± 0,030
004	0,021 ± 0,025	0,041 ± 0,027
005	0,039 ± 0,045	0,077 ± 0,043
006	0,015 ± 0,023	0,030 ± 0,026
007	0,021 ± 0,037	0,059 ± 0,041
008	0,018 ± 0,031	0,026 ± 0,031
009	0,031 ± 0,041	0,062 ± 0,040
010	0,009 ± 0,021	0,019 ± 0,024
Overall	0.022 ± 0.008	0.041 ± 0.018

Table 3.13: Estimated value of Vb at Voxel level, for CCA without correction and with Chen's correction, for both model with and without constraint on k_3. Values are represented in median value ± median absolute deviation. The last raw represent a mean value across all the subject, expressed in mean ± standard deviation

Subject	**CCA Chen**	
	Without constraint	*With constraint*
001	0,026 ± 0,038	0,032 ± 0,038
002	0,023 ± 0,045	0,032 ± 0,045
003	0,015 ± 0,040	0,029 ± 0,040
004	0,026 ± 0,039	0,028 ± 0,038
005	0,032 ± 0,041	0,043 ± 0,040
006	0,023 ± 0,041	0,033 ± 0,040
007	0,008 ± 0,028	0,020 ± 0,029
008	0,020 ± 0,037	0,030 ± 0,035
009	0,024 ± 0,038	0,039 ± 0,037
010	0,013 ± 0,031	0,021 ± 0,033
Overall	0.021 ± 0.007	0.031 ± 0.007

3.5 Correlation analysis and comparison with Variational Bayes at Voxel Level

Correlation analysis was performed to assess the coherence between the spatial patterns of the different maps. In here only the results obtained with two of the four input functions examined (ICA with Chen correction and CCA without any correction) are presented.

3.5.1 K_i Correlation

In this paragraph, the correlation plots between K_i estimated values are reported in figures.

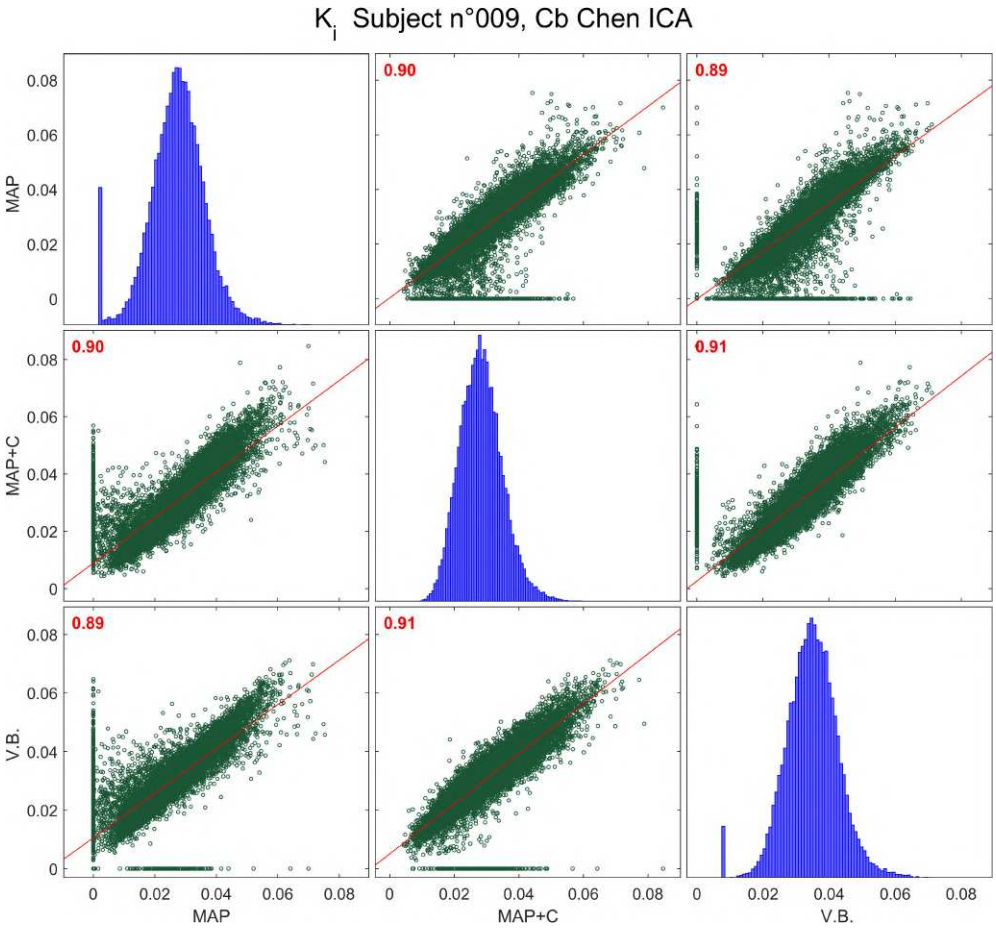

Figure 3.36: Correlation with K_i [ml/cm^3/min] values estimated with MAP and Variational Bayesian, Voxel level, ICA with Chen's correction, Subject 009

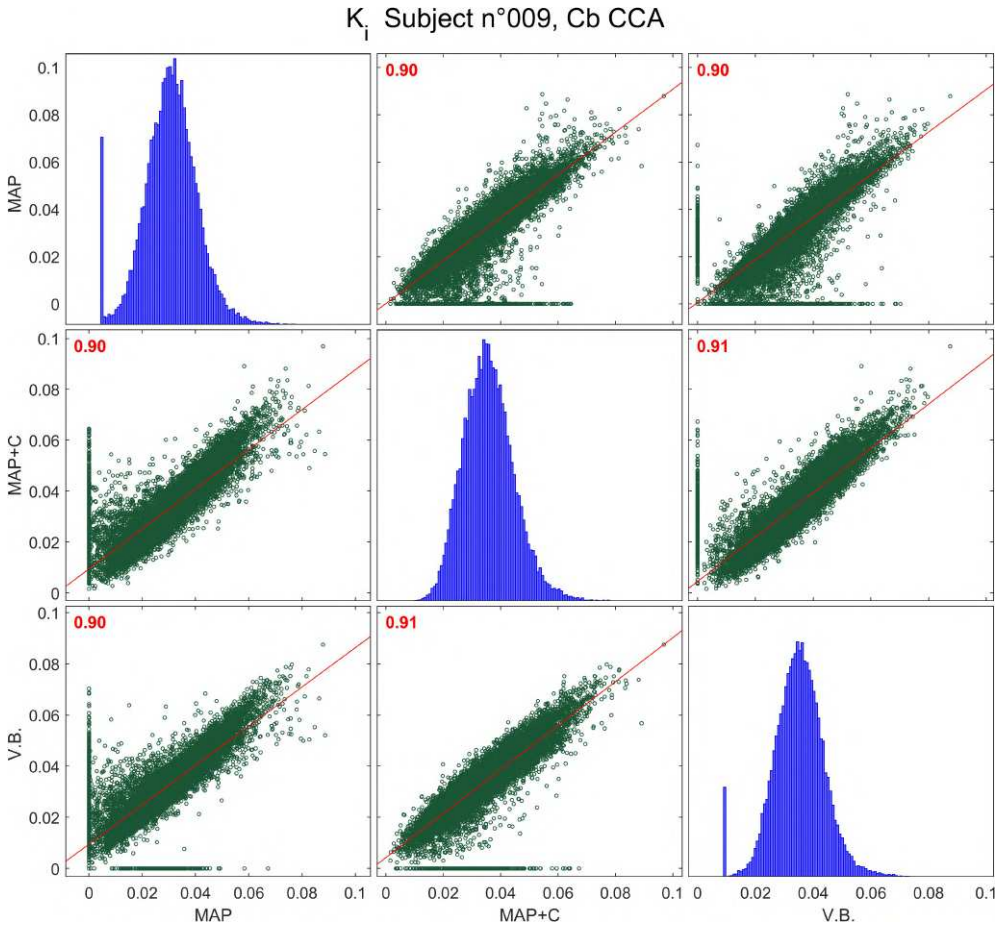

Figure 3.37: Correlation with K_i [ml/cm^3/min] values estimated with MAP and Variational Bayesian, Voxel level, CCA with no correction for PVE, Subject 009

3.5.2 K_1 Correlation

In this paragraph, the correlation plots between K_1 estimated values are reported in figures.

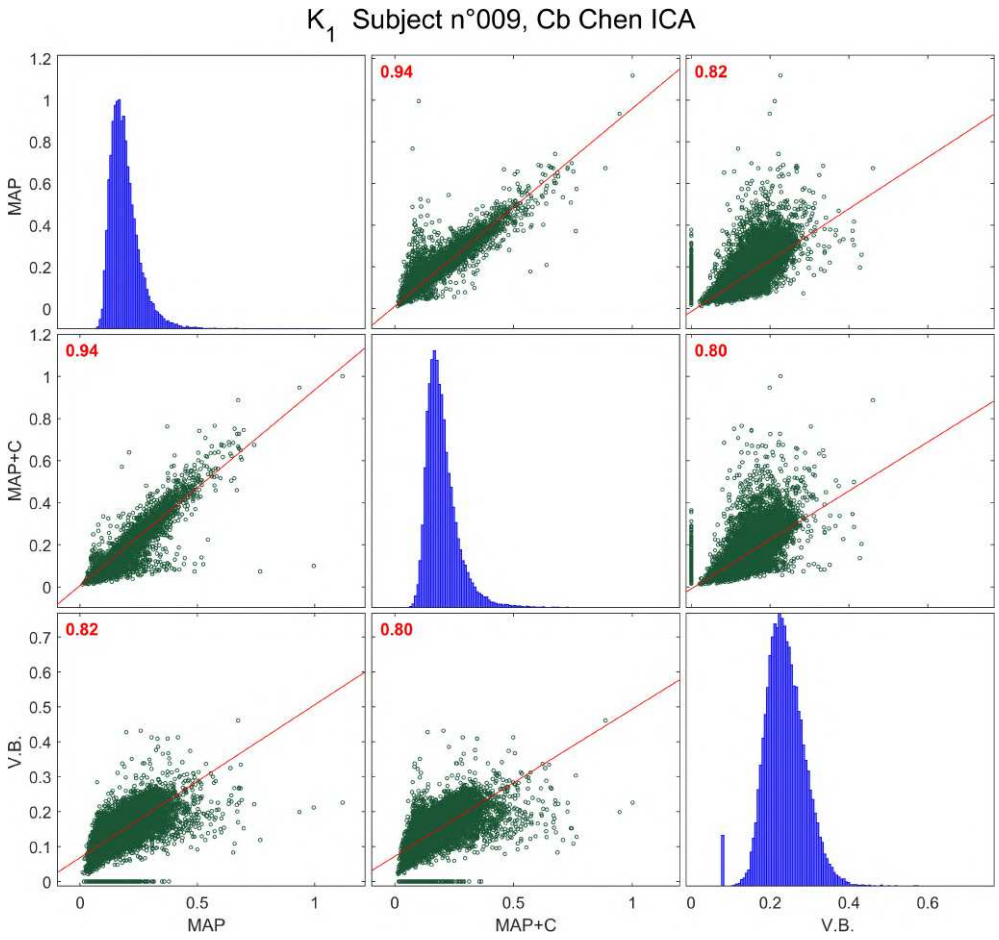

Figure 3.38: Correlation with K_1 [ml/cm^3/min] values estimated with MAP and Variational Bayesian, Voxel level, ICA with Chen's correction, Subject 009

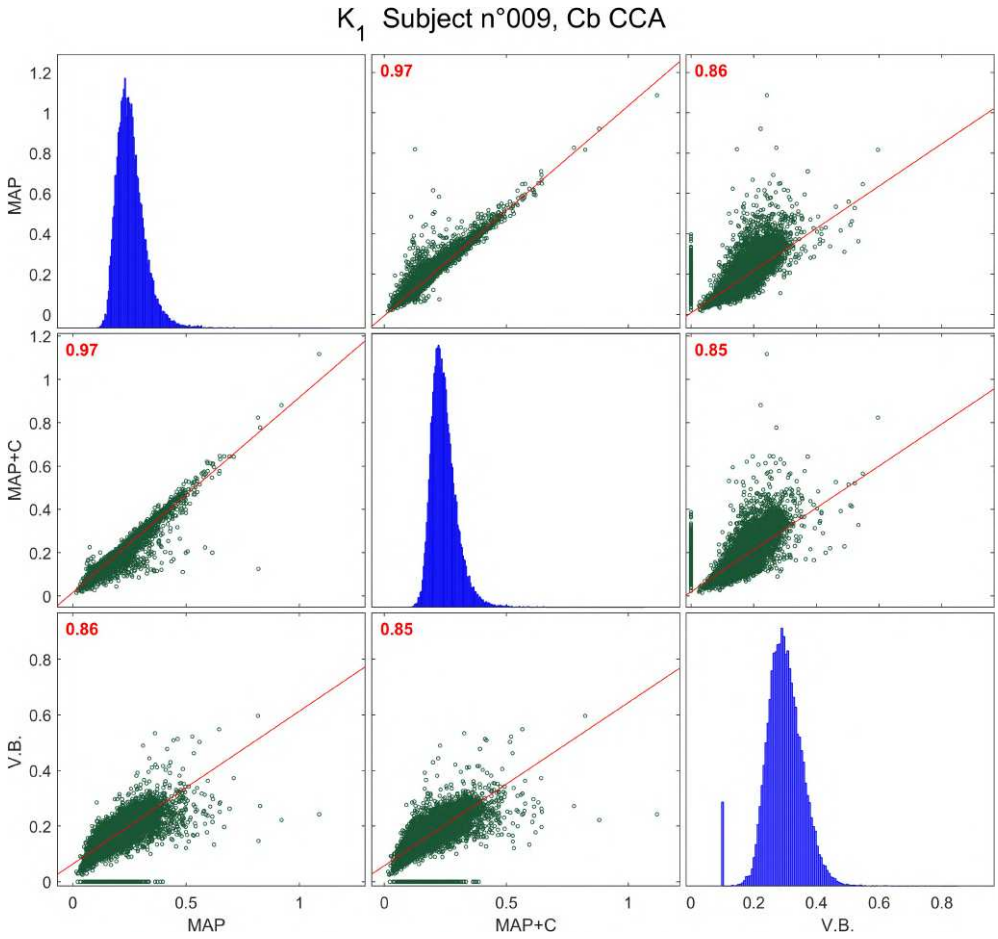

Figure 3.39: Correlation with K_1 [ml/cm^3/min] values estimated with MAP and Variational Bayesian, Voxel level, CCA with no correction for PVE, Subject 009

3.5.3 k_2 Correlation

In this paragraph, the correlation plots between k_2 estimated values are reported in figures.

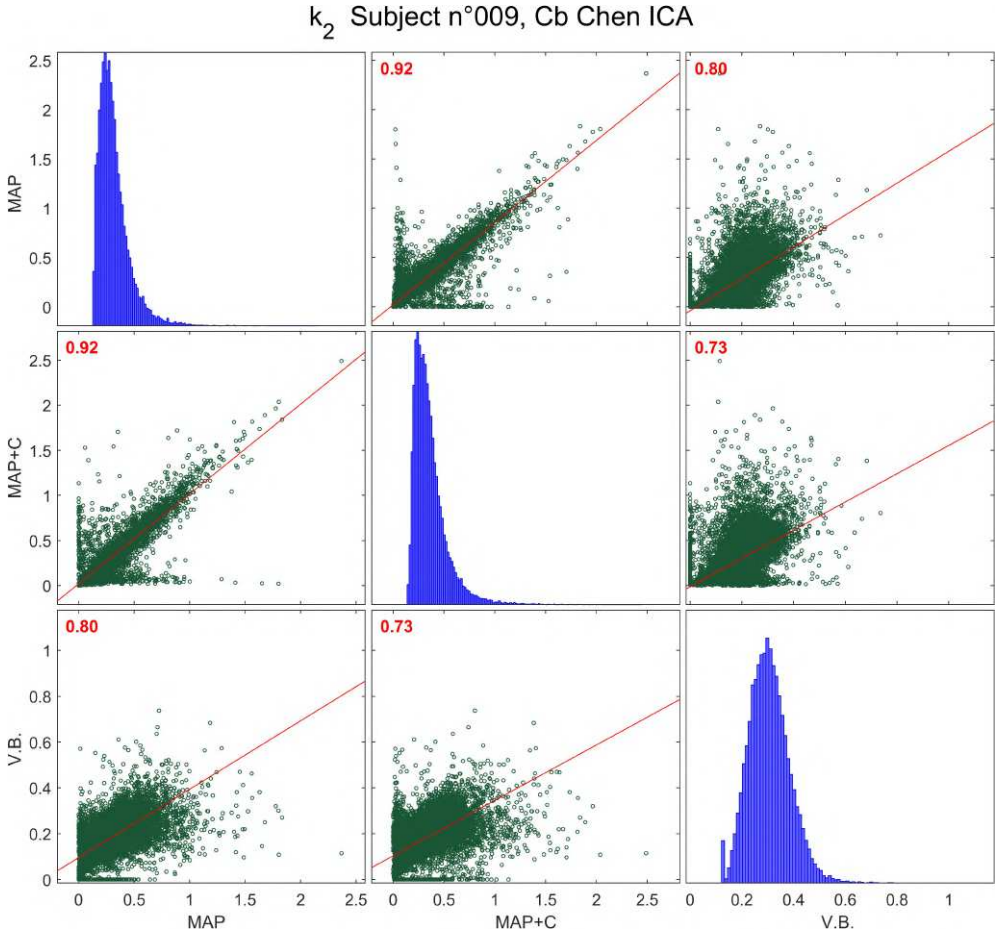

Figure 3.40: Correlation with k_2 [min^{-1}] values estimated with MAP and Variational Bayesian, Voxel level, ICA with Chen's correction, Subject 009

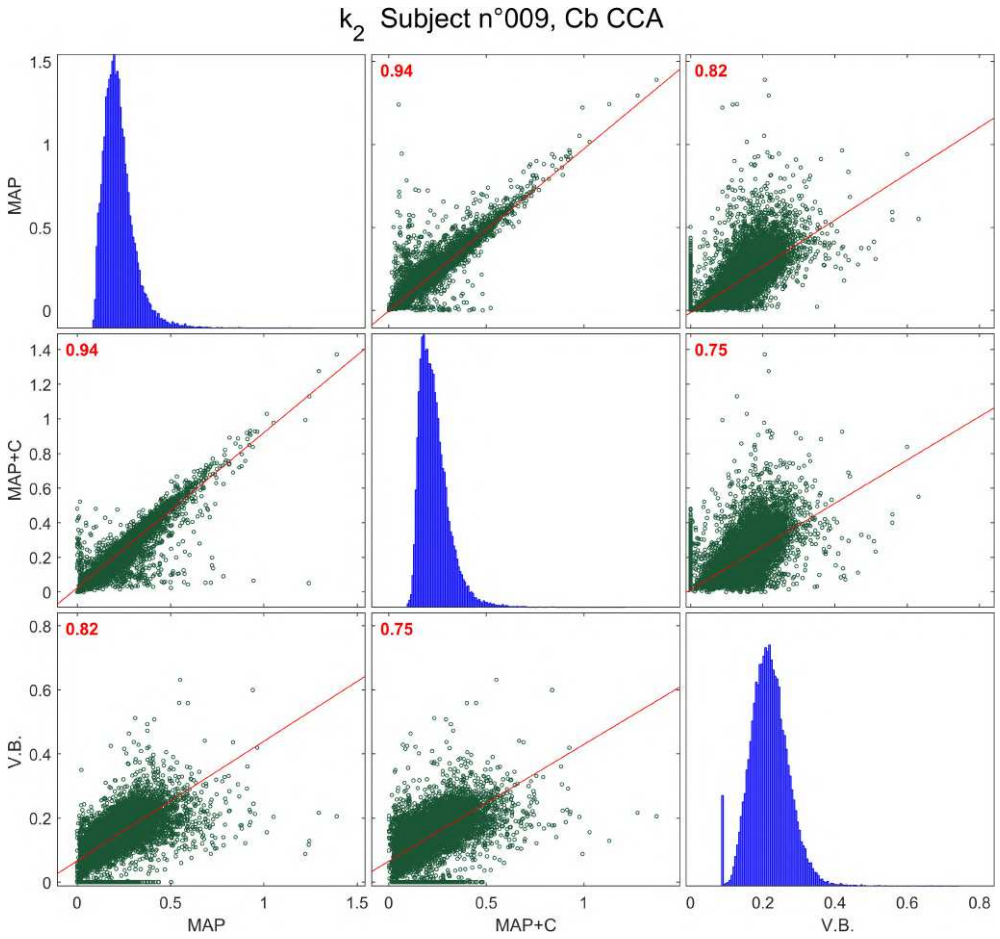

Figure 3.41: Correlation with k_2 [min^{-1}] values estimated with MAP and Variational Bayesian, Voxel level, CCA with no correction for PVE, Subject 009

3.5.4 k_3 Correlation

In this paragraph, the correlation plots between k_3 estimated values are reported in figures.

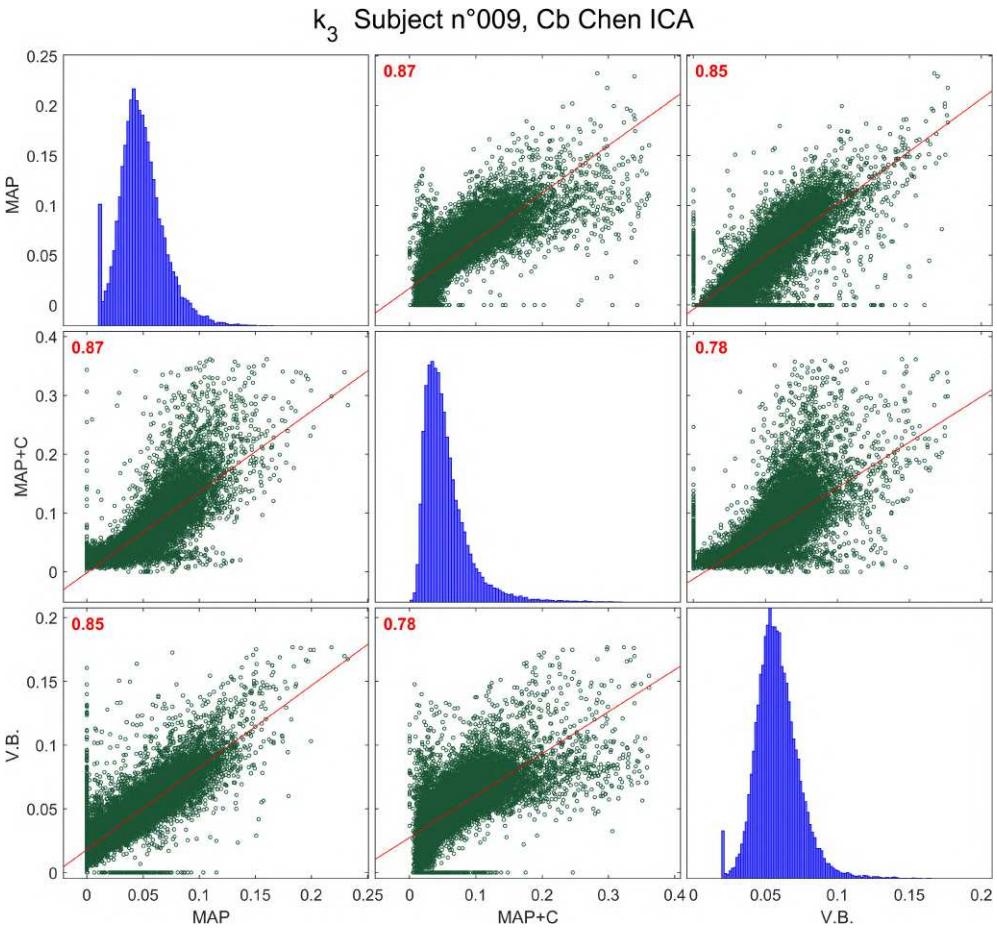

Figure 3.42: Correlation with k_3 [min^{-1}] values estimated with MAP and Variational Bayesian, Voxel level, ICA with Chen's correction, Subject 009

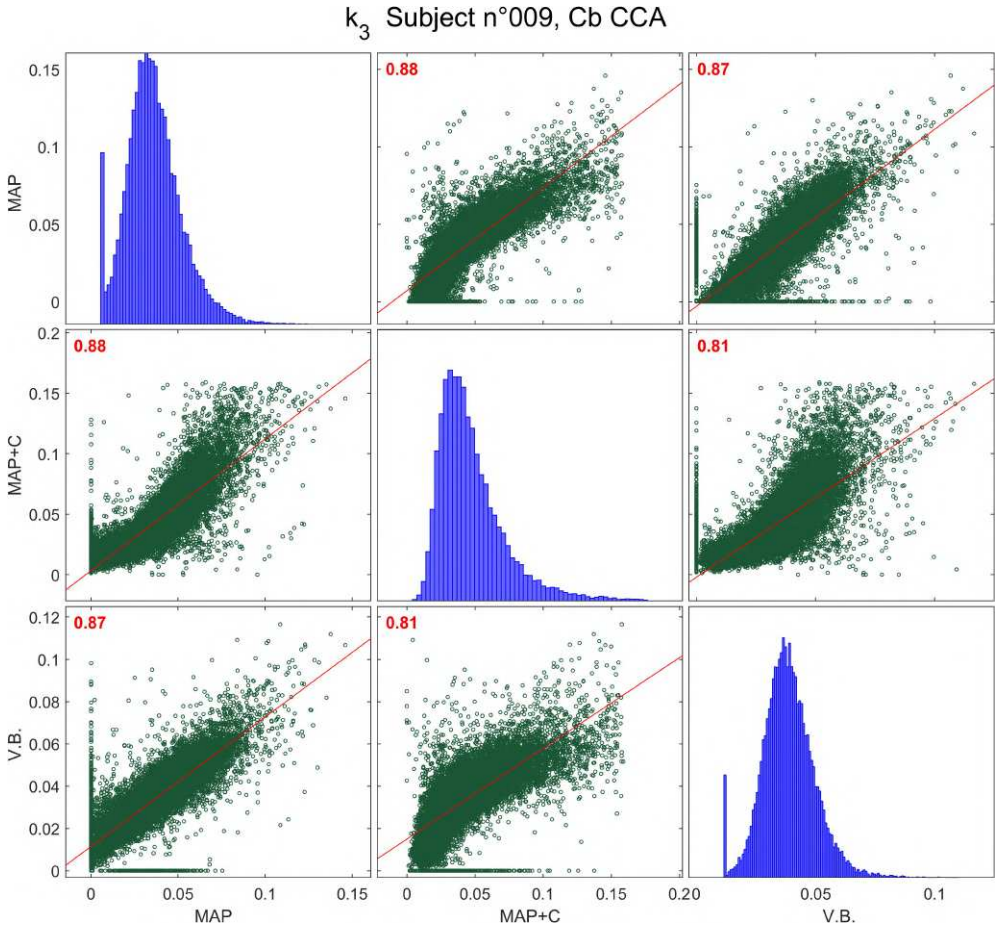

Figure 3.43: Correlation with k_3 [min^{-1}] values estimated with MAP and Variational Bayesian, Voxel level, CCA with no correction for PVE, Subject 009

3.5.5 Vb Correlation

In this paragraph, the correlation plots between Vb estimated values are reported in figures.

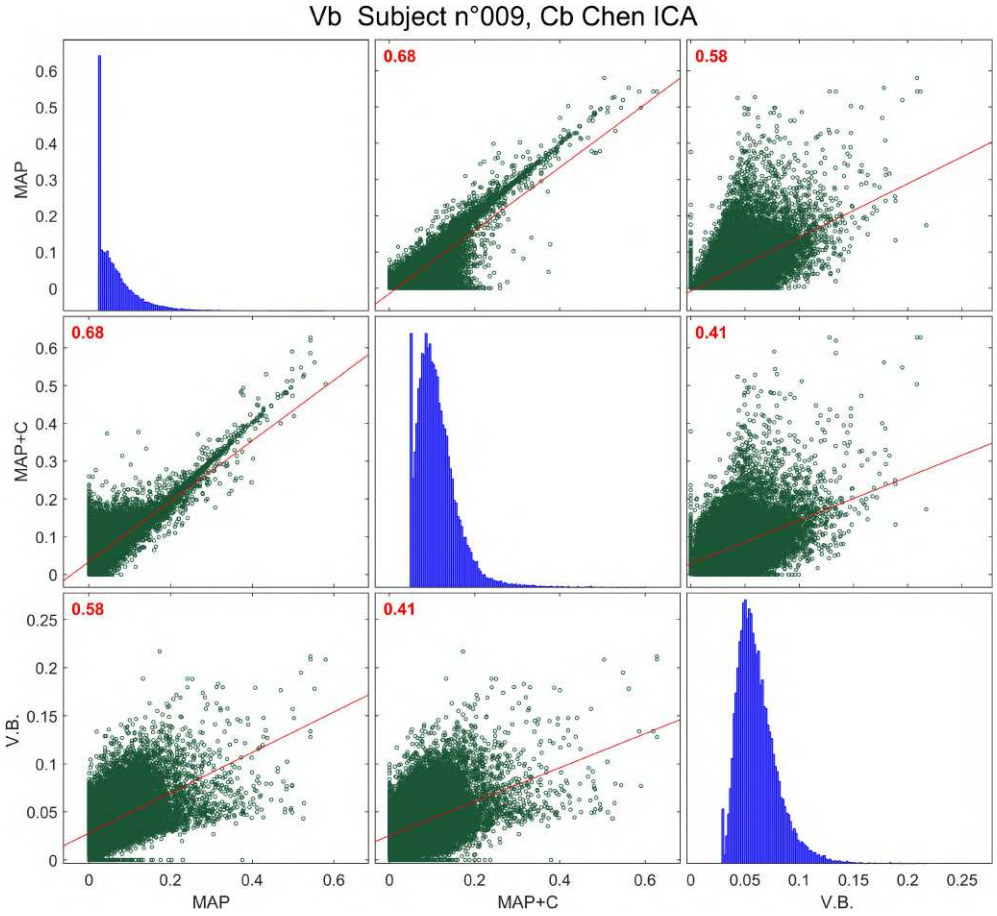

Figure 3.44: Correlation with Vb [adim] values estimated with MAP and Variational Bayesian, Voxel level, ICA with Chen's correction, Subject 009

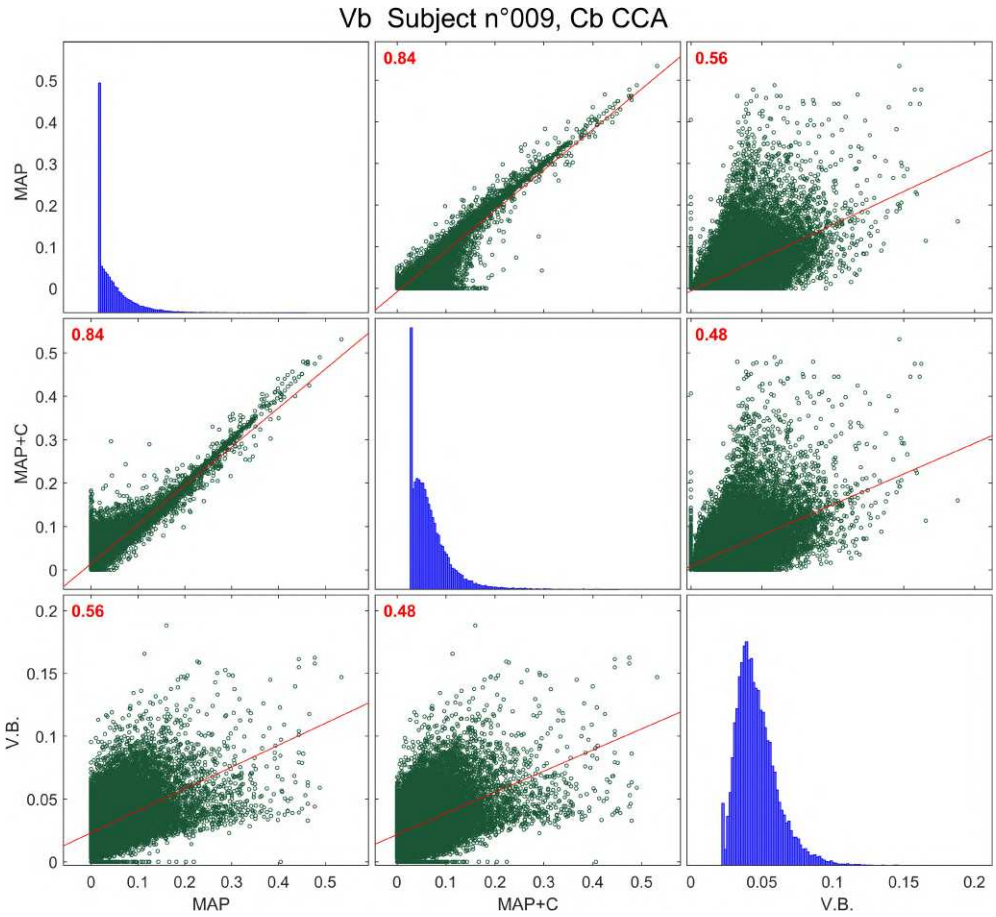

Figure 3.45: Correlation with Vb [adim] values estimated with MAP and Variational Bayesian, Voxel level, CCA with no correction for PVE, Subject 009

The parameters with the highest correlation values with Variational Bayes were K_i and K_1. The k_2 has lower correlation values, while k_3 showed similar values even though it has a significant number of outliers, as previously demonstrated in the exploratory analysis. Vb was the parameter that produced the lowest correlation values with Variational Bayesian.

3.6 Parametric Maps comparison with Variational Bayes at Voxel level

The final comparison step is performed through the reconstruction of parametric maps at voxel level. Only the maps obtained with two out of the four tested input functions are reported in this paragraph (ICA with Chen Correction and CCA with no Correction). To check if the spatial heterogeneity of the microparameter in the tumour area is preserved among the different estimators, an axial slice encompassing the tumour was selected. The parameter maps of subject n° *9* are represented in figures below.

3.6.1 K_i Parametric maps

In this paragraph, parametric maps of slice 90 between K_i estimated values are reported in figures, with a boxplot for the values of the entire brain.

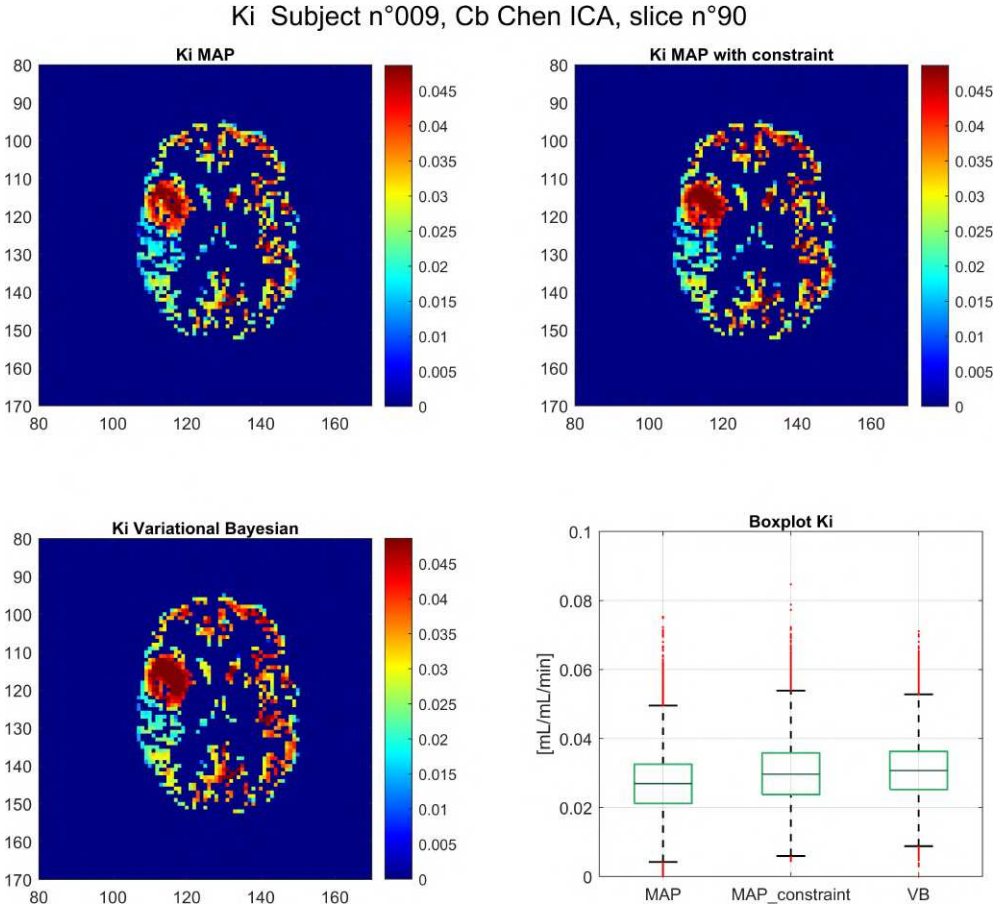

Figure 3.46: K_i parametric map, comparison with MAP and Variational Bayesian, Voxel level, ICA with Chen's correction, Subject 009

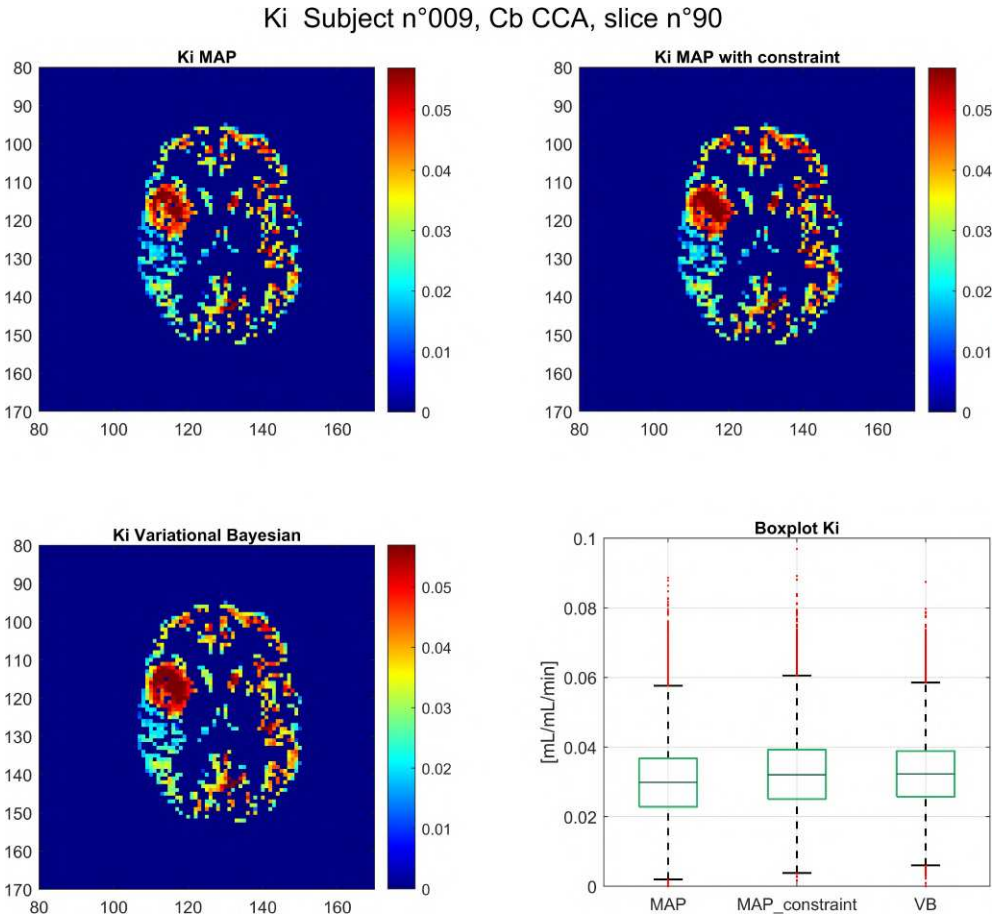

Figure 3.47: K_i parametric map, comparison with MAP and Variational Bayesian, Voxel level, CCA with no correction for PVE, Subject 009

3.6.2 K_1 Parametric maps

In this paragraph, parametric maps of slice 90 between K_1 estimated values are reported in figures, with a boxplot for the values of the entire brain.

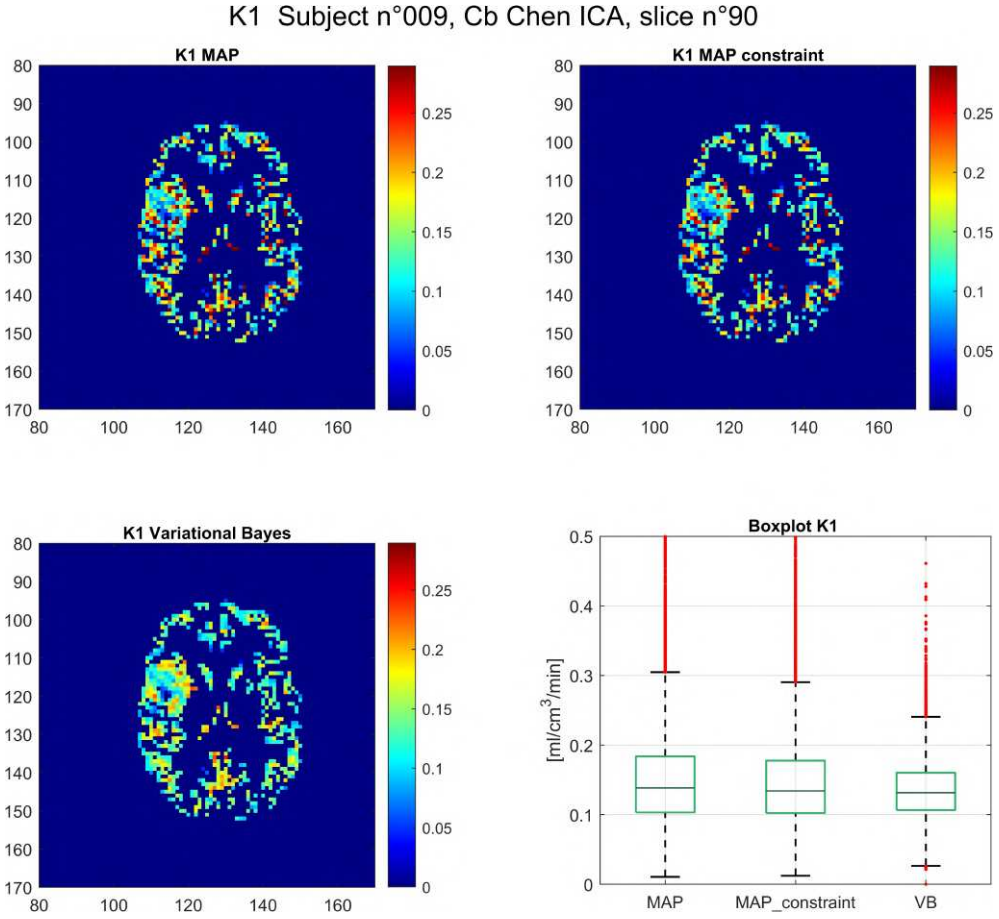

Figure 3.48: K_1 parametric map, comparison with MAP and Variational Bayesian, Voxel level, ICA with Chen's correction, Subject 009

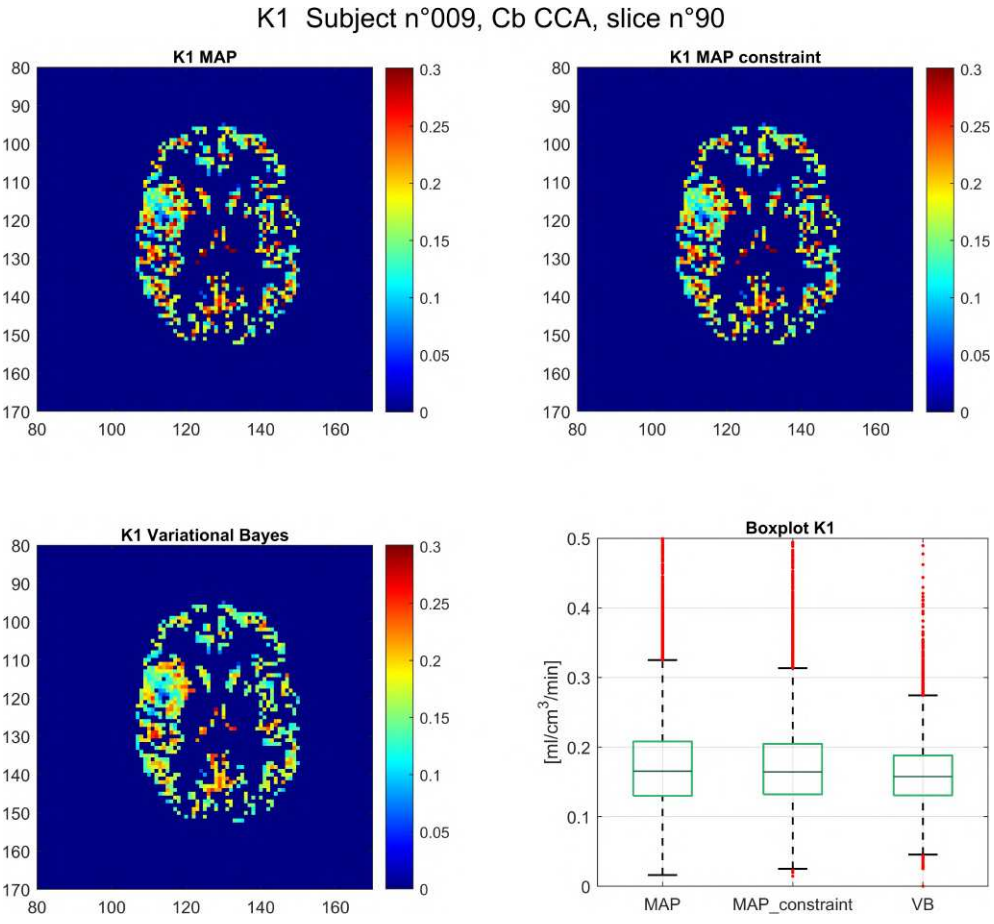

Figure 3.49: K_1 parametric map, comparison with MAP and Variational Bayesian, Voxel level, CCA with no correction for PVE, Subject 009

3.6.3 k_2 Parametric maps

In this paragraph, parametric maps of slice 90 between k_2 estimated values are reported in figures, with a boxplot for the values of the entire brain.

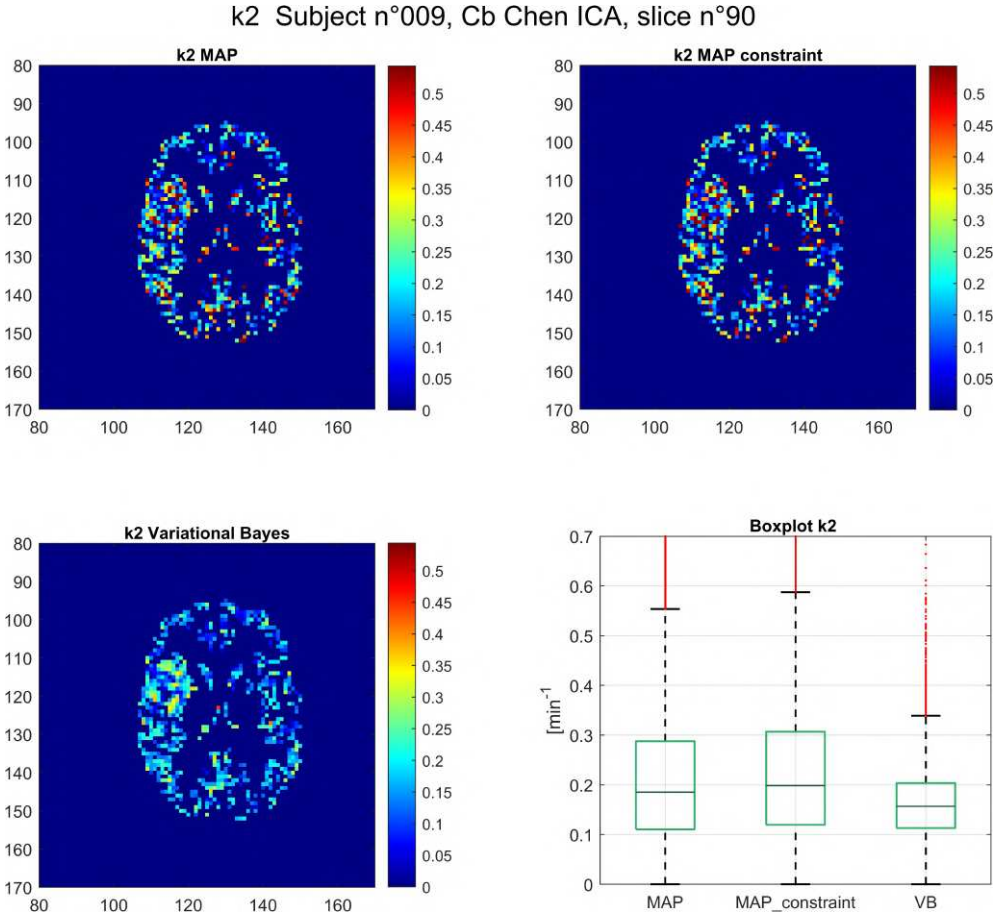

Figure 3.50: k_2 parametric map, comparison with MAP and Variational Bayesian, Voxel level, ICA with Chen's correction, Subject 009

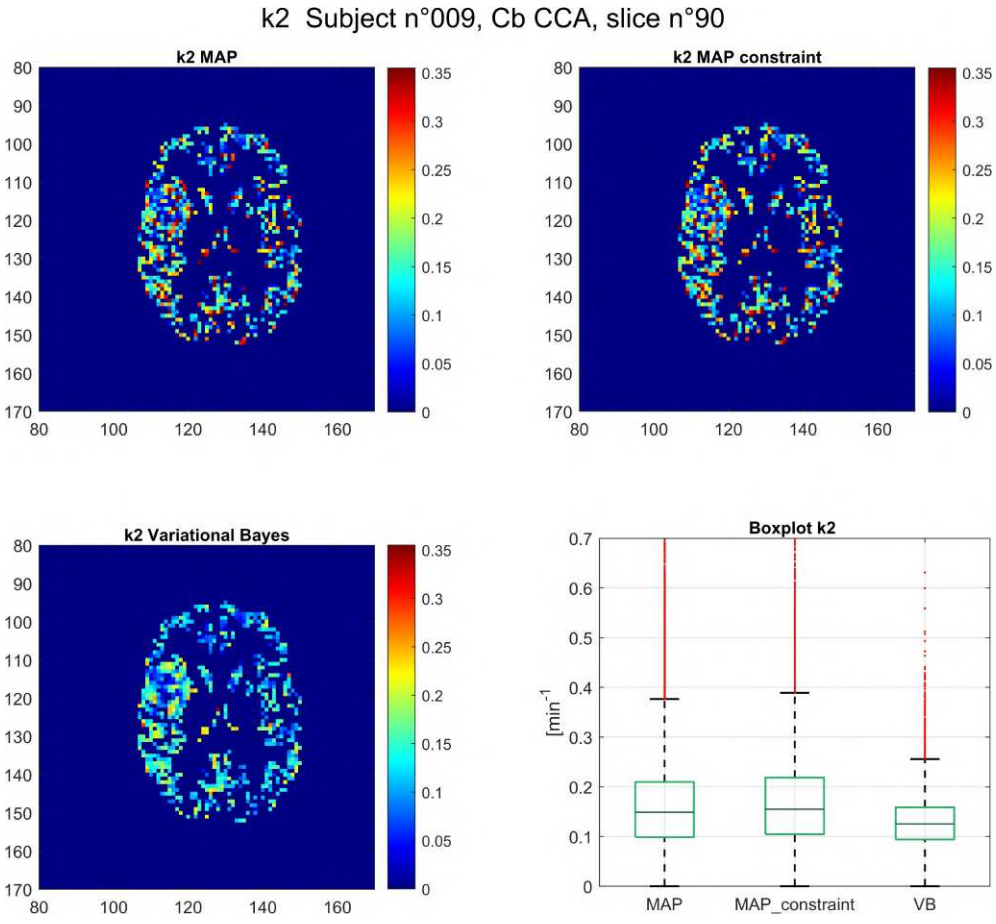

Figure 3.51: k_2 parametric map, comparison with MAP and Variational Bayesian, Voxel level, CCA with no correction for PVE, Subject 009

3.6.4 k_3 Parametric maps

In this paragraph, parametric maps of slice 90 between k_3 estimated values are reported in figures, with a boxplot for the values of the entire brain.

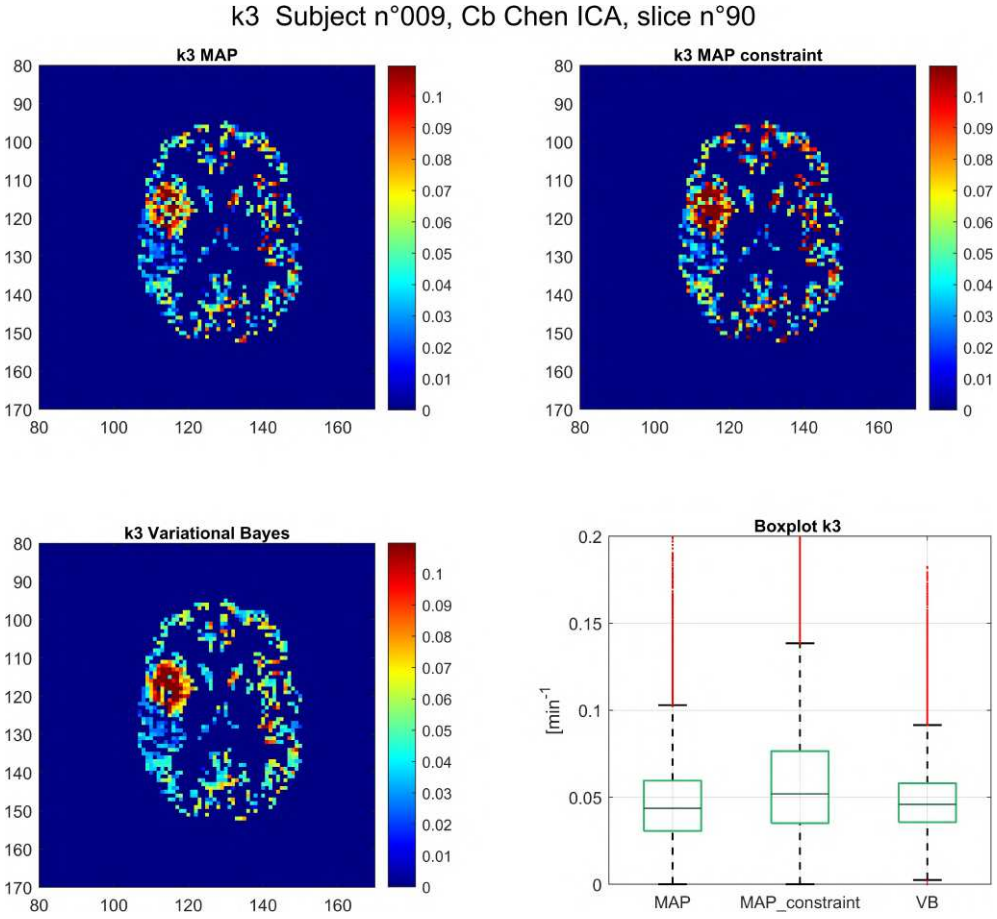

Figure 3.52: k_3 parametric map, comparison with MAP and Variational Bayesian, Voxel level, ICA with Chen's correction, Subject 009

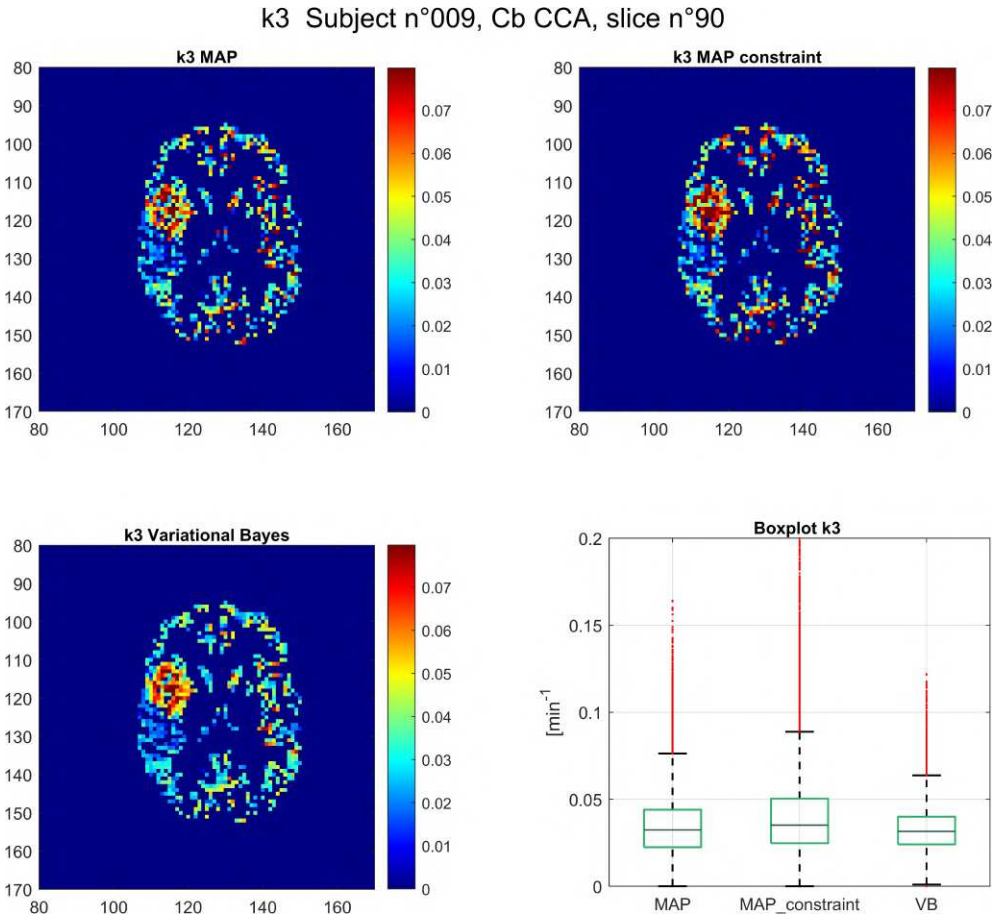

Figure 3.53: k_3 parametric map, comparison with MAP and Variational Bayesian, Voxel level, CCA with no correction for PVE, Subject 009

3.6.5 Vb Parametric maps

In this paragraph, parametric maps of slice 90 between Vb estimated values are reported in figures, with a boxplot for the values of the entire brain.

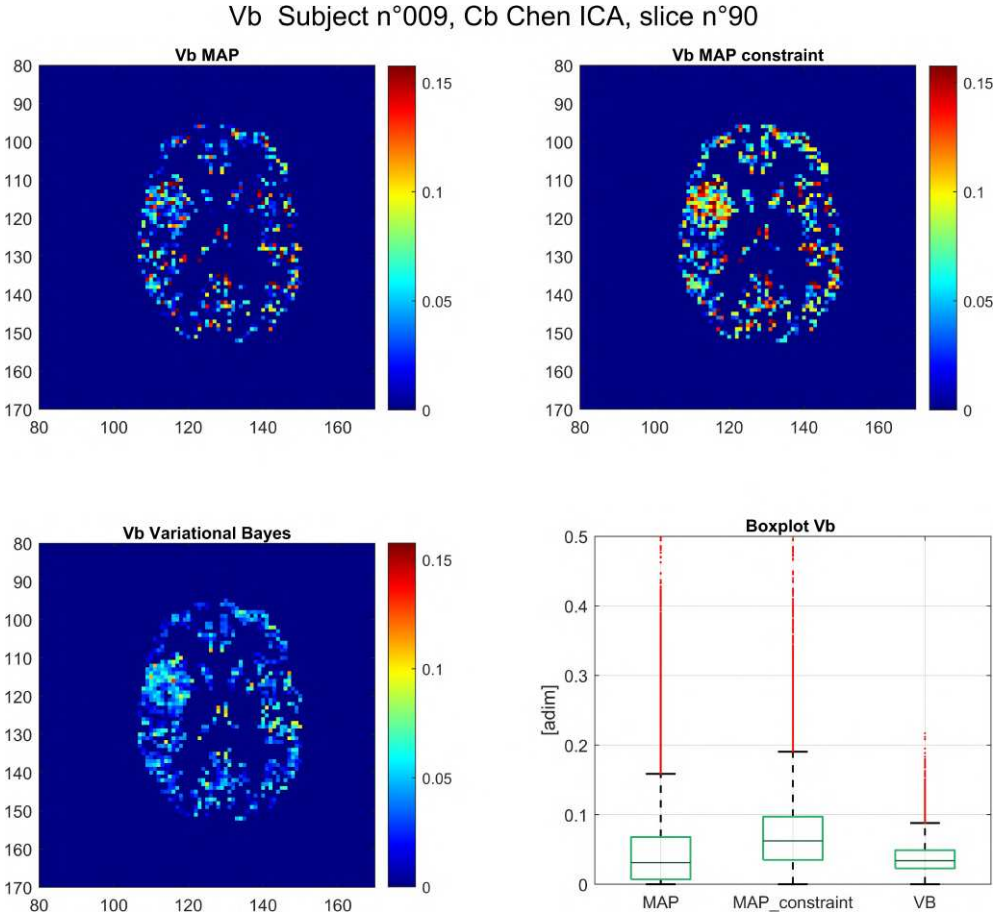

Figure 3.54: Vb parametric map, comparison with MAP and Variational Bayesian, Voxel level, ICA with Chen's correction, Subject 009

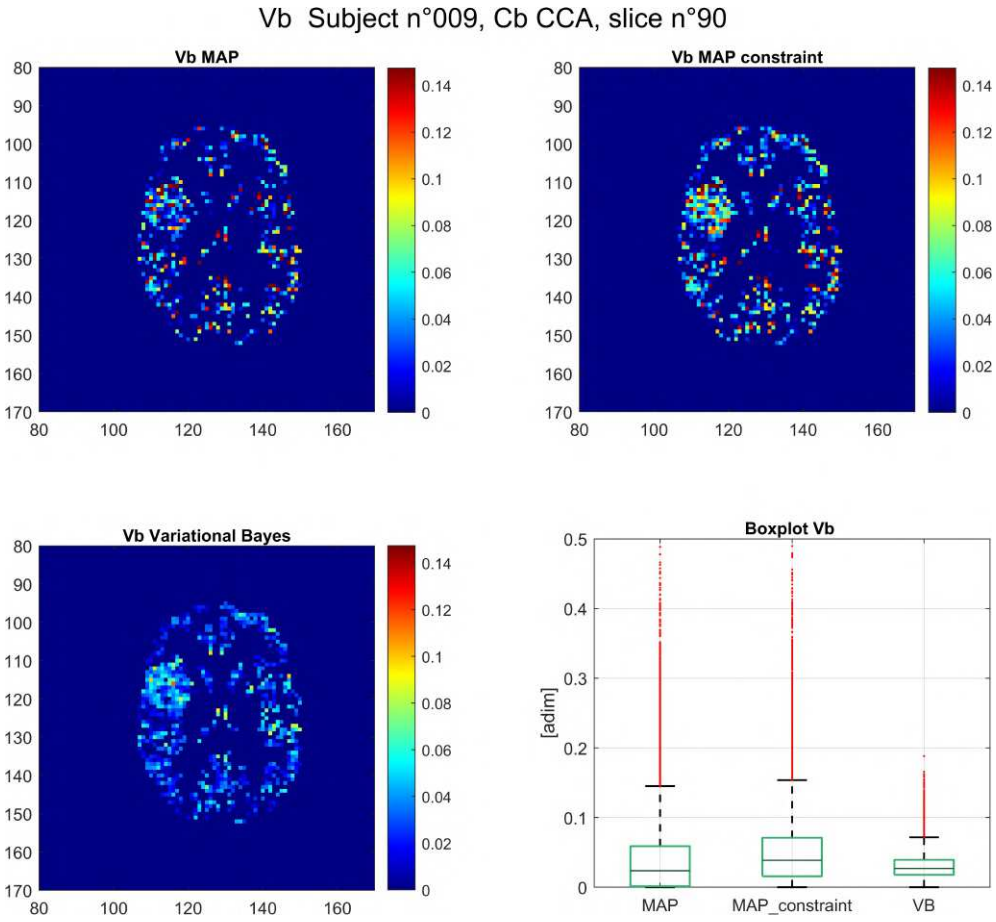

Figure 3.55: Vb parametric map, comparison with MAP and Variational Bayesian, Voxel level, CCA with no correction for PVE, Subject 009

The parameters K_i and K_1 exhibit a common spatial pattern for the compared methods. Similarly, k_3 shows a pattern similar to the previous parameters, despite the presence of a higher number of outliers, especially when the constraint is applied. The parameters k_2 and Vb estimated with MAP, both with and without the constraint, show less satisfactory results compared to Variational Bayesian.

Chapter 4

Discussion

In this thesis project, PET quantification of [^{18}F]FDG microparameters at voxel level was performed. Parametric estimates at the voxel level with non-linear estimator are greatly affected by the noise in the data, resulting in a significant number of non-physiological estimates, high computational costs, convergence issues, or imprecise results. Faster and more robust estimation algorithms are needed. This work aims to overcome the problem by proposing a Bayesian approach, specifically the Maximum A Posteriori (MAP). This analysis also considered the variability in parameter estimates depending on the type of IDIF used. In particular, IDIF from different extraction sites, i.e. ICA and CCA, were considered, with or without Chen's method for PVE correction [17].

K_i estimates derived from Patlak's graphical method are both robust to noise and consistent among different input functions. This was expected, as Patlak is based on a linearization of the original model where the shape of the $C_p(t)$ becomes less influential and, as previously highlighted, estimation of K_i can be solved using a linear estimator [16, 37].

In particular, corrected ICAs and CCAs with no correction show similar results. However, it should be noted that, due to noise, voxel-wise data generates greater uncertainty in the estimation of the fractional uptake, compared to ROI analysis, showing higher CV, table 3.4 and 3.5.

The accuracy of the results for [^{18}F]FDG using a non-linear estimator is confirmed at the ROI level by the outcomes obtained during the estimation of the model's microparameters. The results confirm the feasibility of using the ICA corrected with Chen and the uncorrected CCA [36]. This is because the common carotid arteries are well-suited for extracting the IDIF due to their larger caliber, which also make them easier to segment. Moreover, CCAs are less subject to

PVE as tissues in their proximity have a low tracer uptake. On the contrary, the internal carotid arteries are more affected by PVE, both because of their small caliber, which makes their segmentation more difficult, and because they are closer to brain tissues. We can conclude that for ICAs correction remains necessary, whereas in CCAs it may not be needed: this is reflected by the similarity we observe in the parameter estimates based on ICA with Chen correction and CCA without any correction.

At the ROI level, the results of the model are comparable both without and with the introduction of the constraint. The latter offers reduced complexity and, in some cases, regularization of the estimates. However, it should be noted that the k_3 estimate is the most sensitive to the input function type. In particular, for the uncorrected ICA or the corrected CCA, for many subjects the a posteriori estimates of the k_3 present a significant number of non-physiological values. This, along with what was observed above, suggests that the corrected ICA and the uncorrected CCA may be the IDIFs that produce the most reliable results. Same considerations can be made at voxel level. The scaling factor introduced by using the hematocrit to estimate $C_b(t)$ did not yield significantly different results compared to $C_b(t)$ when is set to be equal to $C_p(t)$.

A first inspection of the results of the voxel-level analysis shows an increase in outliers in the distribution of estimated parameters, compared to the estimates at ROI level. Voxel-level analysis permits to fully exploit the spatial resolution of the image to characterize small lesions within anatomical structures, which is not achievable in ROI-based estimation [6, 31]. However, it is important to consider the challenge of dealing with a low SNR when working at the voxel level

The prior allows us to introduce information into the estimation process, independent from the measurement itself. In this case, the prior information was derived from the ROI-level analysis. Given the low SNR at the voxel level, the prior adds information to make the estimation more reliable, reducing its data dependency while enhancing the precision of the estimates. Our prior is based on the ROI-level parameters obtained with a non-linear estimator. Furthermore, the formulation of the prior remains less sensitive than that of the Variational Bayes estimation. On the other hand, the use of the measurement equation for the error covariance, as mentioned in section 2.2.2, requires the calculation of the posterior covariance constant ρ. By construction of the MAP estimation objective function, it is required that this constant is known before the estimation, in order to properly balance prior information with model fitting to the data.

In our case, we did not have the constant ρ before the estimation. This could have led to the high presence of outliers because omitting this constant can results in an underestimation of the measurement error in certain voxels. When the SNR is too low, the reliability of the observed data drops significantly, and the estimator should draw more information from the prior, so that the estimates are pushed back to a physiological range. However, this is not possible without full knowledge of the error covariance matrix for each voxel TAC.

In addition to this, it should be noted that the constraint also produces additional outliers for the parameter calculated a posteriori, which is k_3. The formulation of the constraint, eq.2.10, takes into account the estimation of the fractional uptake K_i calculated at the voxel level. Although the Patlak method is linear and therefore less sensitive to noise, as observed from the results discussed earlier, voxel-wise estimate may still exhibit low accuracy in some voxels. This may contribute to extracting additional outliers when k_3 is estimated a posteriori using the constraint.

The comparison between the two MAP estimations and with the Variational Bayes has yielded promising results. There is a high correlation among the three methods examined. In particular, the use of constraints produces consistent results with the unconstrained MAP, despite the simplification made to the model structure. Both methods also produce results that are correlated with those previously estimated using Variational Bayes. As for k_3, the results of this work should be interpreted cautiously. Although the unconstrained MAP estimation is comparable with the Variational Bayes, the outliers generated with the introduction of constraints are confounding factors for this analysis.. Managing the outliers remains a challenge that can be overcome by considering an appropriate threshold to filter out non-physiological estimates. Of course, handling the error covariance in an adequate way would be the optimal solution to regularize the estimates.

When assessing the visual analysis of parametric maps, the results are promising. The spatial pattern, especially in the tumor region, remains consistent across all the three methods, demonstrating the validity of MAP despite the high number of outliers, particularly for k_3.

Chapter 5

Conclusions and future works

In this thesis project, we developed a MAP-based approach for [^{18}F]FDG kinetic parameters estimation. We also tested the consistency of the estimates obtained using different input functions. The approach was applied to a dataset consisting of 10 [18F]FDG dynamic acquisitions coming from a PET/MR scanner. The performances of the MAP estimator were compared to the ones obtained with a VB approach.

The MAP estimator has yielded satisfactory results, especially in terms of spatial comparisons with Variational Bayes. The results obtained with different methods exhibit high correlation between them. A good consistency was found in results coming from the IDIF extracted from ICA with PVE correction and the one coming from CCA without any correction. Despite the promising results, particular attention should be paid to the outliers produced at the voxel level. The constraint on this parameter allowed working with a reduced complexity model, which produced results comparable to the complete model estimated with MAP and the results of Variational Bayes. However, for the parameter calculated a posteriori, k_3, a high number of outliers were produced.

The use of MAP provides an advantage in constructing the prior, which is less complex than Variational Bayes, and therefore less prone to operator errors. It is based on information produced by a WNLLS estimator,which can be reliably used at ROI level, but it is not commonly employed at voxel level because of the low SNR. Additionally, the constraint, given the comparable results, would further reduce model complexity. The error covariance needs to be properly addressed to regularize the estimates, and this will need to be tackled in the future.

Bibliography

[1] Anne M J Paans et al. “Positron emission tomography: the conceptual idea using a multidisciplinary approach”. In: (). DOI: 10.1016/S1046-2023(02)00075-0. URL: www.academicpress.com.

[2] Matteo Tonietto et al. “Plasma radiometabolite correction in dynamic PET studies: Insights on the available modeling approaches”. In: *Journal of Cerebral Blood Flow and Metabolism* 36 (2 Feb. 2016), pp. 326–339. ISSN: 15597016. DOI: 10.1177/0271678X15610585.

[3] Giampaolo Tomasi, Federico Turkheimer, and Eric Aboagye. “Importance of Quantification for the Analysis of PET Data in Oncology: Review of Current Methods and Trends for the Future”. In: (2011). DOI: 10.1007/s11307-011-0514-2.

[4] Roger N Gunn and Eugenii A Rabiner. “Comments and Controversies PET neuroimaging: The elephant unpacks his trunk Comment on Cumming: "PET neuroimaging: The white elephant packs his trunk?"” In: (2014). DOI: 10.1016/j.neuroimage.2013.12.042. URL: http://dx.doi.org/10.1016/j.neuroimage.2013.12.042.

[5] Ewart R. Carson and Claudio Cobelli. *Modelling methodology for physiology and medicine*, p. 564. ISBN: 9780124115576.

[6] Alessandra Bertoldo, Gaia Rizzo, and Mattia Veronese. “Deriving physiological information from PET images: from SUV to compartmental modelling”. In: *Clinical and Translational Imaging* 2 (2014), pp. 239–251.

[7] Chris W J Van Der Weijden et al. “Non-invasive kinetic modelling approaches for quantitative analysis of brain PET studies”. In: *European Journal of Nuclear Medicine and Molecular Imaging* (). DOI: 10.1007/s00259-022-06057-4. URL: https://doi.org/10.1007/s00259-022-06057-4.

[8] M. M. Alauddin. "Positron emission tomography (PET) imaging with (18)F-based radiotracers". In: *Am J Nucl Med Mol Imaging* 2.1 (2012), pp. 55–76.

[9] Louis Sokoloff, Charles Kennedy, and Carolyn Smith. "The [14C]Deoxyglucose Method for Measurement of Local Cerebral Glucose Utilization". In: vol. 11. Feb. 2008, pp. 155–193. ISBN: 0-89603-143-8. DOI: 10.1385/0-89603-143-8:155.

[10] M. E. Phelps et al. "Tomographic measurement of local cerebral glucose metabolic rate in humans with (F-18)2-fluoro-2-deoxy-D-glucose: Validation of method". In: *Annals of Neurology* 6 (5 Nov. 1979), pp. 371–388. ISSN: 0364-5134. DOI: 10.1002/ana.410060502.

[11] A. A. Lammertsma et al. "Comparison of Methods for Analysis of Clinical [1C]Raclopride Studies". In: *Journal of Cerebral Blood Flow and Metabolism* 16 (1 1996), pp. 42–52. ISSN: 0271678X. DOI: 10.1097/00004647-199601000-00005.

[12] Paolo Zanotti-Fregonara et al. "Image-derived input function for brain PET studies: Many challenges and few opportunities". In: *Journal of Cerebral Blood Flow and Metabolism* 31 (10 Oct. 2011), pp. 1986–1998. ISSN: 0271678X. DOI: 10.1038/JCBFM.2011.107. URL: www.jcbfm.com.

[13] Yong Choi et al. "Parametric Images of Myocardial Metabolic Rate of Glucose Generated from Dynamic Cardiac PET and 2-[@ 8F]Fluoro-2-deoxy-d.-glucose Studies". In: ().

[14] M. Reivich et al. "Measurement of Local Cerebral Glucose Metabolism: Application to the Study of Stroke". In: Springer Berlin Heidelberg, 1983, pp. 153–161. DOI: 10.1007/978-3-642-95428-3_18.

[15] Win L. Chiou. "The Phenomenon and Rationale of Marked Dependence of Drug Concentration on Blood Sampling Site". In: *Clinical Pharmacokinetics* 17 (4 Oct. 1989), pp. 275–290. ISSN: 0312-5963. DOI: 10.2165/00003088-198917040-00005.

[16] Kewei Chen et al. "Noninvasive quantification of the cerebral metabolic rate for glucose using positron emission tomography, 18F-fluoro-2-deoxyglucose, the Patlak method, and an image-derived input function". In: *Journal of Cerebral Blood Flow and Metabolism* 18 (7 1998), pp. 716–723. ISSN: 0271678X. DOI: 10.1097/00004647-199807000-00002/FORMAT/EPUB.

[17] Yin J. Chen et al. “Relative 11 C-PiB Delivery as a Proxy of Relative CBF: Quantitative Evaluation Using Single-Session 15 O-Water and 11 C-PiB PET”. In: *Journal of Nuclear Medicine* 56 (8 Aug. 2015), pp. 1199–1205. ISSN: 0161-5505. DOI: 10.2967/jnumed.114.152405.

[18] M Castellaro et al. “A Variational Bayesian inference method for parametric imaging of PET data ”. In: (2017). DOI: 10.1016/j.neuroimage.2017.02.009. URL: http://dx.doi.org/10.1016/j.neuroimage.2017.02.009.

[19] Nathaniel M. Alpert and Fang Yuan. “A general method of Bayesian estimation for parametric imaging of the brain”. In: *NeuroImage* 45 (4 May 2009), pp. 1183–1189. ISSN: 10538119. DOI: 10.1016/j.neuroimage.2008.12.064.

[20] Jyh-Ying Peng et al. “Dynamic Positron Emission Tomography Data-Driven Analysis Using Sparse Bayesian Learning”. In: *IEEE Transactions on Medical Imaging* 27.9 (2008), pp. 1356–1369. DOI: 10.1109/TMI.2008.922185.

[21] G. Rizzo et al. “Multi-Scale hierarchical generation of PET parametric maps: Application and testing on a [11C]DPN study”. In: *NeuroImage* 59 (3 Feb. 2012), pp. 2485–2493. ISSN: 10538119. DOI: 10.1016/j.neuroimage.2011.08.101.

[22] Francesca Zanderigo et al. “Empirical Bayesian estimation in graphical analysis: a voxel-based approach for the determination of the volume of distribution in PET studies”. In: *Nuclear Medicine and Biology* 37 (4 May 2010), pp. 443–451. ISSN: 09698051. DOI: 10.1016/j.nucmedbio.2010.02.004.

[23] Yan Zhou, John A.D. Aston, and Adam M. Johansen. “Bayesian model comparison for compartmental models with applications in positron emission tomography”. In: *Journal of Applied Statistics* 40 (5 May 2013), pp. 993–1016. ISSN: 0266-4763. DOI: 10.1080/02664763.2013.772569.

[24] Go Akamatsu et al. “A review of harmonization strategies for quantitative PET”. In: *Annals of Nuclear Medicine* 37 (2 Feb. 2023), pp. 71–88. ISSN: 0914-7187. DOI: 10.1007/s12149-022-01820-x.

[25] Dagan Feng, Sung-Cheng Huang, and Xinmin Wang. “Models for computer simulation studies of input functions for tracer kinetic modeling with positron emission tomography”. In: *International Journal of Bio-Medical Computing* 32 (2 Mar. 1993), pp. 95–110. ISSN: 00207101. DOI: 10.1016/0020-7101(93)90049-C.

[26] Tommaso Volpi et al. “Modeling venous plasma samples in [{18}{F}] FDG PET studies: a nonlinear mixed-effects approach”. In: IEEE, July 2022, pp. 4704–4707. ISBN: 978-1-7281-2782-8. DOI: 10.1109/EMBC48229.2022.9871429.

[27] Mattia Francisci et al. “EMATA: an automatic toolbox for the Extraction and Modeling of Arterial inputs for Tracer kinetic Analysis”. In: (July 2023). DOI: 10.36227/techrxiv.23592996.

[28] Jurgen E M Mourik et al. “Image-derived input functions for PET brain studies”. In: (). DOI: 10.1007/s00259-008-0986-8. URL: www.bic.mni.mcgill.ca/software/Display/Display.html,.

[29] Robert Hall. “Vascular injuries resulting from arterial puncture or catheterization”. In: *British Journal of Surgery* 58.7 (Dec. 2005), pp. 513–516. ISSN: 0007-1323. DOI: 10.1002/bjs.1800580711. eprint: https://academic.oup.com/bjs/article-pdf/58/7/513/37089966/bjs1800580711.pdf. URL: https://doi.org/10.1002/bjs.1800580711.

[30] C. S. Patlak, R. G. Blasberg, and J. D. Fenstermacher. “Graphical evaluation of blood-to-brain transfer constants from multiple-time uptake data”. In: *Journal of Cerebral Blood Flow and Metabolism* 3 (1 1983), pp. 1–7. ISSN: 0271678X. DOI: 10.1038/JCBFM.1983.1.

[31] Bernard M. Mazoyer et al. “Dynamic PET Data Analysis”. In: *Journal of Computer Assisted Tomography* 10 (4 July 1986), pp. 645–653. ISSN: 0363-8715. DOI: 10.1097/00004728-198607000-00020.

[32] Dagan Feng, Xianjin Li, and Wan-Chi Siu. “OPTIMAL SAMPLING SCHEDULE DESIGN FOR POSITRON EMISSION TOMOGRAPHY DATA ACQUISITION”. In: 5 (12 1997), pp. 16–1759.

[33] Kewei Chen, Sung-Cheng Huang, and Dagan Feng. “New estimation methods that directly use the time accumulated counts in the input function in quantitative dynamic PET studies”. In: *Physics in Medicine and Biology* 39 (11 Nov. 1994), pp. 2073–2090. ISSN: 0031-9155. DOI: 10.1088/0031-9155/39/11/017.

[34] Richard J Roman. “The mathematical modeling of metabolic and endocrine systems : E.R. Carson, C. Cobelli. and L. Finkelstein. John Wiley and Sons, New York. 1983. 394 pp., illus., index.” In: *Mathematical Modelling* 7 (1986), p. 1669. URL: https://api.semanticscholar.org/CorpusID:118101152.

[35] A. Bertoldo et al. “Evaluation of compartmental and spectral analysis models of [/sup 18/F]FDG kinetics for heart and brain studies with PET”. In: *IEEE Transactions on Biomedical Engineering* 45 (12 1998), pp. 1429–1448. ISSN: 00189294. DOI: 10.1109/10.730437.

[36] Erica Silvestri et al. “Image-derived Input Function in brain [18 F]FDG PET data: which alternatives to the carotid siphons?” In: IEEE, July 2022, pp. 243–246. ISBN: 978-1-7281-2782-8. DOI: 10.1109/EMBC48229.2022.9871200.

[37] S. C. Huang et al. “Noninvasive determination of local cerebral metabolic rate of glucose in man”. In: *American Journal of Physiology-Endocrinology and Metabolism* 238 (1 Jan. 1980), E69–E82. ISSN: 0193-1849. DOI: 10.1152/ajpendo.1980.238.1.E69.

[38] Nicholas J. Tustison et al. “N4ITK: Improved N3 Bias Correction”. In: *IEEE Transactions on Medical Imaging* 29.6 (2010), pp. 1310–1320. DOI: 10.1109/TMI.2010.2046908.

[39] Jimit Doshi et al. “Multi-Atlas Skull-Stripping”. In: *Academic Radiology* 20 (12 Dec. 2013), pp. 1566–1576. ISSN: 10766332. DOI: 10.1016/j.acra.2013.09.010.

[40] Brian B. Avants et al. “A reproducible evaluation of ANTs similarity metric performance in brain image registration”. In: *NeuroImage* 54 (3 Feb. 2011), pp. 2033–2044. ISSN: 1053-8119. DOI: 10.1016/J.NEUROIMAGE.2010.09.025.

[41] Vladimir Fonov et al. “Unbiased average age-appropriate atlases for pediatric studies”. In: *NeuroImage* 54 (1 Jan. 2011), pp. 313–327. ISSN: 1053-8119. DOI: 10.1016/J.NEUROIMAGE.2010.07.033.

[42] Hasan Sari et al. “Estimation of an image derived input function with MR-defined carotid arteries in FDG-PET human studies using a novel partial volume correction method”. In: *Journal of Cerebral Blood Flow and Metabolism* 37 (4 2017), pp. 1398–1409. ISSN: 15597016. DOI: 10.1177/0271678X16656197.

[43] F O’sullivan et al. “Kinetic Quantitation of Cerebral PET-FDG Studies Without Concurrent Blood Sampling: Statistical Recovery of the Arterial Input Function NIH Public Access”. In: *IEEE Trans Med Imaging* 29 (3 2010), pp. 610–624. DOI: 10.1109/TMI.2009.2029096. URL: http://ieeexplore.ieee.org..

[44] Naoya Hattori et al. “Acute Changes in Regional Cerebral 18 F-FDG Kinetics in Patients with Traumatic Brain Injury”. In: ().

[45] Robert B. Innis et al. “Consensus nomenclature for in vivo imaging of reversibly binding radioligands”. In: *Journal of Cerebral Blood Flow and Metabolism* 27 (9 Sept. 2007), pp. 1533–1539. ISSN: 0271678X. DOI: 10.1038/SJ.JCBFM.9600493. URL: www.jcbfm.com.

Ringraziamenti

Ringrazio la Prof.ssa Alessandra Bertoldo per avermi dato l'opportunità di svolgere questo lavoro di tesi. La ringrazio per la sua considerazione nei miei confronti, e per avermi trasmesso una parte, seppur fondamentale, della sua esperienza in questo campo.

Ringrazio il mio correlatore Mattia De Francisci per la sua pazienza, per i consigli che mi hanno accompagnato durante il progetto, avendo sempre considerazione del mio pensiero, trasmettendomi la sua passione per l'argomento.

Ringrazio i miei colleghi dell'Università, con i quali ho condiviso questo percorso pieno di alti e bassi, durante il quale ci siamo sempre sostenuti a vicenda, ed ora che arriva alla conclusione, ognuno di noi ha ottenuto le proprie soddisfazioni.

Ringrazio i miei amici di Padova, con i quali il legame è stato sempre fonte di condivisone di pensieri, paure ma anche obiettivi e gioie.

Un ringraziamento alla mia squadra, in quanto credo che il legame sportivo sia uno dei più puliti e profondi che possa nascere tra le persone, perchè rappresenta motivo di sacrificio, impegno, rispetto e condivisione di momenti felici.

Ringrazio i miei più cari amici, ai quali devo tanto, l'affetto scambiato seppur lontani, e soprattuto la voglia e l'esuberanza di condividere i momenti più rappresentativi della nostra vita.

Ringrazio la mia famiglia, alla quale dedico questo lavoro, segno della conlcusione del mio percorso universitario. A chi da lontano, ma anche da più vicino, mi ha sempre sostenuto, con gesti e parole che in determinati momenti sono valsi oro.

Infine, ma non per importanza, grazie Clara per essere stata sempre al mio fianco, ogni singolo momento. Sei stata fonte di fiducia nei miei confronti, senza la quale non avrei raggiunto determinati obiettivi. Sei la mia tifosa numero uno.